Thermal Contact Resistance between Ceramic and Metallic Surfaces with Applications in Power Electronics

by
Mikel Garcia-Poulin

B.Eng., McGill University, 2016

Thesis Submitted in Partial Fulfillment of the
Requirements for the Degree of
Master of Applied Science

in the
School of Mechatronic Systems Engineering
Faculty of Applied Sciences

SIMON FRASER UNIVERSITY
Fall 2018

Approval

Name: **Mikel Garcia-Poulin**

Degree: **Master of Applied Science**

Title: **Thermal Contact Resistance between Ceramic and Metallic Surfaces with Applications in Power Electronics**

Examining Committee:
Chair: Amr Marzouk
Lecturer

Majid Bahrami
Senior Supervisor
Professor

Jiacheng (Jason) Wang
Supervisor
Assistant Professor

Kevin Oldknow
Internal Examiner
Senior Lecturer & Associate Dean

Date Defended/Approved: November 29, 2018

Abstract

In power electronic systems, aluminum oxide (alumina) is frequently used to electrically isolate high voltage devices mounted onto touch safe heat sinks for cooling. The thermal contact resistance (TCR) developed between the aluminum oxide and the metallic surfaces may significantly increase the thermal resistance between the heat generating device and the heat sink. In this thesis, the thermal contact resistance between ceramics and metals is explored analytically and experimentally. The TCR between polished ceramics and bead-blasted metals was first measured under uniform contact pressures (0.25 – 1.5 MPa) in both atmospheric and vacuum conditions. These results are compared with existing metallic surface TCR models to validate their use with metallic-ceramic surfaces. TCR measurements of as-fired, lapped and polished aluminum oxide in contact with machined, cast and anodized extruded aluminum surfaces with thermal interface materials (TIMs) are also presented.

Keywords: thermal contact resistance; thermal contact conductance; TCR; TCC; alumina; ceramic insulator

Dedication

I would like to dedicate this thesis to my cousin Simon Rochefort.

Acknowledgements

I would like to thank Dr. Majid Bahrami for providing me with the opportunity to study in his lab and for his supervision and guidance throughout my degree. I would like to thank my supervisory and examining committee for taking their time to improve this thesis. I would like to thank Mr. Chris Botting, Mr. Eric Lau and Delta-Q Technologies for the opportunity to work with them and for their willingness to share their time and technical knowledge.

Dr. Mehran Ahmadi, Dr. Wendell Huttema, Dr. Clair McCague, Dr. Maryam Khajehpour, and Dr. Sepehr Foroushani are due many thanks for their technical support, expert advice and our many discussions. I would also like to thank Mustafa Sajid from the MSE machine shop, and the teams at both the Faculty of Applied Science Machine shop and 4D Labs for use of their facilities and expertise.

I would like to thank my lab mates and friends who have helped me through good times and bad. Finally, I would like to thank my family; Mom, Dad, Yoana and Miss Christina Harvey for their love, support and incredible patience for which I am truly grateful.

Table of Contents

List of Tables

List of Figures

Nomenclature

Latin

A_a = *Apparent contact area* [m^2]

A_r = *Real contact area* [m^2]

a = *Microcontact radius*

b = *Fluxtube radius*

c_1 = *Hardness parameter [GPa]*

c_2 = *Hardness parameter [GPa]*

C = *Capacitance [F]*

d = *Gas gap distance [m]*

E = *Bulk Elasticity [GPa]*

D_{bolt} = *Bolt diameter [m]*

f = *Friction factor*

F = *Contact force [N]*

g = *Acceleration of gravity* [m/s^2]

Gr = *Grashof number*

h = *Contact conductance* [W/(m^2·K)]

H' = *Micro-hardness [GPa]*

H_{BR} = *Brinell hardness [GPa]*

I = *Electric current [A]*

k = *Thermal conductivity [W/(m·K)]*

M = *Gas gap rarefaction parameter*

m = *Average asperity slope [rad]*

n = *Number of micro contact spots*

P = *Apparent contact pressure [Pa]*

P_e = Electric power [W]

Pr = Prandtl number

$\dot{Q}$ = Heat transfer rate [W]

R_b = Bond-line thermal resistance [K/W]

R_j = Joint thermal resistance [K/W]

R_{1D} = 1D Thermal resistance

t = Thickness [m]

T = Temperature [K]

T_b = Torque [Nm]

t_o = Initial TIM thickness

V = Voltage [V]

Y = mean separation between planes

Greek

α = Accommodation parameter

α_T = thermal accommodation coefficient

β = Gas parameter

β_{CTE} = Coefficient of thermal expansion [1/K]

ε = Relative size of microcontacts

ε_0 = Permittivity of free space [F/m]

ε_r = Relative permittivity

Λ = molecular mean free path [m]

δ = Flatness deviation [μm]

γ = ratio of gas specific heats

γ_p = Mikic plasticity index

λ = Relative mean separation between planes

ν = *Poisson ratio*

ν_k = *Kinematic viscosity [m^2/s]*

σ = *Roughness [μm]*

σ_0 = *1 μm unit*

ψ = *Constriction/spreading resistance parameter (constriction alleviation factor)*

List of Acronyms

BJT	Bipolar Junction Transistor
FET	Field Effect Transistor
LAEC	Laboratory for Alternative Energy Conversion
PCM	Phase Change Material
SFU	Simon Fraser University
MOSFET	Metal Oxide Semiconductor Field Effect Transistor
TBR	Thermal Boundary Resistance [K/W]
TCC	Thermal Contact Conductance [K/W]
TCR	Thermal Contact Resistance [K/W]
TIM	Thermal Interface Material
TO	Transistor Outline

Executive Summary

Motivation

Power electronics are ubiquitous in our society as they play a key role in a wide range of engineering systems ranging from vehicles to telecom and communication systems. It is expected that the global power electronics market will grow from 31.5 (2015) to 39.2 (2025) billion USD as renewable energy resources and electric transportation become more main stream [1], [2]. For example, to meet CO_2 reduction goals, the auto industry will need to put 50 million electric and plug-in hybrid electric vehicles (EV/PHEV) on the road annually by 2050 and the energy industry requires over 3,300 GW of global renewable energy (solar photovoltaic and wind) capacity by 2030 [3]–[5]. These technologies require low cost, efficient and reliable power electronics which in turn require adequate thermal management [6].

Thermal management of electronics is a significant industry totalling over 10.7 billion USD in global revenues in 2015 [7]. This is because semiconductors, the building blocks of power electronic devices, require cooling to maintain efficiency, minimize stress from thermal expansion and avoid thermal runaway. In fact, increasing device temperature results in an exponential increase in device failure rate [8]. Understanding heat transfer is therefore critical for the design of reliable power electronics. Bottlenecks to heat transfer from device to ambient include; bulk thermal resistance due to the thermal conductivity of the materials in the heat transfer path, spreading resistances due to shape changes in the heat transfer path, thermal contact resistance (TCR) due to heat being restricted to flow through real contact points between two surfaces and the resistance to convection off the heat sink.

High voltage power devices require electrical insulation if they are to be mounted onto touch-safe heat sinks as they often are in battery chargers and power supplies. The electrical insulation adds thermal resistance to the heat transfer from device to ambient. In some cases, the electrical insulation represents the largest thermal resistance in the heat path.

Ceramics, like aluminum oxide (alumina), are good electrical insulators and have thermal conductivities an order of magnitude higher than other dielectrics [9]. They are frequently used as electrical insulators with thermal grease in power electronic systems. They are hard materials and very expensive to polish. However, their use with thermal grease implies that the TCR formed at the interface with metallic surfaces is high when in bare contact.

Most TCR studies in the literature have been focused on bare metal to metal contact [10]. TCR models developed for metal-metal contacts suggest that TCR is a function of contact pressure, material hardness and or elasticity, thermal conductivity of the contacting solids and the interstitial fluid in between them (usually air for a bare contact) and surface geometries [10]. Ceramic surface features are different from metals however as they are formed by particles sintered together at high temperature and pressure. Finally, ceramics do not have free electrons, they must rely on lattice vibrations (phonons) to conduct heat. Despite these differences, the pertinent literature suggests that metal-metal models can be used to predict the TCR for ceramic-ceramic contacts [11], [12]. Ceramic-metal contacts have only been explored in the form of coatings and those compared with metal-metal models did not match [13], [14]. No studies have been conducted on the TCR between ceramic-metal contacts, i.e. without coatings.

In this thesis, the thermal contact resistance between alumina and metals is comprehensively explored in collaboration with Delta-Q Technologies, a leading battery charger manufacturer for small electric vehicle batteries.

Objectives

The research objectives are to:

- Minimize the thermal resistance between heat generating discrete power devices (diodes and MOSFETs) and fully sealed heat sink enclosures in Delta-Q’s chargers.
- Model and predict the thermal contact resistance developed between ceramic and metallic surfaces.

Methodology

A systematic experimental-analytical approach has been adopted to achieve the goals of this research. A block diagram overview for the program is shown in Fig. 1.

The thermal contact resistance study was primarily experimental. Thermal contact resistance was experimentally measured using a guarded heat flow meter, partially per ASTM E1530 [15], available in the Laboratory for Alternative Energy Conversion at SFU. Thermal contact resistance was investigated under various contact pressures, air pressures and sample temperatures using this device. Metallic samples were machined and bead-blasted at SFU's Mechatronics Systems Engineering and Faculty of Science machine shops to include and study the effect of surface roughness on the TCR of metallic-ceramic contacts. Existing analytical models [10], [16]–[18] for metal-metal joints were compared with the experimental results from the ceramic-metal joints. Results were in agreement, in some cases.

To compare the thermal performance of ceramic insulators with other commercially available dielectric thermal interface materials (TIMs), a custom-built testbed was designed and built in the lab. Results showed that bare ceramic insulators were competitive with polyimide insulators and that the thermal resistance was reduced by 70% when ceramic was used with a thermal interface material.

Contributions

The contributions from this thesis are listed below:

- Investigated thermal resistance of electrical insulation for bolted and clamped discrete power devices [19] (Chapter 2);
- Conducted a comprehensive experimental study on thermal contact resistance between polished ceramics and bead-blasted stainless steel surfaces under vacuum and atmospheric pressures over a range of contact pressures, 0.25–1.5 MPa (Chapter 3);

- Studied the validity of existing analytical metal-metal thermal contact resistance models for metal-ceramic joints, under various contact pressures and surface roughness (Chapter 3);
- Experimentally studied the thermal contact resistance of as-fired, lapped and polished aluminum oxide in contact with machined, cast and anodized extruded aluminum surfaces with and without TIMs and compared with models (Chapter 4).

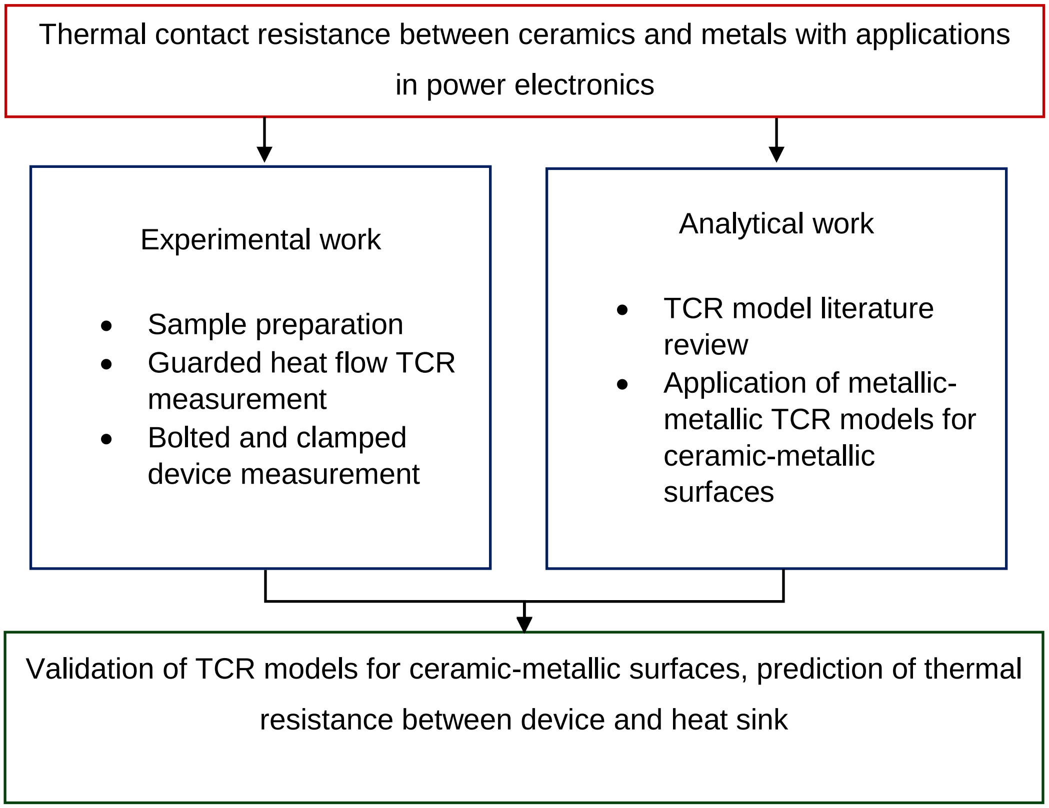

Fig. 1: Research roadmap

Chapter 1. Introduction

1.1. Power electronics

Power electronics, broadly categorized as electronic circuits that primarily control or convert electrical power, are ubiquitous in our society. Examples include battery chargers, electric motor drives, dc-dc converters and telecom rectifiers. Not only are power electronics necessary to operate household devices that run on electricity, like cellphones and computers, they play key roles in a variety of modern engineering systems including electric vehicles, telecom and communication systems and renewable energy technology [20]. In fact, as renewable energy resources and electric transportation become more main stream, it is expected that the power electronics market will grow 30% over ten years, from 31.5 (2015) to 39.2 (2025) billion USD [1], [2]. For example, to meet CO_2 reduction goals, the auto industry will need to put 50 million electric and plug-in hybrid electric vehicles (EV/PHEV) on the road annually by 2050 and the energy industry requires over 3,300 GW of global renewable energy (solar photovoltaic and wind) capacity by 2030 [3]–[5]. These technologies require low cost, efficient and reliable power electronics [20]. Fig. 2 contains examples of typical power electronic systems.

Fig. 2: Power electronics examples: Top left: Bitron Electronics's power inverter for electric vehicles [21]; Top middle: Delta's solar inverter [22]; Top right: Elmo's servo drive for wind turbines [23]; Bottom left: Alpha's rectifier for telecom [24]; Bottom middle: Corsair's power supply for PCs [25] and Bottom right: Delta-Q's battery charger for utility vehicles [26].

Semiconductors are the building blocks of modern day (i.e. current) power electronics. A semiconductor is a material, typically silicon, that neither conducts electricity poorly (electrical insulator) nor well (electrical conductor) [27]. Semiconductor electrical conductivities can be modified by adding dopants (impurities) [27]. For example, p-type silicon can be doped with boron and has a deficiency of valence electrons (i.e. holes), while n-type silicon may be doped with arsenic and contains an excess of valence electrons [27]. The semiconductor junction (P-N, P-N-P, etc.), the union of these doped semiconductors, is the heart for most electronic devices including diodes and transistors [27].

Power electronics rely on solid-state switching devices to convert and control electricity. Diodes are two terminal devices that restrict current to flow in one direction while transistors are three terminal devices that allow for controlled current and voltage modulation [27]. Transistors are generally used as switches or amplifiers and can come in many variations including bipolar junction transistors (BJTs) and field effect transistors (FETs) [27]. Fig. 3 includes an example of the devices found in power electronics. Other devices include inductors, transformers and capacitors.

Fig. 3: Power electronic devices: Left: TO-247 MOSFET; Left middle: TO-220 diode array; Right middle: electrolytic capacitor and Right: transformer

Fig. 4 shows a typical battery charger, an example of an industrial power electronics system. The charger rectifies AC current to DC current to charge a DC battery. In Fig. 4, the devices are mounted onto a printed circuit board (PCB). The PCB also houses the circuitry between components. Standard PCBs are made of layers of fiberglass (FR4) and copper circuitry. The PCB is then mounted onto a heat sink that dissipates the heat generated by the electronics to the environment. In this application, the heat sink is touch-safe and is electrically isolated from the PCB using electrical insulation. This charger (IC650, 650 W, 24-48 V) was designed and manufactured by Delta-Q Technologies. Throughout this thesis, this battery charger is used as a reference for power electronic applications. In addition, certain studies are in collaboration with

Delta-Q Technologies and are motivated with the goal of improving the thermal management design of Delta-Q's battery charger.

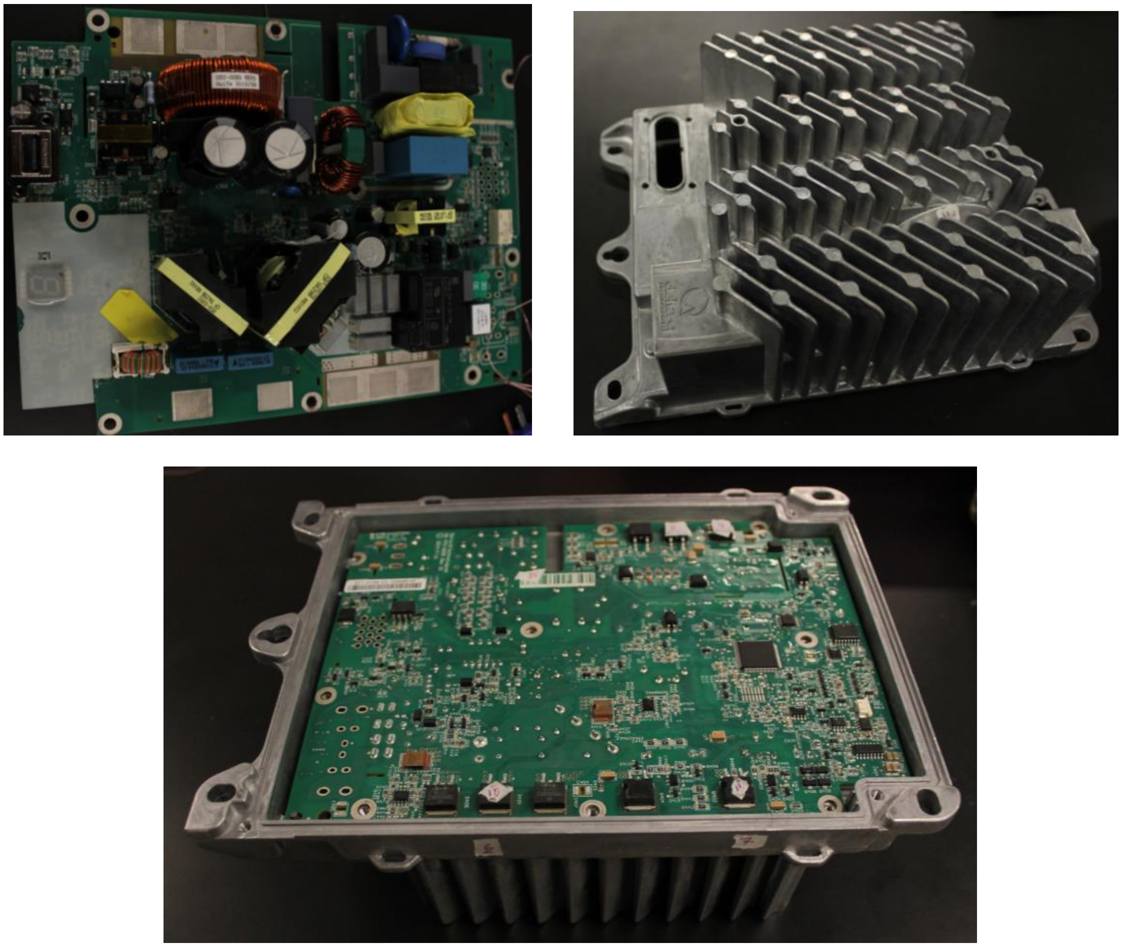

Fig. 4: Delta-Q's IC650 battery charger; Top left: bottom of PCB; Top Right: heat sink enclosure top view; and Bottom middle: PCB in heat sink upside down.

1.2. Thermal management of power electronics

Thermal management of electronics is a significant industry totalling over 10.7 billion USD in global revenues in 2015 [7]. This is because electronics require cooling to maintain reliable operation. Power electronics are no different and often require high voltages and currents which can compound the thermal problem.

1.2.1. Heat sources

Most electronics losses are emitted in the form of heat. There are several sources of heat generation depending on the type of device.

Joule heating was first proposed by James Prescott Joule in 1841 [28]. It occurs in all electrically conducting materials (expect for superconductors). Joule heating can be summed up by Eq. 1, i.e., electrons flowing through a conductor (electric current) are scattered by ions in the conductor and converted into heat.

$$\dot{Q} = I^2 R_e \tag{1}$$

Switching losses occur while a device is transitioning from ON to OFF and vice versa. It is a function of frequency, input voltage, and current. In power electronics, transistors primarily dissipate heat due to switching losses and conduction losses. Transformers or inductors generate heat due to winding losses (joule heating in the windings) and core losses (ferromagnetic related losses i.e. hysteresis and eddy currents) [29].

Transistors have decreased in size (famously predicted by Moore) and increased in density and switching frequency for decades [29]. The net result has been an increase in heat generated per unit area, or heat flux. Thermal management has not kept up and has limited the development of high power electronics [29].

1.2.2. Failures

If the heat generated within a device is not removed, then device temperature will rise which can lead to several issues resulting in failure. As materials expand and contract due to thermal expansion, bonded materials and joints will experience stress and strain. Over many cycles, these thermal expansion induced stresses can cause fatigue failure [29]. Temperature increase can also result in increased heat generation due to either an increased resistance with temperature or increased current flow with temperature. The net result is further temperature increase and in turn more heat generation. This is known as thermal runaway. Corrosion, electro migration and ionic contamination may also occur due to improper thermal management [29].

In general, device failure rate increases exponentially with increasing device temperature [8]. Proper thermal management and heat transfer analysis is therefore critical for the design of reliable power electronics.

1.2.3. Heat transfer and thermal resistances

Heat transfer is driven by temperature difference and impeded by thermal resistance. In heat transfer problems, the resistance network analogy is often applicable, where the thermal resistance is given by Eq. 2.

$$R = \frac{\Delta T}{\dot{Q}} \tag{2}$$

In general, thermal resistances between electronic device and ambient can be divided into 4 categories: 1) bulk thermal resistance, 2) spreading resistance, 3) thermal contact resistance (TCR) and 4) film resistance. Fig. 5 is an example of a typical thermal resistance network from a power device mounted onto a heat sink.

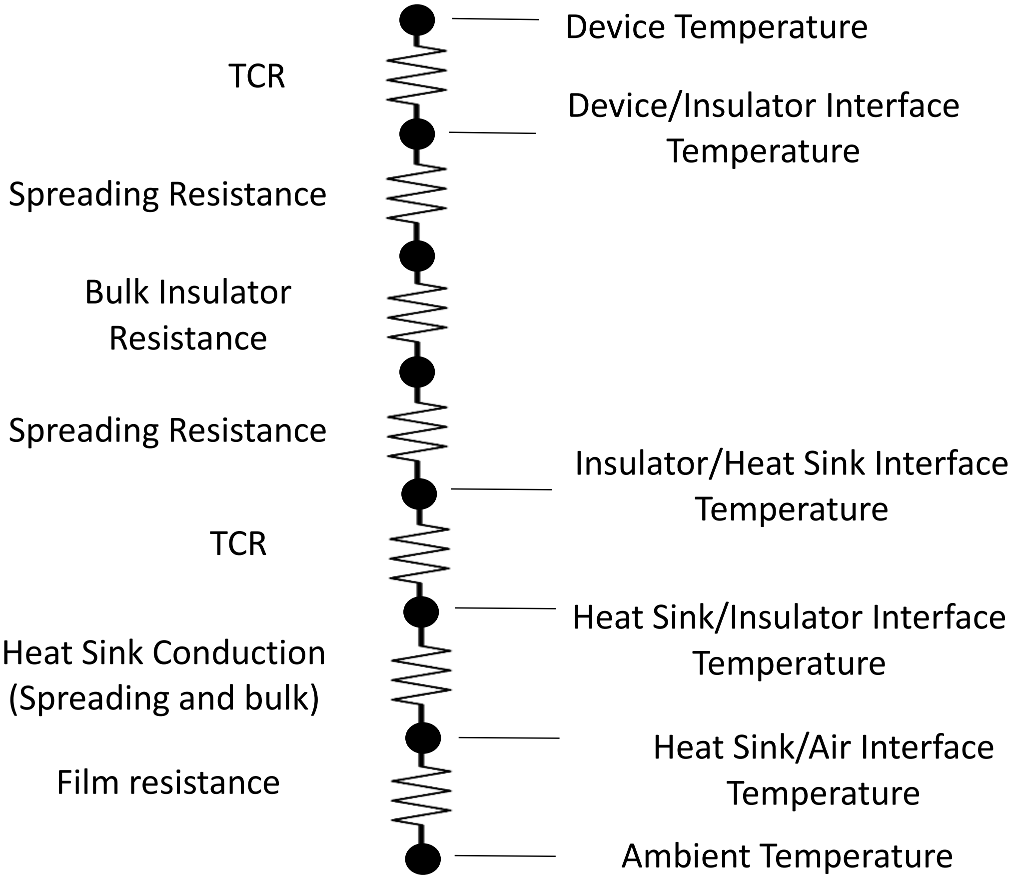

Fig. 5: Typical thermal resistances from device to ambient in power electronics device

Bulk thermal resistance is due to the resistance of the material itself to conducting heat. It may be minimized by selecting materials with a high thermal conductivity, k. In one dimensional planar heat transfer (1D), bulk resistance is calculated with Eq. 3. The thermal conductivity of materials is an empirical material property defined by Fourier's law (shown for 1D in Eq. 4) and measured experimentally.

$$R_{1D} = \frac{t}{kA} \tag{3}$$

$$\dot{Q} = -kA\frac{dT}{dx} \tag{4}$$

If the problem requires two or three dimensions, Eq. 3 is not sufficient, and the thermal resistance is a function of the boundary conditions and the geometry of the problem. However, in certain cases 2D or 3D effects may be simplified into a separate thermal resistance conveniently used in 1D heat transfer networks. Thermal spreading resistance (or constriction resistance) is one such case and is the resistance caused by area mis-matches in the heat transfer path. Spreading resistance into an infinite hemisphere is given by Eq. 5 for an isothermal circular contact with radius a.

$$R_s = \frac{1}{4ka} \tag{5}$$

Film resistance is the resistance to convection off the heat sink to the ambient. Convection, the sum of advection (bulk flow) and diffusion (flow due to gradients) can be categorized into natural convection or forced convection. Natural convection is driven by density change in the fluid due to temperature difference while forced convection is driven by pressure difference caused by a fan or pump. In power electronics, heat sinks are typically air cooled either by forced or natural convection. Fans are not desired because they add cost and risk to a cooling system but they are often required for higher power densities. In vehicles or data centers, electronics can be cooled by liquid cooling or two-phase cooling where the power densities and economics justify the added cost and complexity of the cooling system. Fig. 6 illustrates the different cooling methods from heat sink to ambient and their respective heat transfer coefficient defined by Eq. 6, Newton's law of cooling.

$$\dot{Q} = hA\Delta T \tag{6}$$

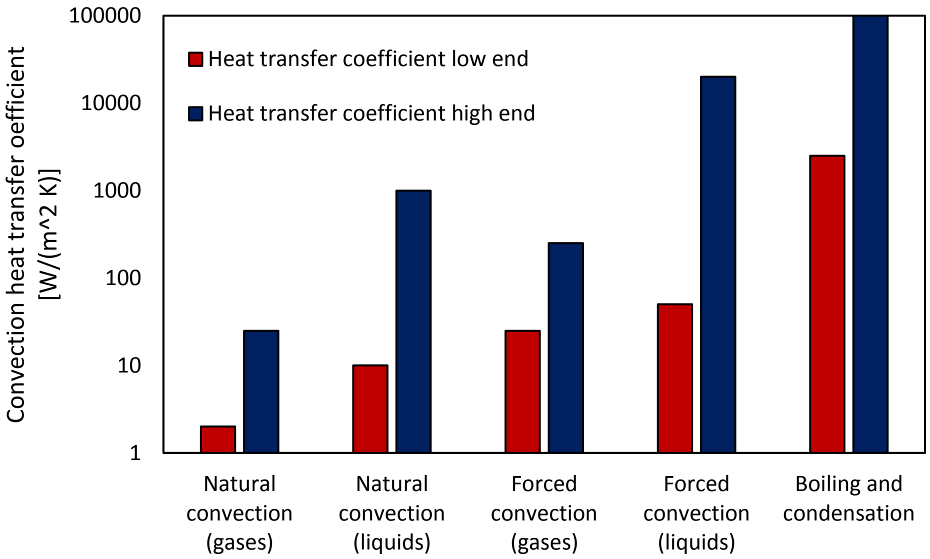

Fig. 6: Typical convective heat transfer coefficients [30].

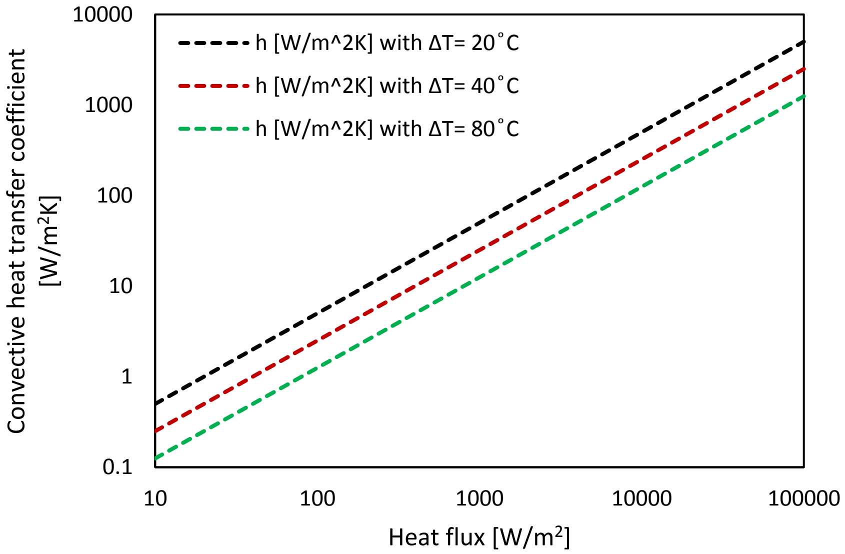

Fig. 7: Heat transfer coefficient required vs heat flux at given temperature difference between heat sink and ambient.

To illustrate the point, Delta-Q's IC650 heat sink is used as an example. If the maximum allowable temperature of the heat sink (both a safety requirement for users of the charger and performance requirement to maintain operation of the electronics), is set at 80˚C and the charger operates in ambient air of 40˚C while emitting 87 W, then the minimum convective heat transfer coefficient required to cool the charger is equal to 8.4 W/(m^2 K). Clearly, forced liquid cooling is not justified for this application. Convection coefficient vs heat flux is plotted in Fig. 7.

Film resistance is a main bottleneck to heat transfer. Air convection, forced or natural, is widely considered to be at its limit. In power electronics, if heat sinks are properly designed, film resistance is often a function of economics as liquid cooled systems are not financially viable nor practical for many systems. This subject, though interesting, is not the focus of this thesis.

1.3. Thermal contact resistance

Thermal contact resistance (TCR), the main focus of this thesis, is the resistance to heat transfer across mated parts due to surface imperfections such as roughness, out-of-flatness, machine lay or surface curvature. All surfaces are imperfect and TCR is therefore irritably present in most thermal designs. TCR is infamously difficult to model because it is a strong function of microscopic surface geometry and surface properties that are not always well quantified. TCR is not yet easily approximated with numerical methods such as finite element analysis (FEA) as are other thermal problems because it is a multi-dimensional problem that requires significant micro-scale geometric characterisation and modelling.

Thermal contact resistance was discovered during the space age when satellites were sent up to space and experienced vacuum air pressures. In a vacuum, TCR increases by an order of magnitude as heat is no longer able to travel through air pockets in between solid surfaces and is constricted to travel through the real contact spots in a joint. Fig. 8 illustrates TCR in a vacuum.

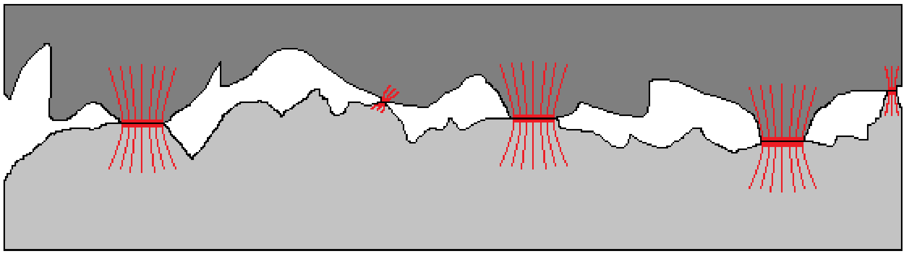

Fig. 8: Heat is forced to flow through real contact points in a vacuum.

Thermal contact resistance between metals has been significantly studied since the 1960s because metals are the most common materials in thermal designs. TCR between bare metals is a function of material thermal conductivity, hardness (actually, surface micro-hardness) and/or elasticity and surface geometry parameter such as roughness and roughness slopes. TCR is also a strong function of contact pressure as it influences the geometry of the joint. Accurately predicting TCR is of strong interest to the thermal engineering community as it simplifies the thermal design process.

Analytically modelling TCR is a multi-disciplined task requiring: 1) geometrical (statistics, surface metrology); 2) mechanical (deformable solid mechanics); and 3) thermal (heat transfer) modelling.

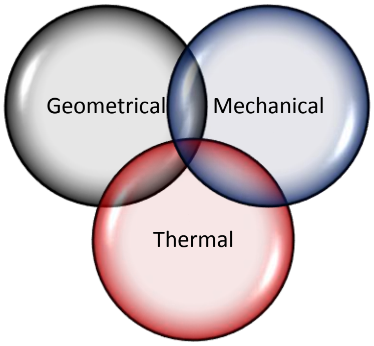

Fig. 9: Thermal contact resistance triad.

1.3.1. Geometrical models

Surface imperfections can be modelled statistically [31], with fractals [32],fast Fourier transforms [33] or as may be the case with FEM contact analysis [34] , with actual scans of the surface. In this thesis, we follow the statistical approach for its simplicity and reasonable agreement with experimental data.

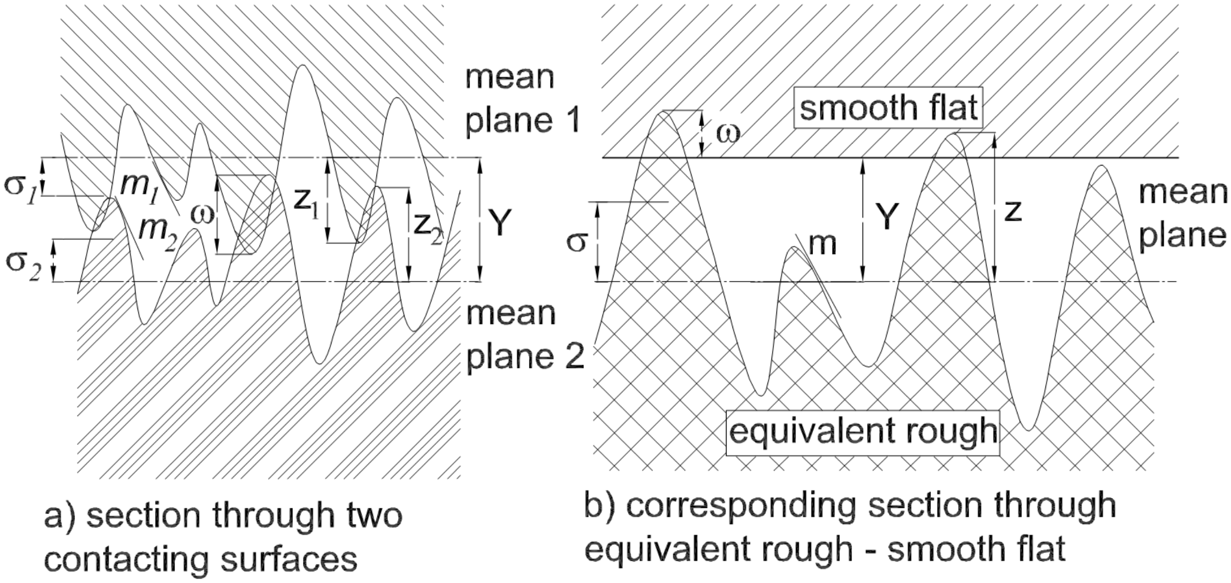

Fig. 10: Equivalent rough surface and perfectly smooth surface for conforming rough contact.

Perhaps the simplest and most common models assume a Gaussian (normal) distribution of deviations (called asperities) from a mean line as an approximation for microscale surface roughness. Furthermore, it is often assumed that the asperity peaks are circular and that their radius is also a Gaussian distribution. If the heights of the asperities are Gaussian, then the slopes of the asperities are also Gaussian. To simplify the geometry, the joint is approximated by an effective rough surface (see Fig. 10 [35]), encompassing surface properties from both surfaces, in contact with a perfectly flat surface. These models require simple inputs such as root mean square (RMS) roughness (σ) of the deviations (z) from the surface mean plane and average asperity slopes of these asperities (m). These may be measured for each surface using a stylus profilometer. Because of the Gaussian assumption, the effective parameters may be easily calculated with Eq. 7 and 8.

$$\sigma = \sqrt{\sigma_1^2 + \sigma_2^2} \tag{7}$$

$$m = \sqrt{m_1^2 + m_2^2} \tag{8}$$

Macro-scale out-of-flatness can be modelled as surface curvature [36] or periodic large wavelength waviness (0.08 to 8 mm). A cut-off wavelength is used to differentiate between roughness and waviness, its determination is facilitated by existing standards and is a function of mean surface roughness R_a (8 mm for $R_a > 10$ μm, 2.5 mm for 10 μm $> R_a > 2$ μm, etc.). These models may be combined with micro-scale models to cover non-conforming rough contact. Similar to roughness, the surface curvature of both surfaces may be combined into the effective surface curvature. The joint is then approximated by a flat surface in contact with a round surface with the effective surface curvature.

1.3.2. Mechanical models

Several methods exist in the literature to model the deformation of the contacting surfaces. If real surfaces (i.e. scans) are used in the geometric model, then the mechanical model may be calculated with FEA. This is an intensive activity but is an active research topic. Similarly, mechanical models also exist for fractal geometries. If the statistical method is chosen for the geometry, then the mechanical model is readily calculated depending on whether the deformation of the asperities is in the elastic or plastic range.

Common assumptions include:

- Gaussian asperity distribution
- Interfacial forces are in the normal direction (friction is neglected)
- Microcontacts are far apart from each other and deformation of one does not affect another
- Deformation is determined from the equivalent surface

Elastic vs plastic deformation of asperities has been heavily debated in the literature [37]. Models exist from both schools of thought exist. Mikic introduced a plasticity-elasticity ratio, Eq. 9, to identify whether deformation was plastic ($\gamma_p < 0.33$), elastic ($\gamma_p > 3$) or elasto-plastic ($0.33 < \gamma_p < 3$). Elastic models require Young's modulus and Poisson ratio as an input, while plastic models require a hardness parameter.

$$\gamma_p = \frac{H_{micro}}{Em} \tag{9}$$

$$E = \left(\frac{1 - \nu_1^2}{E_1} + \frac{1 - \nu_2^2}{E_2} \right)^{-1} \tag{10}$$

Hardness changes as function of indentation depth and force. When indentation depths and forces are small, hardness is called surface micro-hardness [38] and is often much larger than bulk material hardness. This is hypothesized to be because of work hardening on the surface of metals. In general surface micro-hardness is a function of the material at the surface, effective roughness, effective average asperity slope and contact pressure. Yovanovich and Hegazy showed that statistical TCR models are accurate for a wide range of metal surfaces if the surface micro-hardness is used as an input and not the bulk material hardness [39]. The mechanical model outputs the mean relative separation between contacts with Eq. 11 or Eq. 12 to calculate the average micro contact radius with Eq. 13, the number of contact points with Eq. 14 and the ratio of real to apparent contact area with Eq. 15 [40].

$$\lambda_{elastic} = \sqrt{2}\,\mathrm{erfc}^{-1}\left(\frac{4\sqrt{2}\,P}{mE}\right) \tag{11}$$

$$\lambda_{plastic} = \sqrt{2}\,\mathrm{erfc}^{-1}\left(\frac{2P}{H'}\right) \tag{12}$$

$$a = \mathrm{erfc}\left(\frac{\lambda}{\sqrt{2}}\right)\frac{\sigma}{m}e^{\frac{\lambda^2}{2}}\sqrt{\frac{8}{\pi}} \tag{13}$$

$$n = \frac{\frac{1}{16}\left(\frac{m}{\sigma}\right)^2 e^{-\lambda^2}}{\mathrm{erfc}\left(\frac{\lambda}{\sqrt{2}}\right)} \tag{14}$$

$$\frac{A_{real}}{A_{apparent}} = \frac{1}{2}\mathrm{erfc}\left(\frac{\lambda}{\sqrt{2}}\right) \tag{15}$$

On the macro-scale, models are built starting from Hertzian contact and bulk deformations are generally considered elastic. In this thesis, only conforming rough contact is considered.

1.3.3. Thermal models

In a vacuum, TCR is the constriction and spreading resistance at each solid spot contact in parallel. In general, it is assumed that contacts are far enough apart from each other so that the constriction and spreading resistance at the contacts are not affected by each other. The spreading resistance for each contact point can be calculated using Eq.17 for the half-space geometry and Eq. 18 for the fluxtube geometry (b is the radius of the fluxtube and a the microcontact radius). Both geometries give similar results [36]. Eq. 16 is the effective thermal conductivity of the joint. The constriction/spreading resistance parameter (Eq. 19) is required for the fluxtube model and is calculated from the relative microcontact radius ε. All the micro-contacts are in parallel, given by Eq. 21 for half space and Eq. 22 for fluxtube spreading/constriction resistance.

$$k = \frac{2k_1 k_2}{k_1 + k_2} \tag{16}$$

$$R_{asperity\ halfspace} = \frac{1}{2ka} \tag{17}$$

$$R_{asperity\ fluxtube} = \frac{\psi(\varepsilon)}{2ka} \tag{18}$$

$$\psi(\varepsilon) = (1 - \varepsilon)^{1.5} \tag{19}$$

$$\varepsilon = \frac{a}{b} = \sqrt{A_{real}/A_{apparent}} \tag{20}$$

$$TCR_{halfspace} = \frac{1}{2nk_s a} \tag{21}$$

$$TCR_{flux\ tube} = \frac{\psi(\varepsilon)}{2nk_s a} \tag{22}$$

$$h_{contact\ micro\ solid} = \frac{1}{TCR\ A_{apparent}} \tag{23}$$

If there is a fluid between the solids, such as air, then heat may conduct through the fluid gaps between both solids. Gas gap models are available in the literature for a range of Knudsen numbers [16] [41]. The Knudsen number is calculated using Eq. 24 and identifies the conduction regime in the gas. If Knudsen is greater than 10 the gas is in the free molecule regime and gas molecule collision are rare. The transition regime occurs for Knudsen between 0.1 and 10 and the slip regime occurs for Knudsen less than 0.1 but greater than 0.01. When Knudsen is less than 0.01, the gas is in the continuum regime and the gas molecule collisions are frequent. Λ is the mean free path of the gas and is a function of gas temperature and gas pressure and d is the distance between solid surfaces [16].

$$Kn = \frac{\Lambda}{d} \tag{24}$$

One of the simplest gas gap models available in the literature, Eq. 25, assumes that the resistance across the gas gap is equal to the conduction (depending on the gas regime) between two isothermal planes (T_i in Fig. 11) with an area equal to the apparent contact area, separated by the distance between the two mean planes, Y (Y=σλ). This model is depicted in Fig. 11 [35]. The authors assumed that the real contact area was negligible for the gas gap resistance calculation since it is typically 1% of the apparent contact area [35]. This model also neglects the bulk conduction of the solid between the isothermal planes and the contact planes in each solid surface. The thickness of this solid is labelled l in Fig. 11 and is on the order of 40 microns [35]. This is a fair assumption since the thermal conductivity of the solids are orders of magnitude greater than the thermal conductivity of gasses in the gap. The gas gap rarefaction parameter, M, is a function of an accommodation parameter (α), a gas parameter (β) and the mean free path (Λ). More details on these parameters are provided in chapter 3. The solid contact resistance and the gas gap resistance are in parallel as seen in Eq. 27.

$$R_{gas} = \frac{\sigma\lambda + M}{k_g A_a} \tag{25}$$

$$M = \alpha\beta\Lambda \tag{26}$$

$$TCR = \left(R_{micro\ solid}^{-1} + R_{gas}^{-1}\right)^{-1} \tag{27}$$

Micro gaps (<0.01 mm) are typically too small for natural convection and therefore only conduction is considered [16]. Natural convection can be neglected for Grashof numbers less than 2500 [16]. It is easily shown that a Grashof number much less than 2500 is reasonable for the joints in this thesis. Assuming a mean ideal gas temperature of 363 K, (90˚C, the mean temperature of the joints in Chapters 3 and 4), with $\beta_{cte}= 1/T_m$, solid temperatures of 340 K (67˚C) and 384 K (111˚C) taken from experiment, kinematic viscosity of air equal to 2.3×10^{-5} m^2s^{-1} and a generous gas gap, d, of 1 mm the Grashof number is 2.2. This is calculated using Eq. 28.

$$Gr = \frac{g\beta_{cte}(T_{s1} - T_{s2})d^3}{\nu_k^2} \tag{28}$$

Radiation is typically neglected in TCR modelling because its heat transfer contribution is negligible at low temperature differences [10].

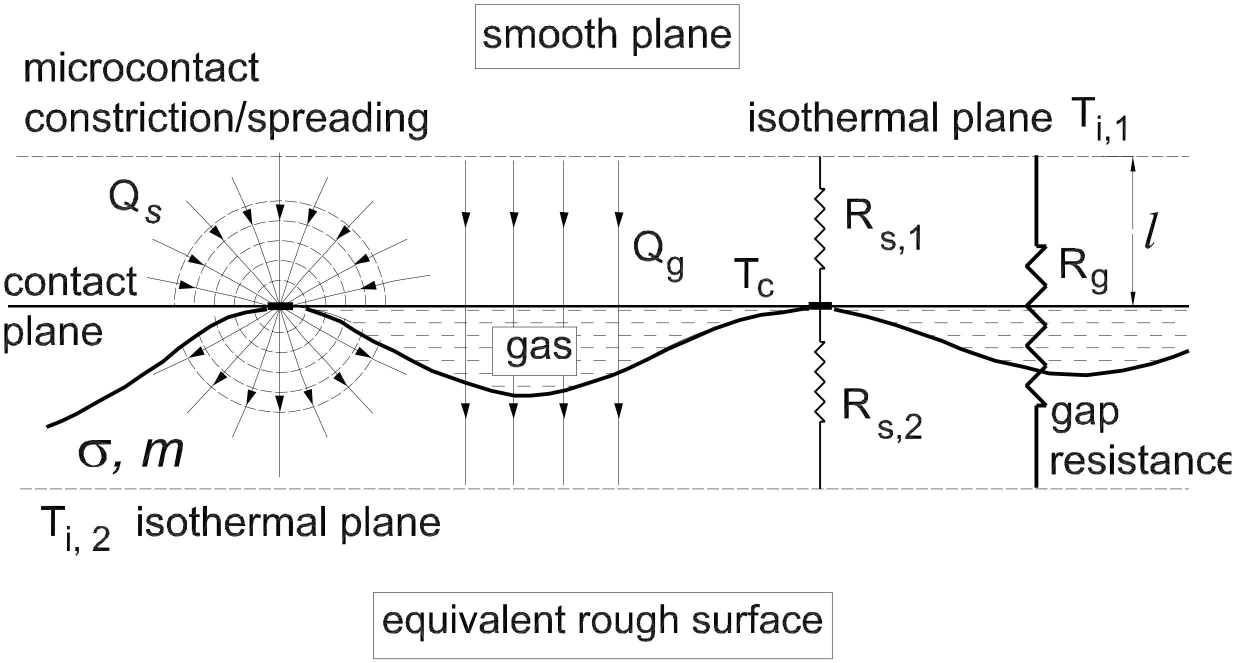

Fig. 11: Gas gap model by Bahrami et al. [35]

1.4. Thermal interface materials

Thermal interface materials (TIMs) are materials inserted in between solid joints in order to reduce TCR. Effective TIMs include thermal greases, thixotropic gap fillers, metal foils, graphite sheets, carbon nanotube arrays and phase change materials (PCMs).

TIMs reduce TCR by filling the micro gaps between the real solid contact spots. In essence, they replace the air (or vacuum) in the gaps; increasing the thermal conductivity of the gaps by at least an order of magnitude. This is seen in the gas (now TIM filled) gap model for joints filled with greases, gap fillers and PCMs [42].

$$R_{TIM\ gaps} = \frac{\sigma\lambda}{k_{TIM} A_a} \tag{29}$$

In practice, the thickness of the TIM between the solids (bond-line thickness) is not negligible and must be considered in the model. Typically, the bond-line thickness and thermal conductivity of the TIM are very influential on the total joint resistance. In addition, the wetting characteristics of the TIM on the surfaces in question are important. Models exist that consider surface tension, air pockets stuck between TIM and solid in the gaps and adhesion forces [43]. Eq. 31 is the combination of contact resistance between TIM and each solid, the TIM filled gap resistance and the bond-line thickness and is also appropriate for deformable sheets like graphite and metal foils [44] [42].

$$R_{TIM\ bondline} = \frac{t_b}{k_{TIM} A_a} = \frac{t_0 \left(1 - \frac{P}{E_{TIM}}\right)}{k_{TIM} A_a} \tag{30}$$

$$R_{TIM} = \left(R_{contact}^{-1} + R_{gaps}^{-1}\right)^{-1} + R_b + \left(R_{contact}^{-1} + R_{gaps}^{-1}\right)^{-1} \tag{31}$$

TIMs are commonly used in power electronics between heat sinks and PCBs and internal heat sinks and individual components and represent a significant portion of the thermal management industry.

1.5. Electrical insulation

Dielectrics (materials that do not conduct electricity) generally have low thermal conductivities and consequently large thermal resistances if they are thick. Electrically insulating material may therefore be a significant bottleneck to heat transfer, as is the case with FR4 in printed circuit boards for example. In many power electronics systems, such as Delta-Q’s battery charger, the heat sources must be separated from heat sinks with dielectric material. Clearly in this application a TIM that simply fills the gaps between real solid spots, such as thermal grease will not suffice. A dielectric material between two metals (device and heat sink) forms a capacitor which in turn can cause parasitic capacitive currents through the heat sink. This electromagnetic interference (EMI) is highly non-desirable in a power electronics system and must be carefully tested for [20]. Thick dielectrics are poor capacitors compared to thin ones and are therefore more desirable from an EMI perspective. Common electric insulators include polyimide films, silicone pads, Kapton films and alumina insulators.

1.5.1. Electrical insulation in Delta-Q's battery charger

Delta-Q's IC650 battery charger is depicted schematically in Fig. 12. There are two main types of components broadly categorized as surface mounted devices and through-hole. The surface mounted devices represent 52 W of the 87 W emitted by the charger and the through-hole devices the balance equal to 35 W. The surface mounted devices are mounted directly on the PCB which is then bolted to the heat sink. Heat emitted by these devices travels primarily through the copper thermal vias in the PCB through an electrically isolating material and into the heat sink. The through-hole devices are cooled primarily via a thermal epoxy that attaches them to the heat sinks. The thermal epoxy is also a dielectric. In both cases, materials that electrically insulate the live devices from the heat sink are directly in the heat transfer path and contribute significant thermal resistance. The cooling of the surface mounted devices is the practical starting point of this thesis as they represent 60% of the heat generated in the charger.

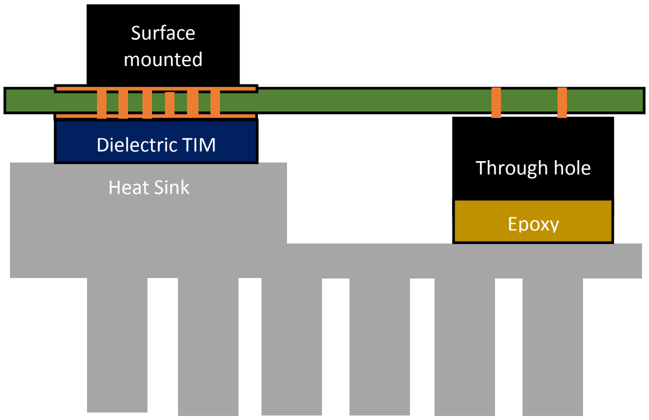

Fig. 12: Electrical insulation in Delta-Q's IC650 Battery Charger

1.5.2. Alumina

Alumina or aluminum oxide is an engineered ceramic with the chemical composition Al_2O_3. It is a common electrical insulator in power electronics often used with a purity of 92%. Alumina is also used as a grinding material because it is one of the hardest materials in the world. Alumina, like other engineered ceramics, can withstand very high temperatures and is therefore a common material for refractory insulation. Alumina insulators or substrates are manufactured by sintering aluminum oxide grains at high temperatures and pressure. Substrates can be lapped or polished with diamond paste if desired. The thermal contact resistance between alumina and metals has not been widely studied. It is the focus of much of this thesis.

1.6. Objectives and chapter contents

In this thesis, the TCR between alumina and metals is investigated to enable the prediction of battery charger thermal performance with ceramic insulators and to minimize the thermal resistance between heat generating discrete power devices and the fully sealed heat sink in Delta-Q's charger. The thermal resistance of common electrical insulators and alumina with and without TIMs is the focus of chapter 2. This chapter was presented as a conference paper at Semi-Therm 18 in San Jose California in March 2018 [19]. The validity of metal-metal TCR models is explored in chapter 3 by measuring the TCR between ceramics and bead-blasted stainless steels under vacuum and atmospheric pressure. This chapter has been prepared for submission as a manuscript for journal publication. Chapter 4 includes an experimental investigation of the TCR between cast, anodized and aluminum and as-fired, lapped and polished alumina. Influence of TIMs on these surfaces is also investigated in chapter 4. A version of this chapter has also been prepared for submission as a manuscript for journal publication.

Chapter 2. Electrical insulation for discrete power devices

In power electronic systems, TO-220 packaged electronic devices are bolted or clamped to metal heats sink for cooling. When mounting high voltage TO-220 devices to touch-safe heat sinks, electrical insulation must be used between the device and the heat sink. This chapter experimentally explores the thermal resistance between bolted and clamped TO-220 packages and the heat sink due to the electrical insulator. Aluminum oxide insulators are experimentally compared to commercially available polyimide thermal interface materials. Various TIMs are explored to reduce the thermal contact resistance at the alumina/metal interface including screen printed phase change material. Results show that thermal contact resistance at the alumina interface is significant under both clamped and bolted TO-220 diodes but can be reduced up to 70% with graphite sheets, thermal grease or phase change material.

2.1. Introduction

Power diodes and transistors, integrated either in power modules or as individual discrete packages, are among the most common components in power electronics [45]. The lower cost transistor outline (TO) series components, such as the TO-220 and TO-247, are widely used in lower current applications such as on-board electric vehicle battery chargers. When operating at high voltage they require electrical insulation before mounting onto touch-safe heat sinks. The electrical insulation adds additional thermal resistance to the heat transfer from device to ambient. In some cases, the electrical insulation may represent the largest thermal resistance in the heat path. Increasing thermal resistance without decreasing power results in an increase in device temperature which in turn results in an exponential increase in device failure rate [8]. Common electrical insulators include polyimide films coated with thermal interface materials (TIMs) to reduce the thermal contact resistance (TCR) developed between both imperfect contact interfaces (device/insulator and insulator/heat sink). Alternatives to polyimide films include ceramics which, as seen in Table 1, have thermal conductivities orders of magnitude larger than most dielectrics [9]. However, since they have lower dielectric strengths than other dielectrics, ceramics used to isolate high voltage devices must be relatively thick. This additional thickness is beneficial in reducing electric capacitance between device and heat sink, which can mitigate common mode EMI noise from high frequency power device switching.

Low cost ceramic insulators, such as alumina, are not usually sold with integrated coatings or TIMs. Alumina is a hard material and thus will suffer from high TCR when in bare contact with metals. When ceramics are used to isolate discrete TO devices a reduction in bulk thermal resistance may therefore be offset by an increase in TCR.

Table 1: Typical electrical insulation properties [9], [46], [47]

Material	Thermal conductivity [W/m·K]	Dielectric strength [kV/mm]	Relative permittivity
Beryllium oxide	40 to 210	13	6.8
Aluminum nitride	170 to 220	10 to 15	8.7 to 16
Aluminum oxide	10 to 34	10 to 17	9.5 to 10
Polyimide film	0.1 to 1.2	120 to 300	3.5

Many studies have been published on the thermal performance of TIMs in the literature, some of which electrically insulate adequately for high voltage applications [48]–[50]. However, studies on dielectric TIMs are not common. Only a few studies have been published on TIMs with alumina as a contact material. In practice, when alumina is used in industry thermal grease is applied on the surfaces to reduce the TCR. It is known that thermal grease may pump out during operation and this may result in failure if not considered [48]. In addition, the application of thermal grease or any TIM to the alumina adds an additional manufacturing step on the assembly line.

In this chapter, a PCM TIM is screen printed onto both sides of an alumina insulator. The PCM and screen printing is provided by a thermal management supplier [Universal Science, Milton Keynes, United Kingdom]. It is believed that this alumina/PCM insulator will be more easily and reliably installed into a product on the assembly line than insulators with separate TIMs. The thermal resistance of the alumina insulator with screen printed PCM is measured under a TO-220 diode bolted and clamped to an aluminum heat sink. Commercially available polyimide insulators and various other TIM and alumina combinations are also tested in the same configurations.

2.2. Experimental setup

Figure 13 shows a schematic of the custom-designed test bed. Thermocouples [T type, OMEGA, ±0.5 °C] are epoxied to a TO-220 dual Schottky diode [100 V, ON Semiconductor] and to a custom-built water-cooled aluminum cold plate finished with a fly cutter on a mill and then polished with 400 grit sand paper. A thermal bath [Polystat 3C15, Cole Parmer] is used to cool the cold plate. The diode package is soldered to a PCB to facilitate splitting the connected power cables. The cables are connected to a programmable DC power supply [62012p-80-60, Chroma], and two additional wires are attached to the PCB traces next to the diode leads for voltage measurement across one of the two diodes in the TO-220 package. Control and data acquisition are performed using a desktop computer and a data acquisition module [NI CDAQ-9174, National Instruments] containing cartridges for recording thermocouple [NI 9213, National Instruments] and voltage measurements [NI 9205, National Instruments].

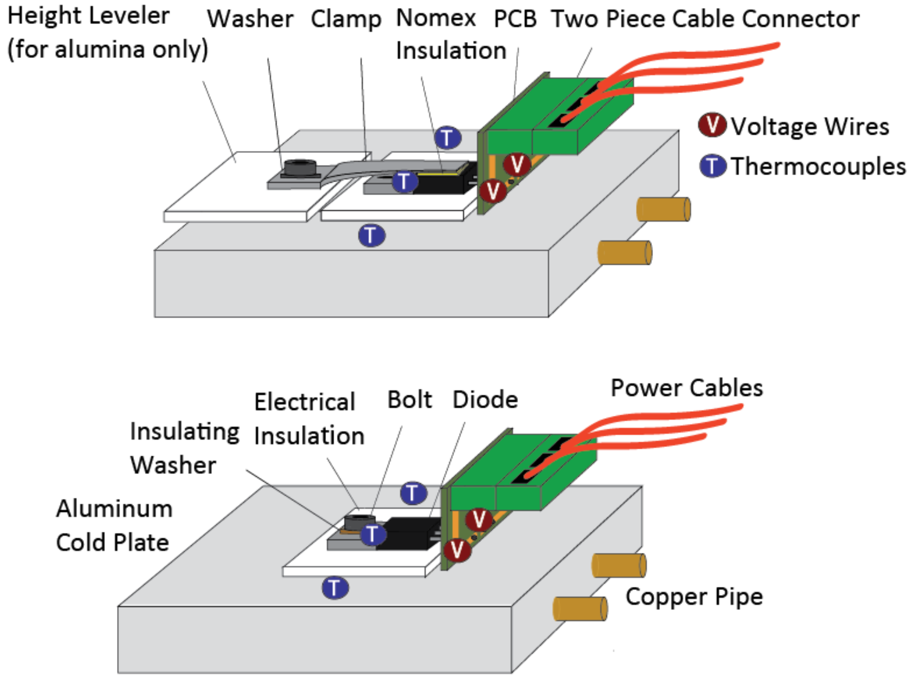

Fig. 13: Custom built experimental testbed for measuring the thermal resistance of TO-220 insulation.

Current is read from the power supply and recorded automatically by the control program written in LabVIEW. Prior to mounting, the cold plate surface is lightly rubbed with steel wool to remove any oxide layers and then both diode and cold plate are cleaned with isopropyl alcohol. The diode, washer and insulating material are mounted using an M3 bolt torqued to 0.56 N-m (5 in-lbs). For the clamped configuration, insulating paper (Nomex) is used between the bolted clip and the diode. To maintain the same clamping force, a bare alumina height leveler is placed under the clip when alumina is used to isolate the diode. After mounting, the cold plate is then insulated from the environment using glass wool and the power is turned on. Power supply voltage and current, diode voltage, diode temperature and cold plate temperature are recorded once steady-state is achieved. This is determined to be when temperature and voltage rates of change are below a certain threshold (1.25x10^-5) for a certain period of time (3 minutes). Extending the steady-state parameters had no significant effect on the results. Cold plate and alumina surface characteristics are provided in Table 2. Roughness and flatness deviation were measured using a profilometer (skidless diamond tip, Mitutoyo Surftest SJ-400, flatness resolution of 0.3 µm over 25 mm) after all thermal resistance measurements were conducted. The relatively large out-of-flatness of the cold plate along the width of the diode is due to the manual steel wool rubbing between runs.

Table 2: Average roughness and flatness measurements of contact surfaces

Sample	Root mean square roughness, R_q [µm]	Peak to peak maximum out-of-flatness deviation [µm]
Cold plate (along width of diode)	0.4	21.1 (concave)
Cold plate (along length of diode)	0.4	5.3
Alumina insulator	1.1	10.6

Electrical power is calculated using Eq. 32 by assuming both diodes in the TO-220 have the same voltage drop and that the voltage drop in the leads, solder and traces in the PCB are negligible.

$$\dot{Q} = P_e = \Delta V \cdot I \tag{32}$$

Thermal resistance is calculated using Eq. 33 by assuming that the temperature gradient in the aluminum cold plate is negligible compared to the temperature difference between the diode and the cold plate. In addition, losses to the ambient through the insulation and through the power cables are neglected.

$$R = \frac{T_d - T_{cp-avg}}{\dot{Q}} \tag{33}$$

2.3. Electrical insulators and thermal interface materials

Materials used to electrically insulate the diode from the cold plate are listed in Table 3. These materials are commercially available and were selected based on recommendations from an industrial partner of the project [Delta-Q Technologies, Burnaby BC Canada]. Though the list is not exhaustive, these products were selected because of their reasonable cost and frequent use in high voltage power electronics. All dielectrics used provide at least 4,000 V of dielectric breakdown voltage. Also included in Table 3 are one dimensional thermal resistance, parallel plate capacitance and dielectric breakdown voltage. Breakdown voltage, thermal conductivity and thickness are reported by the manufacturer while relative permittivity is approximated. Capacitance and thermal resistance are calculated using Eq. 34 and 35. The alumina insulator chosen has a dielectric breakdown voltage at least four times higher than the polyimide films and yet still has the lowest expected thermal resistance and capacitance. Decreasing the alumina thickness would result in even lower thermal resistance but higher capacitance.

$$C = \frac{\varepsilon_0 \cdot \varepsilon_r \cdot A_a}{t} \tag{34}$$

$$R_{1D} = \frac{t}{k \cdot A_a} \tag{35}$$

Commercially available TIMs used to reduce the TCR introduced by the alumina are listed in Table 4. Unique samples, developed to reduce assembly time, are shown in Fig. 14. The samples were created by screen printing phase change material onto both sides of the alumina insulators.

Table 3: Material properties of electrically insulating samples

Electrical insulator	Thermal conductivity [W/(m·K)]	Dielectric breakdown voltage [V]	Relative permittivity	Thickness [mm]	1D Thermal resistance [K/W] (1 cm x 1 cm)	Parallel plate capacitance [pF] (1 cm x 1 cm)
Adhesive coated polyimide tape	0.40	6,000	3.5	0.203	5.00	15.5
PCM coated polyimide film	0.46	4,200	3.5	0.05	1.08	61.9
Alumina	15	26,533	10	1.57	1.04	5.64

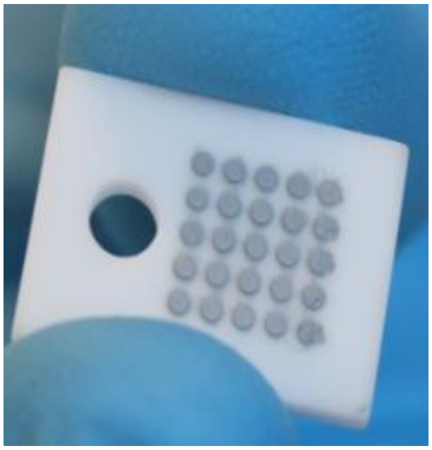

Fig. 14: Screen printed PCM onto alumina insulator courtesy of Universal Science [Milton Keynes, UK].

Table 4: Reported properties of non-electrically insulating TIMs for alumina

Alumina TIMs	Thermal conductivity [W/(m·K)]	Thickness [mm]
Synthetic graphite 400	400 (in-plane) 28 (through-plane)	0.2
Synthetic graphite 700	700 in-plane	0.1
Silicon-based thermal grease	2.3	-
Cured gap filler	3.6	-
Screen printed PCM on alumina	3.5	-

2.4. Experimental results

Thermal resistance results for a TO-220 diode bolted and clamped with electrical insulation are provided in Fig. 15. The experimental uncertainty, which is plotted as error bars, includes both calculated uncertainty and the standard deviation of the measurements. The standard deviation of the alumina without any TIM is much higher than for the other samples.

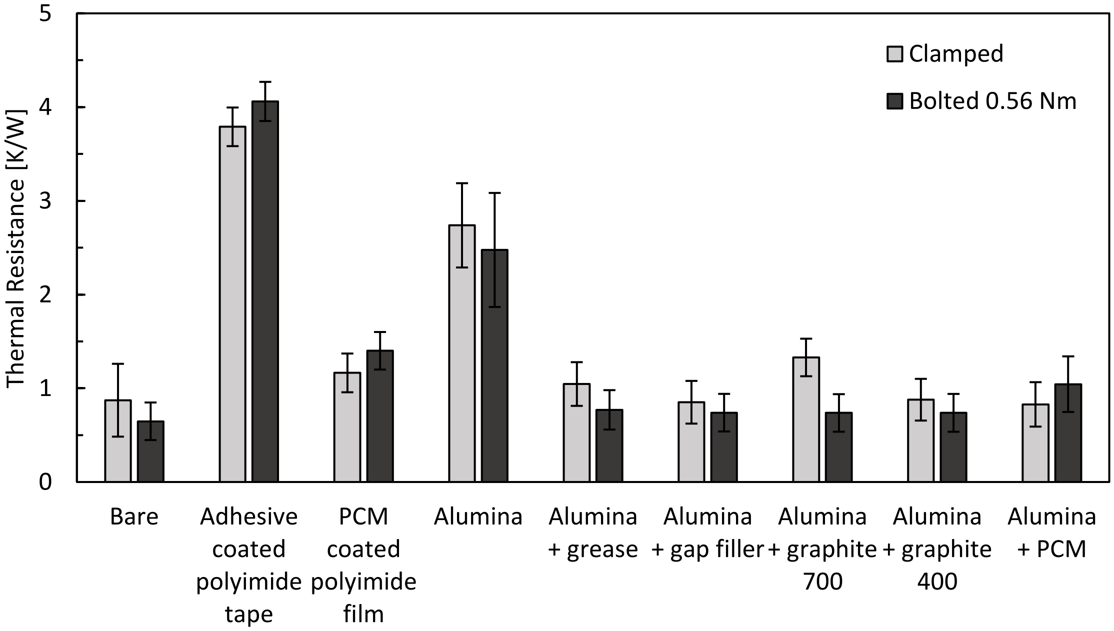

Fig. 15: Thermal resistance of TO-220 power diodes clamped and bolted with electrical insulation.

This may be due to mounting misalignment, mounting pressure variation and changes in the surface of the diode and the cold plate with individual runs. When TIMs are used high standard deviation is not observed as the conforming material reduces the result's dependency on pressure, roughness and non-conformity of the contact. Uncertainty analysis equations are shown in Eq. 36 through 39.

$$\frac{u_{\dot{Q}}}{\dot{Q}} = \sqrt{\left(\frac{u_{\Delta V}}{\Delta V}\right)^2 + \left(\frac{u_I}{I}\right)^2} \tag{36}$$

$$u_{\Delta T} = \sqrt{(u_T)^2 + (u_T)^2} \tag{37}$$

$$\frac{u_R}{R} = \sqrt{\left(\frac{u_{\Delta T}}{\Delta T}\right)^2 + \left(\frac{u_{\dot{Q}}}{\dot{Q}}\right)^2} \tag{38}$$

$$u_{R\cdot\sigma} = \sqrt{(u_R)^2 + (\sigma)^2} \tag{39}$$

The thermal resistances range from 0.65 K/W for a bare un-insulated diode up to 4.1 K/W when the diode is insulated with adhesive coated polyimide tape. Alumina, without any TIM, is the second worst insulator tested. The alumina insulators have a lower thermal resistance than the polyimide films tested however the high TCR at both the diode and cold plate interface results in a higher total thermal resistance. The polyimide films are both coated with a material that reduces this TCR. When thermal grease, gap filler, graphite or PCM is used on both sides of the alumina the reduction in thermal resistance is as high as 70% which confirms that TCR is a major bottleneck to heat flow on alumina/aluminum interfaces. Performance differences between the TIMs used are not discernible on this testbed as the error bars are overlapping. Relatively thick layers of grease and gap filler were used on the alumina surfaces. This may have been required due to the out-of-flatness of the cold plate surface. The average pressure distribution under the diode is shown for both diode configurations in Table 5. The average pressure under the bolted configuration is an approximation calculated using Eq. 40 and 41 with a friction factor of 0.2.

$$F = \frac{T_b}{f \cdot D_b} \tag{40}$$

$$P = \frac{F}{A_a} \tag{41}$$

Only Eq. 41 is necessary for the clamped configuration where it is assumed the applied force is equal to the rating of the clip (50N).

Table 5: Average pressure distribution at TO-220/alumina and alumina/cold plate interfaces

Configuration	Average pressure under diode [kPa]	Average pressure under alumina [kPa]
Bolted 0.56 Nm	6,517	3,260
Clamped 50 N clip	333	167

Despite the different average and distribution (uniform and non-uniform) of the contact pressures the experimental results show that there is no discernible thermal difference between clamped and bolted TO-220s when using electrical insulation as the differences fall within the error bars. This may be because under the bolted configuration, the average non-uniform contact pressure is higher than the clamped configuration but it is located further from the die location in the package. In both setups, heat may bypass the insulating TIM and travel through the bolt or the clip assembly. The differences in thermal resistance of these paths may also influence the result. Differences in thermal resistance due to temperature were not discernible on this testbed.

2.5. Conclusion

Results for the thermal resistance of a bolted and clamped TO-220 with screen printed PCM on alumina as electrical insulation are presented along with commercially-available insulator and TIM combinations. No discernible differences are observed between the clamped and bolted configurations despite the different contact pressures in both configurations. The alumina with TIM combination was competitive with respect to the commercially available polyimide film products despite offering higher breakdown voltage and lower capacitance. Its thermal resistance approaches that of the bare TO-220 without a TIM. To reduce experimental error, standardized tests are recommended for further quantifying the differences between TIMs and electrical insulators used for power packages. More detailed surface characterization may also be required.

Chapter 3. Thermal contact resistance of ceramic-metallic surfaces

Engineered ceramics are widely used in a variety of industries in demanding thermal environments. As seen in chapter 2, the thermal contact resistance (TCR) between ceramic insulators and metallic heat sinks can be a significant bottleneck to heat transfer. Despite this, existing TCR literature has for the most part focused on metal-metal contacts. In this chapter, the thermal contact resistance (TCR) between aluminum oxide, alumina nitride and stainless steel is experimentally measured using the guarded heat flow meter technique, as per ASTM E1530 [15]. Tests were conducted both under vacuum and under atmospheric pressure in order to compare results with existing metal-metal TCR models.

3.1. Introduction

Engineered ceramics are used extensively in demanding operating conditions due to their exceptional material properties. Examples include the use of aluminum nitride in electronic and power electronic packaging which has a thermal conductivity similar to aluminum yet does not conduct electricity. Aluminum oxide is frequently used as a grinding material for its hardness, as a thermal insulator in refractories due to its high melting point and as an electrical insulator because of its high dielectric strength.

In applications where thermal management is critical, such as electronics cooling, thermal resistance both within and at the interfaces of engineered ceramics can significantly influence heat transfer. The ability to model and predict heat transfer in such assemblies is critical for proper thermal design and thus reliability of such devices. The bulk thermal resistance of ceramics can be readily estimated knowing its thermal conductivity using standardized tests such ASTM E-1530 [15]. Spreading and constriction thermal resistances, i.e., the resistance due to cross-sectional area changes in the heat path, may be calculated using available correlations [51], [52] or FEA software. TCR is the resistance to heat transfer through imperfect mating surfaces, on the other hand, is more difficult to predict because it is a function of microscale surface features (e.g. surface roughness and out-of-flatness) as well as material surface properties (e.g. surface micro-hardness) that do not necessarily reflect the bulk material properties [38].

Our current knowledge of TCR is due to the work of many researchers who for the most part focused on metal-metal contacts [10]. In a vacuum, heat is limited to flow through the solid contact points at the interface between the surfaces as radiation heat transfer contribution is negligible when joint temperatures are below 600 °C [53]. To simplify the analysis, many studies have divided this solid resistance into micro and macro thermal contact resistances [17]. Micro-resistance is caused by microscale imperfections commonly referred to as surface roughness while macro-resistance is caused by surface curvature, out-of-flatness or macro-scale periodic imperfections (waviness) [17].

Cooper, Mikic and Yovanovich developed the famous CMY model for conforming (negligible macro imperfections) rough contacts which assumed a Gaussian roughness distribution, equivalent joint material and surface properties and plastic deformation of roughness peaks (asperities) [54]. Conforming rough models may be coupled with non-conforming smooth (negligible micro imperfections) models to cover non-conforming rough contacts [17]. At atmospheric gas pressure, heat may pass through air gaps (both micro and macro) as well as through the solid contact spots, again radiation is typically neglected. Bahrami et al. [16] and Song et al. [41] gas gap models cover a wide range of Knudsen numbers. A more detailed review can be found in Madhusudana's book [55] and Yovanovich's review paper [10]. Metal-metal contact has dominated TCR research as metals are good thermal conductors and are the most common materials used in thermal management systems. However, ceramic TCR has not been widely studied and TCR between ceramic and metals even less so.

Marotta and Fletcher studied refractory ceramic coatings on metal substrates in contact with bare aluminum [13]. Only 2 of the 8 test cases matched Yovanovich and Antonetti's model [56] at high contact pressures while none of the coatings matched Yovanovich and Antonetti's model [56] or Yip's model [57] at lower contact pressures [13]. The authors believed it might be due to out-of-flatness or incorrect thermal conductivity of the coatings [13]. Chung et al. studied metallic coatings on aluminum oxide substrates [14]. Their aluminum and copper coatings improved thermal contact conductance by 30%. They did not compare their experimental results with any of the available models in the literature. Mirmira and Fletcher studied interfacial contact resistance between stacks of single crystal ceramics and proposed a correlation to fit their experimental results [58].

Some experimental results did match existing metal-metal models. The experiment conducted by Aikawa and Winer on sintered silicon nitride contacts fit the modified Greenwood-

Williamson contact model [12]. Similarly, Rao et al.'s experimental TCR results on Al2O3/Al-AlN metal matrix composite joints [11] were close to both Mikic's model [59] and Sridhar and Yovanovich's model [60].

The thermal resistance of joints made up of dissimilar materials is an active research topic [61]. Ceramics and metals transfer heat through different methods; metals transport heat via free electronics while heat transfer in ceramics relies heavily on lattice vibrations (phonons) [62],[61]. Research on thermal boundary resistance (TBR), which is the resistance at a perfect interface between different materials due to phonon-electron, phonon-phonon and electron-electron interactions, suggests that material pairs that differ greatly in their Debye temperatures may have higher TBR than more similar material pairs [63],[61]. This TBR is expected to be much less important than TCR due to imperfect mechanical contact [63].

Ceramics and metals are also different in their mechanical properties. From metal-metal studies, it is known that TCR is a strong function of surface micro-hardness (and/or elasticity), contact pressure and surface geometry [10]. Ceramics, and aluminum oxide in particular, are an order of magnitude harder than most metals. In addition to their extreme hardness, ceramics are brittle materials while metals are ductile. Under blunt indentation, ceramic deformation, though similar to metal deformation on a macro scale, is different from metals on a micro scale and is characterized by brittle cone fracture above the elastic limit [64]. These cracks may initiate further microcracks at high loads [64]. Finally, ceramic surfaces can be notably different from surfaces found in typical TCR experiments, such as bead blasted metals. Ceramics are formed from powders and sintered particles under high pressure and temperature. Depending on grain size and sintering parameters, these surfaces may contain dead end surface pores.

None of the TCR models currently available in the literature have been developed based on ceramic-metal contacts or porous, cone-fractured microcontacts. Perhaps this is because researchers have concluded that ceramic-metal contacts are not much different from metal-metal interfaces with respect to TCR. The experimental literature does not yet back up this hypothesis. Ceramic-metal contacts have only been explored in the form of coatings and these did not match the existing models. No experimental studies have been conducted on the TCR between bulk ceramic-metal contacts (without coatings). Despite the differences in geometric, mechanical and thermal characteristics (the triad disciplines of TCR modelling) between ceramics and metals, the existing literature, and Ref. [12] in particular, suggests that metal-metal models work well for some ceramic-ceramic contacts.

In this chapter, conforming rough TCR between bead blasted stainless steel 304 and aluminum oxide and aluminum nitride is measured using a guarded heat flow meter technique, as per ASTM E1530 [15]. Our experimental results are then compared with available statistical TCR metal-metal models and show that metal-metal models are in reasonable agreement with ceramic-metal joints.

3.2. Statistical TCR model implementation

Statistical TCR models used in this work all assume that one surface is rough and the other is perfectly smooth. The rough surface takes on the effective surface properties of both real surfaces. These properties are calculated with Eq. 42 to Eq. 44 while Eq. 45 is exclusively used for models that assume elastic deformation. Plastic models assume that the micro-hardness of the effective rough surface is equal to the micro-hardness of the softer material. Micro-hardness and not bulk hardness is recommended for plastic TCR models [38].

$$\sigma = \sqrt{\sigma_{metal}^2 + \sigma_{ceramic}^2} \tag{42}$$

$$m = \sqrt{m_{metal}^2 + m_{ceramic}^2} \tag{43}$$

$$k = \frac{2k_{metal}k_{ceramic}}{(k_{metal}+k_{ceramic})} \tag{44}$$

$$E = \left(\frac{1-\nu_{ceramic}^2}{E_{ceramic}} + \frac{1-\nu_{metal}^2}{E_{metal}}\right)^{-1} \tag{45}$$

The CMY model with plastic deformation [40], the CMY with elastic deformation [59] and Bahrami et al's scale analysis model [36], were selected for comparison with the present experimental results. The scale analysis model does not differ significantly from the CMY plastic model [36]. Both are used in this work because the scale analysis model, though easy to implement, has a scaling factor that was derived based on metal-metal TCR experiments. The appropriateness of this scaling factor for ceramic-metal joints is not known a priori. The CMY and the scale analysis models' equations are listed in Table 6. Implementation of the CMY model requires iteration on the microhardness and mean plane separation (from Eq. 46 to Eq. 52 excluding Eq. 48) between the two effective surfaces. The bulk material hardness is used as an initial guess for this iteration which is completed when the micro-hardness re-calculations are negligibly different. Equations 53 through 57 complete the CMY model for conforming rough contact. Correlations that simplify the CMY model implementation are available in the literature [10] but are not used in this work.

Micro-hardness is calculated only for the stainless-steel surfaces since the ceramic surfaces have expected microhardness [65] in excess of 3 times that of stainless steel, thus the effective joint microhardness is the stainless steel microhardness. Several correlations for microhardness coefficients, c1 and c2, used for the micro-hardness of stainless steel are available in the literature and two different ones (Eq. 46, Eq. 47 and Eq. 58, Eq. 59 and Eq. 60) are selected for this implementation of the CMY and scale analysis models. Equations 61 and 62 complete the scale analysis model for conforming rough contact. The CMY elastic model may be calculated from Eq. 48 and Eq. 49 to Eq. 57 excluding Eq. 52.

Equations 57 and 62 represent the micro thermal resistance due to imperfect contact at the conforming surfaces, caused by surface roughness of the mating surfaces. Under atmospheric gas pressure, TCR calculations require an additional model to calculate the resistance of the gas gaps in between the contacting surfaces. Two of these models are tabulated in Table 7, one being a simplification (Eq. 63 to Eq. 67 and Eq. 71) of the other (additional Eq. 63 to Eq. 70) [16]. Both models yield close results for the present tests. The simplified model of Bahrami et al. assumes that the gas gaps may be approximated by two parallel plates with apparent contact area held a distance equal to the mean plane separation apart from each other. In this work, the simplified model is used with the scale analysis model and the full gas-gap model is used with the CMY models so that both a detailed and a simpler model are compared with the results. Since the heat is limited to travel either through the solid contact points or through the gas, the gas resistance and the solid resistance are in parallel, as seen in Eq. 72.

Table 6: Summary of solid-solid micro-contacts thermal contact resistance equations

Eq. No.	Equation	Ref.
(46)	$c_1 = 7.339e^{(-0.001695)(T-25.2)}$	[40]
(47)	$c_2 = -0.279$	[40]
(48)	$\lambda_{elastic} = \sqrt{2}\,\mathrm{erfc}^{-1}(\frac{4\sqrt{2}\,P}{mE})$	[40]
(49)	$\lambda_{plastic} = \sqrt{2}\,\mathrm{erfc}^{-1}(\frac{2P}{H'})$	[40]
(50)	$a = \mathrm{erfc}(\frac{\lambda}{\sqrt{2}})\frac{\sigma}{m}e^{\frac{\lambda^2}{2}}\sqrt{\frac{8}{\pi}}$	[40]
(51)	$DV = a\sqrt{2\pi}$	[40]
(52)	$H' = c_1\left(\frac{DV}{10^{-6}}\right)^{c_2}$	[40]
(53)	$\frac{A_{real}}{A_{apparent}} = \frac{1}{2}erfc(\frac{\lambda}{\sqrt{2}})$	[40]
(54)	$n = \frac{\frac{1}{16}\left(\frac{m}{\sigma}\right)^2 e^{-\lambda^2}}{\mathrm{erfc}(\frac{\lambda}{\sqrt{2}})}$	[40]
(55)	$\psi = \left(1 - \sqrt{\frac{A_{real}}{A_{apparent}}}\right)^{1.5}$	[40]
(56)	$h_{solid} = \frac{2nak}{\psi}$	[40]

(57)	$TCR_{solid} = \frac{1}{h_{solid}A_{apparent}}$	[40]
(58)	$K = \frac{H_B}{H_{BGM}}$	[36]
(59)	$c_1 = H_{BGM}(4 - 5.77K + 4K^2 - 0.61K^3)$	[36]
(60)	$c_2 = -0.57 + 0.82K - 0.41K^2 + 0.06K^3$	[36]
(61)	$H' = c_1 \left(\frac{\sigma}{m\sigma_0}\right)^{c_2}$	[36]
(62)	$TCR_{solid} = \frac{0.565H'\left(\frac{\sigma}{m}\right)}{k_s F}$	[36]

Table 7: Gas gap equations

Eq. No.	Equation	Ref.
(63)	$\Lambda = \Lambda_0 (\frac{P_0}{P_g})(\frac{T_g}{T_0})$	[16]
(64)	$for\ diatomic\ or\ polyatomic\ gases,\ \ M_g^* = 1.4 M_g$	[16]
(65)	$\mu = \frac{M_g}{M_s}$	[16]
(66)	$\alpha_T = e^{-0.57\left(\frac{T_s - T_0}{T_0}\right)} \left(\frac{M_g^*}{6.8 + M_g^*}\right) + \left(\frac{2.4\mu}{(1+\mu)^2}\right)(1 - e^{-0.57\left(\frac{T_s - T_0}{T_0}\right)})$	[16]
(67)	$M = \left(\frac{2 - \alpha_{T1}}{\alpha_{T1}} + \frac{2 - \alpha_{T2}}{\alpha_{T2}}\right)\left(\frac{2\gamma}{1+\gamma}\right)\left(\frac{\Lambda}{Pr}\right)$	[16]
(68)	$when\ 0.01 \leq \frac{M}{\sigma} \leq 1,$ $f_g = 1.063 + 0.0471(4 - \lambda)^{1.68}\left(ln\left(\frac{\sigma}{M}\right)\right)^{0.84}$	[40]
(69)	$when\ \frac{M}{\sigma} \geq 1, \qquad f_g = 1 + 0.06\left(\frac{\sigma}{M}\right)^{0.8}$	[40]
(70)	$TCR_{gas} = \frac{1}{k_g A_a f_g}(M + \sigma\lambda)$	[40]
(71)	$TCR_{gas-simplified} = \frac{1}{k_g A_a}(M + \sigma\lambda)$	[16]
(72)	$TCR_j = \left(\frac{1}{TCR_{solid}} + \frac{1}{TCR_{gas}}\right)^{-1}$	[16]

3.3. Experimental setup

Thermal conductivities of the stainless steel 304 (2 mm and 4 mm thick) and 99.5% aluminum oxide (2 mm thick) samples were measured per ASTM E1530 using a guarded heat flow meter setup available at our lab [15]. ARMCO iron heat flux meters with a diameter of 25.4 mm (one inch) were used with six thermocouples located at the center of the flux meters 5 mm apart from each other and 10 mm apart from the edges. Aluminum nitride thermal conductivity was not measured because the combination of small sample thickness (0.4 mm) and high expected thermal conductivity (170 W/(m·K)) results in a negligible deviation in thermal resistance (0.002 K/W) with a reasonable difference (30%) in expected and actual thermal conductivity.

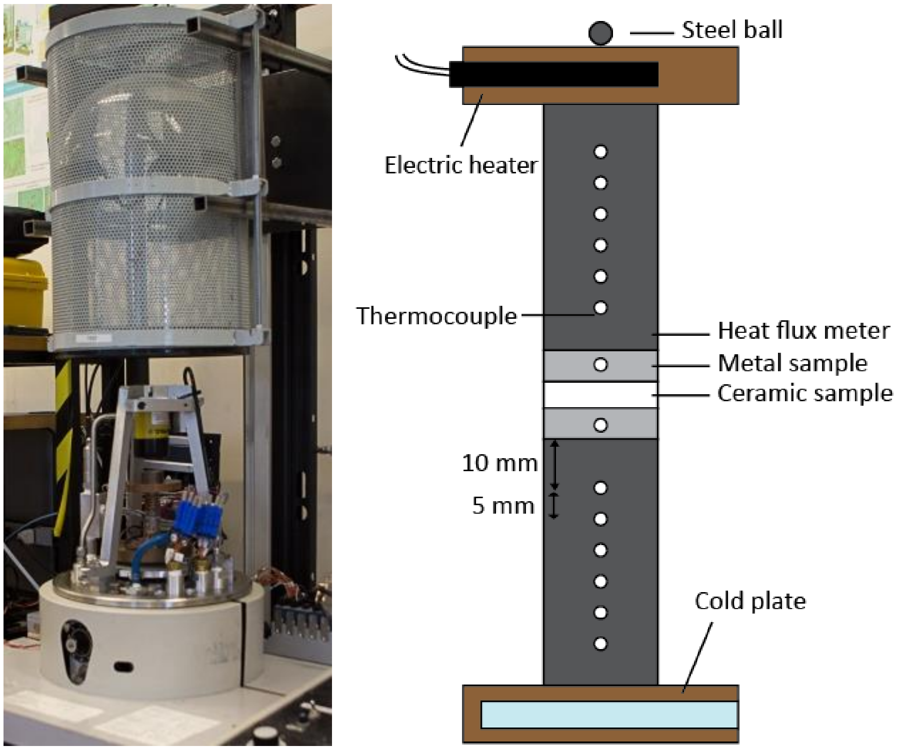

Fig. 16: Guarded heat flow meter experimental setup.

To measure the TCR between ceramic and metallic surfaces the same guarded heat flow meter setup was used. The heat flow through the joint was measured per ASTM E1530 using the cylindrical ARMCO iron heat flux meters. To measure the temperature difference across the metal-ceramic-metal joint thermocouples (Omega, T Type, ±1 °C) were inserted into each metal sample. All measurements were conducted with a single ceramic (or metal) sample in between two metal samples equipped with thermocouples. Thermocouples that exhibited minimal temperature (< 0.3 °C) difference in a hot water bath (from ambient to 100 °C) were selected for insertion into the metal samples.

To prepare the metal samples for the TCR experiment, stainless steel 304 disks were first turned on lathe, lapped (to ensure conforming contact) offsite and then bead-blasted at an in-house machine shop to create close to random (Gaussian) roughness. Measured surface roughness values are provided in Table 9.

All sample roughness and approximate flatness measurements (< 0.75 micron across sample diameter) were measured by profilometer (skidless diamond tip, Mitutoyo Surftest SJ-400, flatness resolution of 0.3 µm over 25 mm) in our lab. Polished and as-fired aluminum oxide and polished aluminum nitride 25.4 mm (1 inch) diameter disks were ordered from Ortech Advanced Ceramics and Stellar Ceramics, respectively.

TCR measurements were conducted both in a vacuum and under atmospheric gas pressure. First a rotary pump and then a diffusion pump were used to create a high vacuum. During measurement, vacuum pressure was maintained between 1.25 and 4 mPa ($4 \cdot 10^{-5}$ mbar or $3 \cdot 10^{-5}$ torr) and was measured with a Penning gauge. Thermal measurements were taken at steady-state conditions determined to be when the total thermal resistance between the heat flux meters changed less than 0.12% for over 30 minutes and 0.06% over 10 minutes. On average, tests exceeded 3 hours. Details of uncertainty analysis are provided in Appendix A.

Bulk material properties are tabulated in Table 8. Thermal conductivity, and roughness were measured in the lab. Approximate micro-hardness, bulk elasticity and Poisson ratio values were taken from the literature. Table 10 lists the experimental joints used in the experiment.

Table 8: Bulk material properties

	Thermal Conductivity [W/(m·K)]	Approx. Micro-Hardness [GPa]	Bulk Elasticity [GPa]	Poisson Ratio
AlN	170	10	300	0.24
Al2O3	25.2	15	300	0.21
SS304	16.8	3.4	200	0.29

Table 9: Surface properties

Properties	Measured RMS Roughness [µm]	Calculated Asperity Slope [rad]	Approx. Calculated Micro-Hardness [GPa]
Polished AlN	0.03	0.0092	10
Polished Al2O3	0.28	0.048	15
As-fired Al2O3	1.1	0.13	15
Lapped SS304	0.33	0.043	3.85
Bead-blasted SS304 control	2.8	0.13	2.9
Bead-blasted SS304 test	1.9	0.11	3.1

Table 10: Experimental joints

Joint Number	Metal Sample	Ceramic Sample
Joint 1	Lapped SS304	Bead blasted SS304 control
Joint 2	Bead blasted SS304 test	Polished Al2O3
Joint 3	Bead blasted SS304 test	Polished AlN
Joint 4	Lapped SS304	Polished Al2O3
Joint 5	Lapped SS304	Polished AlN
Joint 6	Lapped SS304	As-fired Al2O3
Joint 7	Bead blasted SS304 test	As-fired Al2O3

3.4. Porosity of ceramic samples

Engineered ceramic substrates like alumina and aluminum nitride are formed by sintering at high pressure. This process can produce pores in the finished surfaces depending on sintering conditions and grain sizes. Both ceramic samples, as described by the manufacturers, do not contain through hole pores. However, it is likely that the samples contain finite dead-end pores due to the nature of the sintering process. The grain sizes used to produce these ceramics are not known. Scanning electron microscope images were taken of the surfaces of the polished aluminum oxide and polished aluminum nitride samples. They are shown in Fig. 17 to 18 for aluminum oxide, and Fig. 19 to 20 for aluminum nitride.

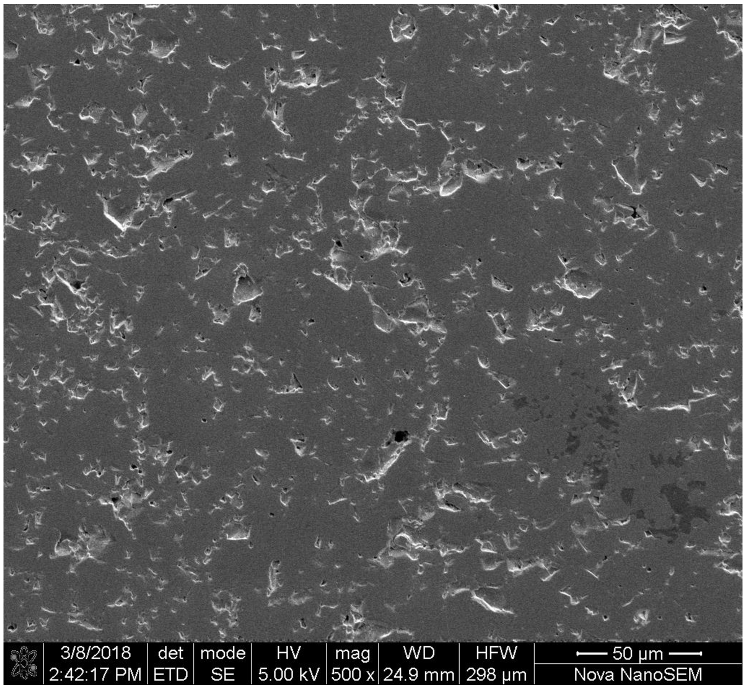

Fig. 17: SEM image of polished aluminum oxide at 500X magnification

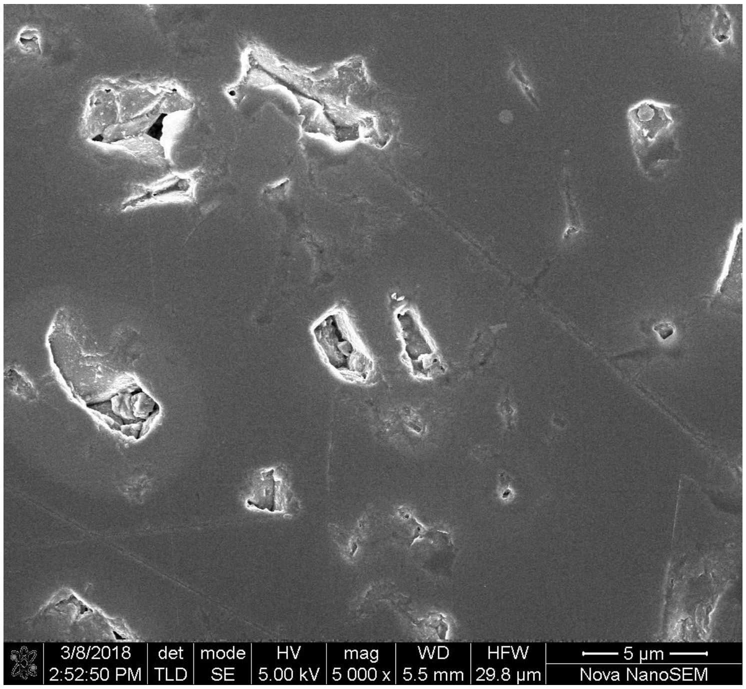

Fig. 18: SEM image of polished aluminum oxide at 5000X magnification

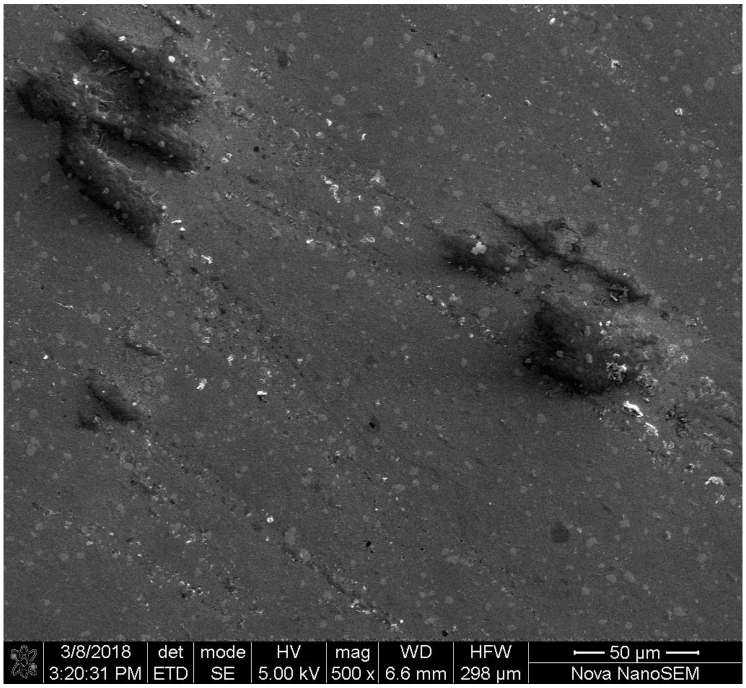

Fig. 19: SEM Image of Polished Aluminum Nitride 500X magnification

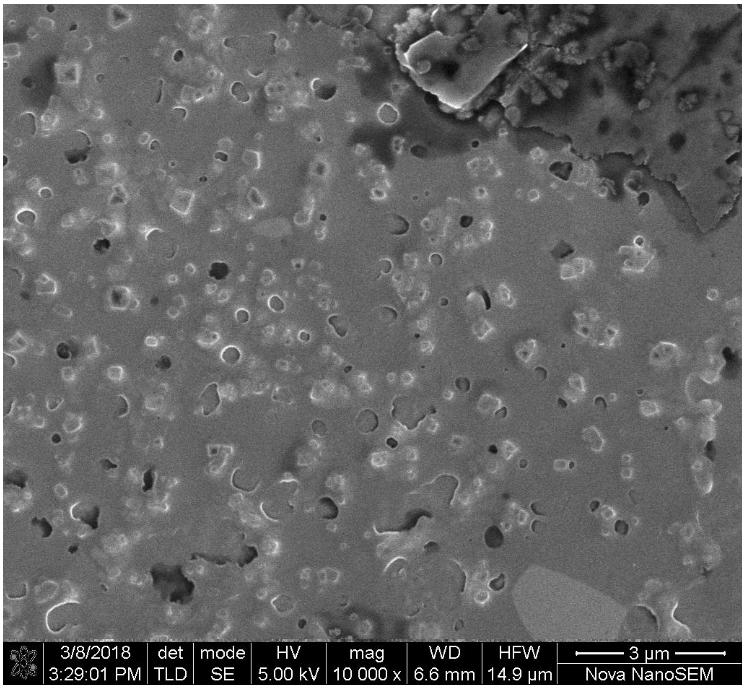

Fig. 20: SEM image of polished aluminum nitride at 10000X magnification

As seen in the images, the aluminum oxide surfaces contain what appear to be pores with diameters on the order of 1 to 10 microns and the aluminum nitride surfaces contain pores on the order of 0.1 to 1 microns. To take the SEM images both aluminum oxide and aluminum nitride surfaces were coated with a thin layer (several nanometers) of conductive material (iridium). SEM images were taken under high vacuum at 4D labs at Simon Fraser University Burnaby using their Nova NanoSEM machine.

To approximate the pore to surface area ratio images were analysed in ImageJ. The following procedure was used:

1. Scale image using legend (draw line and analyze, set scale)
2. Crop image to remove legend (image, crop)
3. Make the image binary (process, binary, make binary)
4. Draw outlines (process, binary, outlines) around the white edges and fill holes (process, binary, fill holes)
5. Analyze particles (analyze, analyze particles with include holes and min seize =0.01)

Two images analyzed by this process are included in Fig. 21-22 and Fig. 23-24.

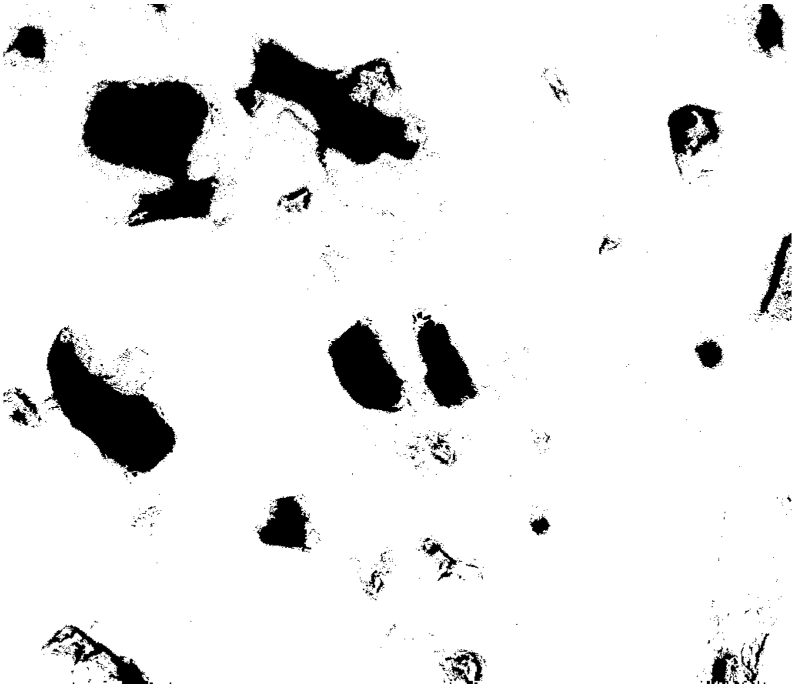

Fig. 21: Edited SEM image of polished aluminum oxide at 5000X magnification

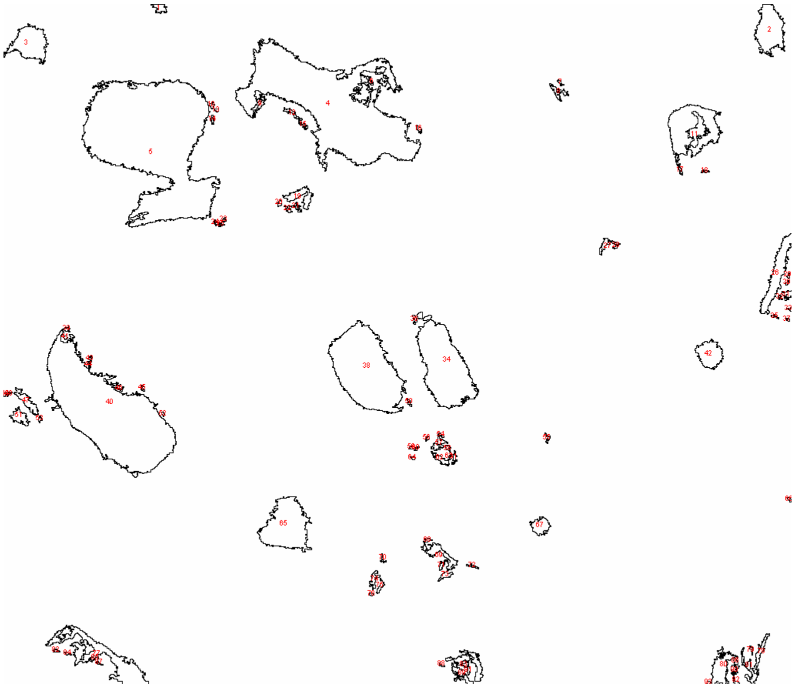

Fig. 22: Count of pores of SEM image of aluminum oxide at 5000X magnification

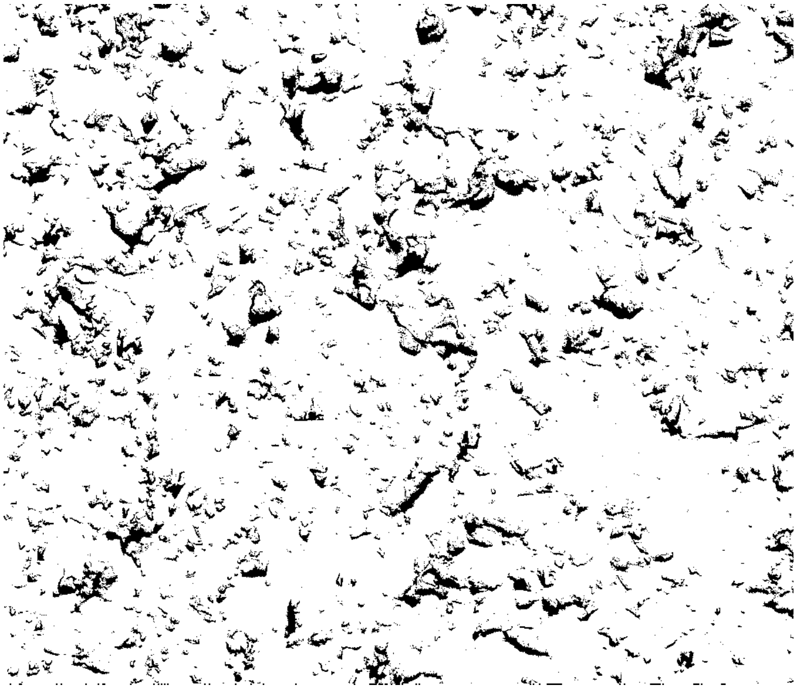

Fig. 23: Edited SEM image of polished aluminum oxide at 500X magnification

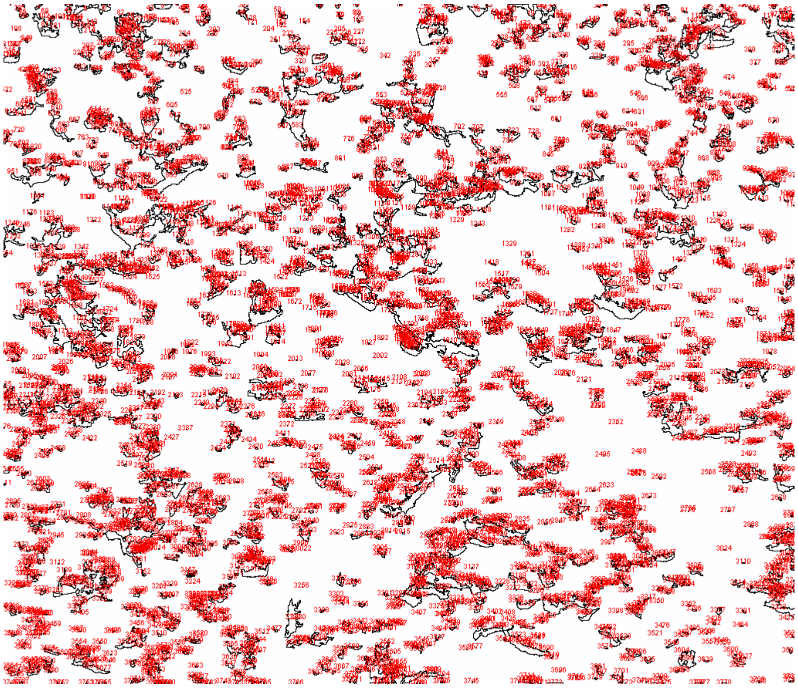

Fig. 24: Count of pores of SEM image of aluminum oxide at 500X magnification

The outlines defined in Fig. 22 and Fig. 24 may be open-ended pores. It is difficult to confirm this using SEM images because it is not always clear what is a valley and what is a peak.

This method of characterising the surface can be subjective. Using this method, the pore to area ratio of the aluminum oxide surfaces was 9.3% using 5 different images of the same surface. The aluminum nitride surface had a ratio of 8.3% using 4 different images.

Optical images were also taken of the polished aluminum oxide and polished aluminum nitride surfaces to confirm that the pores observed (particularly Fig. 20) were not due to flaking of conductive iridium coating required by SEM. The image analysis process in ImageJ is the same, except only a section of the image was chosen for analysis due to uneven lighting. Selected images are shown from Fig. 25 to Fig. 31.

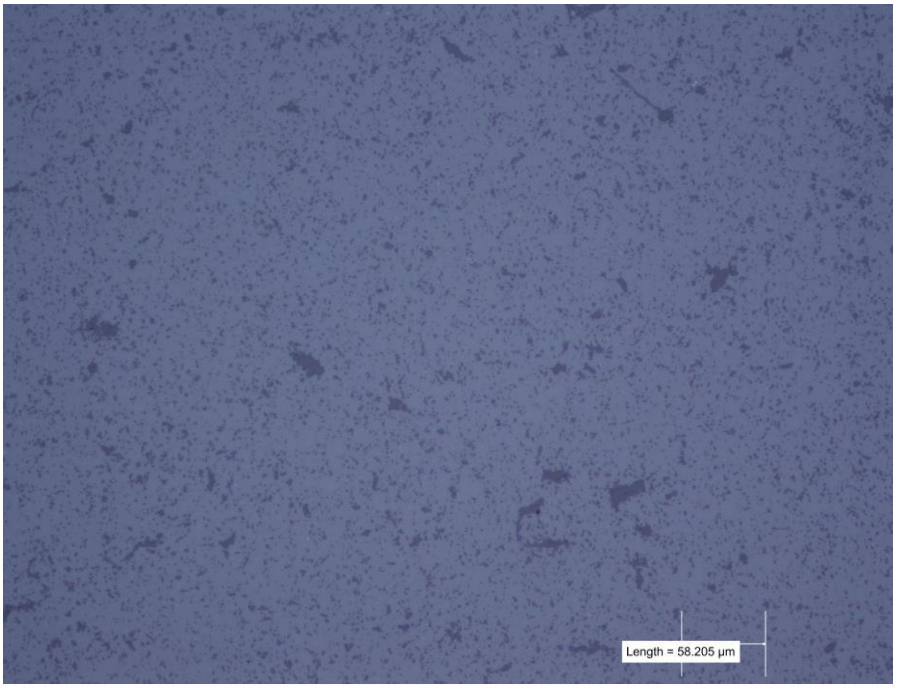

Fig. 25: Optical microscope image of polished aluminum oxide at 20x magnification

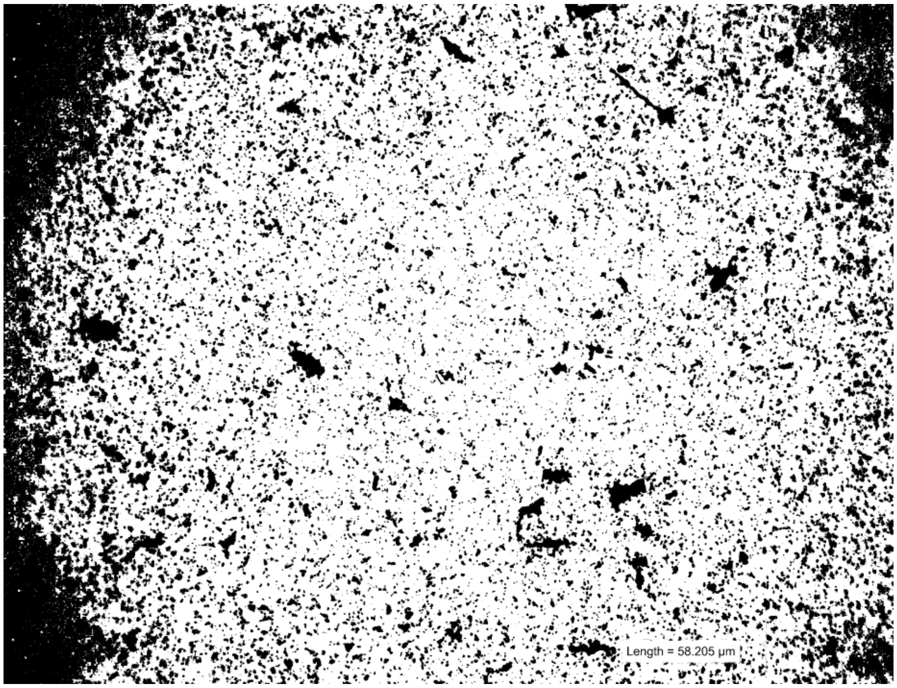

Fig. 26: Binary of optical image of aluminum oxide at 20x magnification

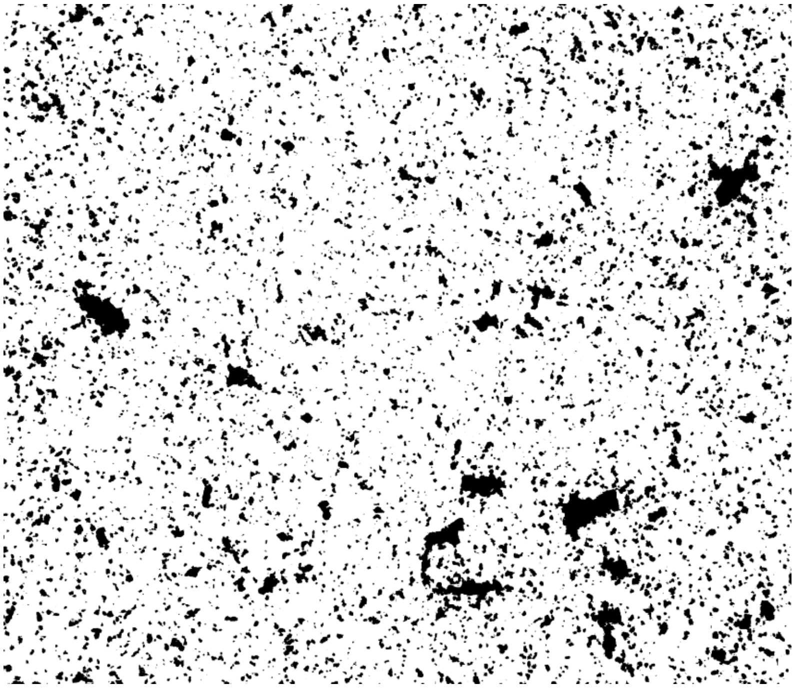

Fig. 27: Selection of binary of optical image of aluminum oxide at 20x magnification

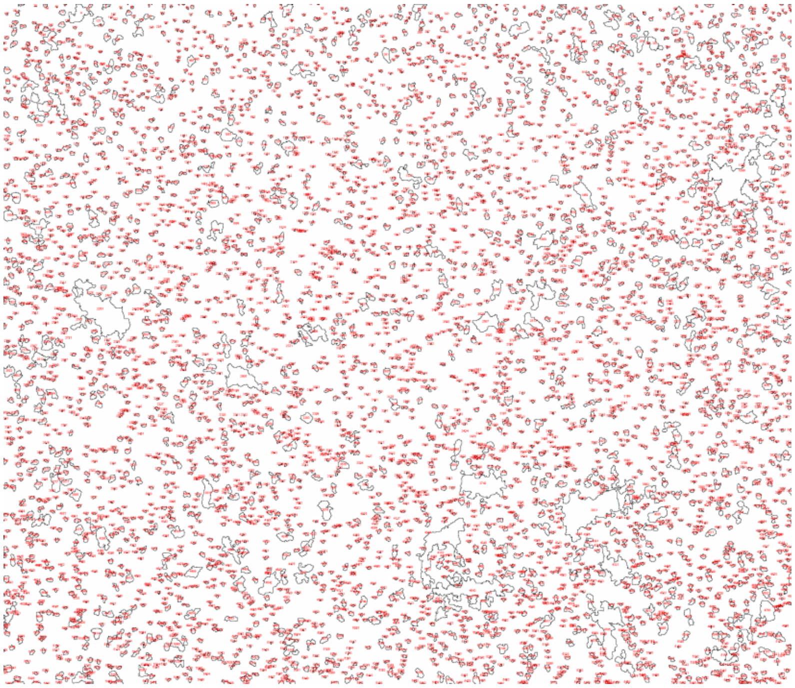

Fig. 28: Selected pores of aluminum oxide under optical microscope at 20x magnification

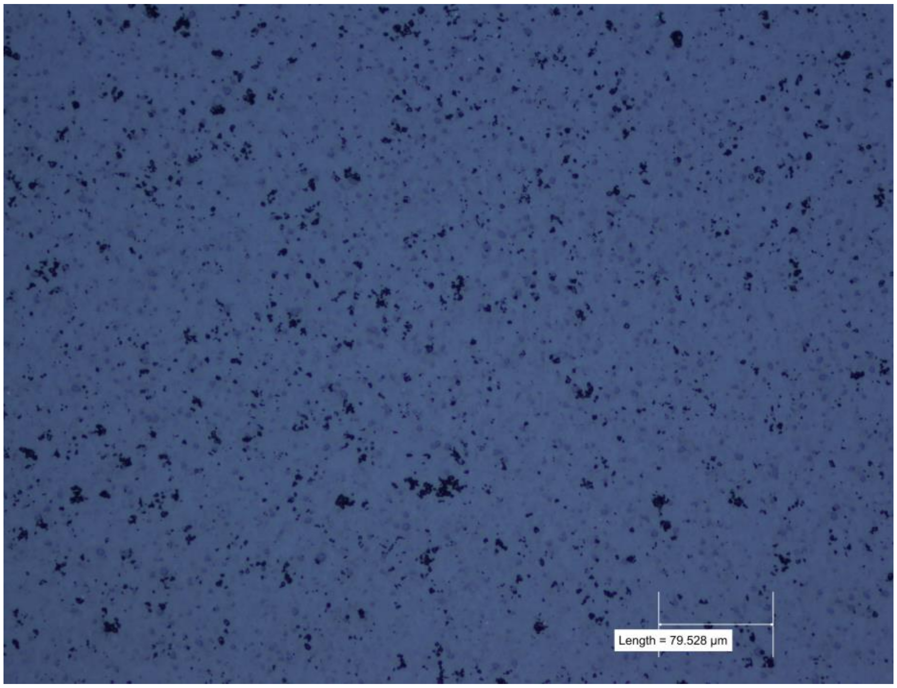

Figure 29: Optical microscope image of polished aluminum nitride at 20x magnification

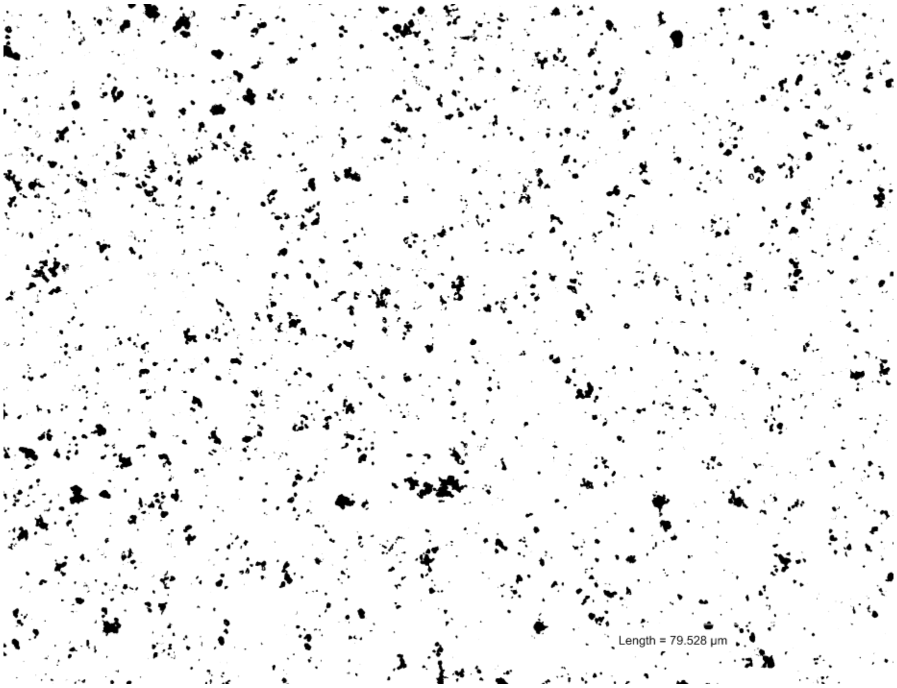

Fig. 30: Selection of binary of optical image of aluminum nitride at 20x magnification

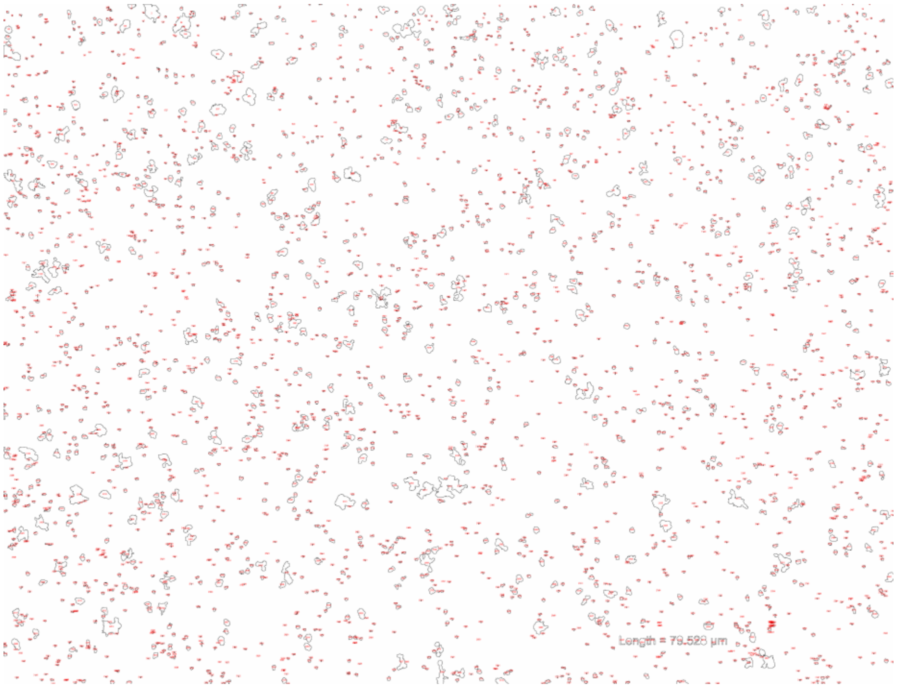

Fig. 31: Selected pores of aluminum nitride under optical microscope at 20x magnification

The average results from the optical images indicate that the pore to area ratio of the aluminum oxide surfaces and aluminum nitride surfaces are 14% and 8% respectively. It is however unclear whether all of the pores are indeed pores. They may in some cases be hills and valleys due to surface roughness. This data is therefore not used in the any of the models in this thesis. The pores will be captured fully by profilometer only if the profilometer tip diameters are smaller than the pore diameters. In general, this is not the case.

3.5. Experimental results

Thermal conductivity measurements of the stainless steel and aluminum oxide are presented in Fig. 32. The linear curve fits (y-intercept = 32.87 and slope = -0.08526 for alumina and y-intercept = 13.70 and slope = 0.03407 for stainless steel) in Fig. 32 were used to de-convolute the TCR from all the experimental results in this work.

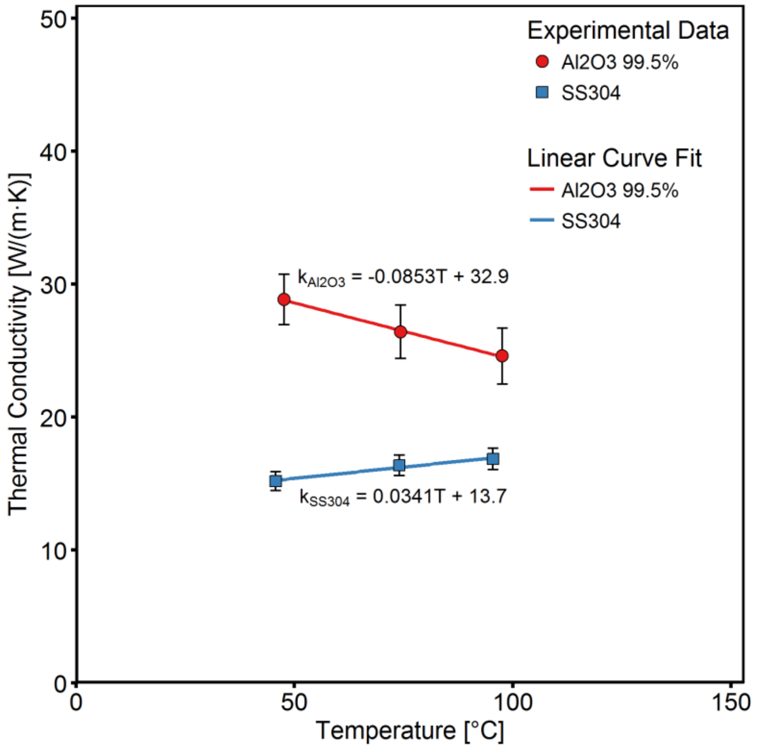

Fig. 32: Thermal conductivity and linear fits for alumina and stainless steel measured with the guarded heat flow method between 45 and 100 °C.

To investigate the repeatability of the results, the TCR of a metal-ceramic-metal joint (Joint 2) was mounted and measured 5 times (rotating sample and re-mounting each time) under atmospheric pressure. As seen in Fig. 33b, re-mounting the joint did not result in a significant difference in TCR in atmospheric pressure. Similarly, Fig. 33a illustrates the same test but done under high vacuum pressure (Joint 4).

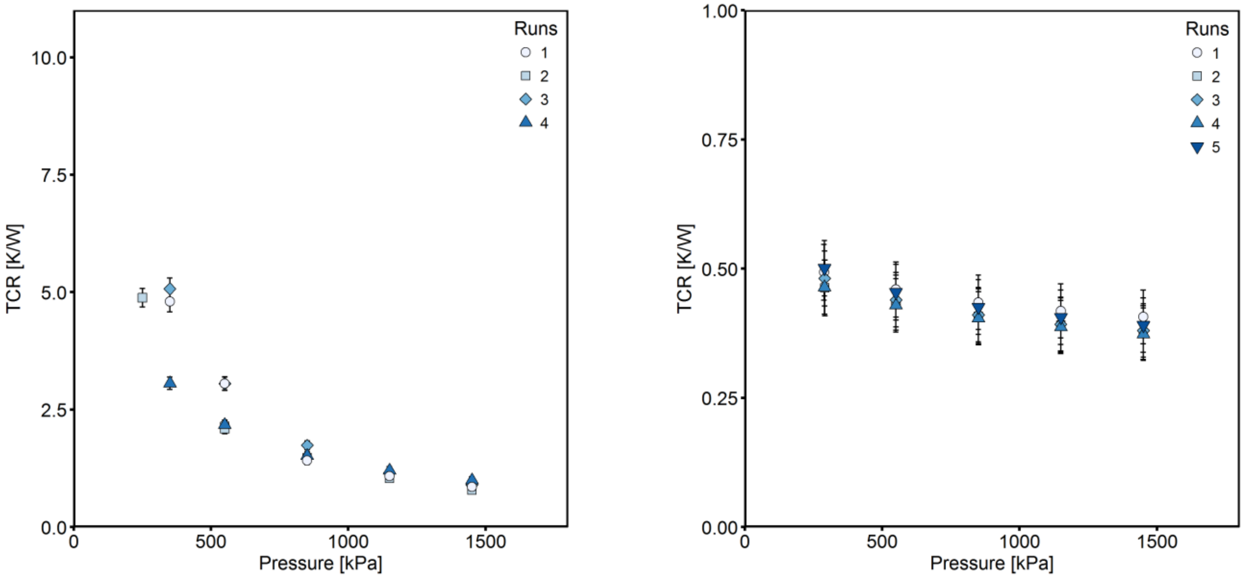

Fig. 33: a) Repeatability of TCR experiment under high vacuum pressure (Joint 4) and **b)** Repeatability of TCR under atmospheric air pressure (Joint 2)

The deviations in the results are insignificant at high contact pressure but become significant and are outside the expected uncertainty at low contact pressures. This is deemed reasonable considering that the sample was rotated and re-mounted in between each run and high random error is only present at low contact pressures, especially where TCR is most sensitive to initial contact area and hysteresis.

To provide a benchmark for comparison with all of the ceramic-metal tests the TCR between lapped stainless steel and bead-blasted stainless steel was measured both in vacuum and under atmospheric pressure. The experimental results for two different bead-blasted samples under vacuum are presented in Fig. 34a and those in atmospheric pressure in Fig. 34b along with the TCR models for conforming rough contact previously described. These samples were bead-blasted at different times and underwent lapping (before bead-blasting) at different machine shops. The results clearly show that one of stainless steel samples (blue) does not adequately follow the models, especially in vacuum. This sample underwent less lapping than the other stainless steel sample (before bead-blasting). Since the models were not capable of predicting the TCR at this stainless steel stainless steel interface, this sample was not used. The purpose of this study is to test the validity of metal-ceramic contacts with metal-metal models, not to illustrate the limitations of the models for non-gaussian metal-metal contact, though clearly from Fig. 19a, not all metal-metal contacts are captured with existing models.

Fig. 34c and Fig. 34d show the isolated control for the study. These bead-blasted stainless steel samples and lapped bead-blasted steel samples are used for the rest of the study.

The experimental data matches both plastic models under vacuum and atmospheric pressure in Fig. 34c and Fig. 34d. It is clear from Fig. 34c that the plastic deformation assumption of the asperities predicts the data more accurately for these contact pressures. Lambert and Fletcher's correlation for asperity slope as a function of surface roughness, Eq. 73, is used for the stainless steel surfaces in this study. This is done with confidence, despite associated error with asperity correlations on the order of 30%, because the TCR data is in good agreement with the model in Fig. 34c and Fig. 34d. Use of the measured asperity slope did not adequately capture the steel steel TCR (of either control sample) with these models. The cause for this is unknown but may be due to poor asperity slope measurement due to limitations of of the profilemoeter tip or the consequences of bead-blasting technique.

$$m_{SS304} = 0.076(\sigma)^{0.52} \tag{73}$$

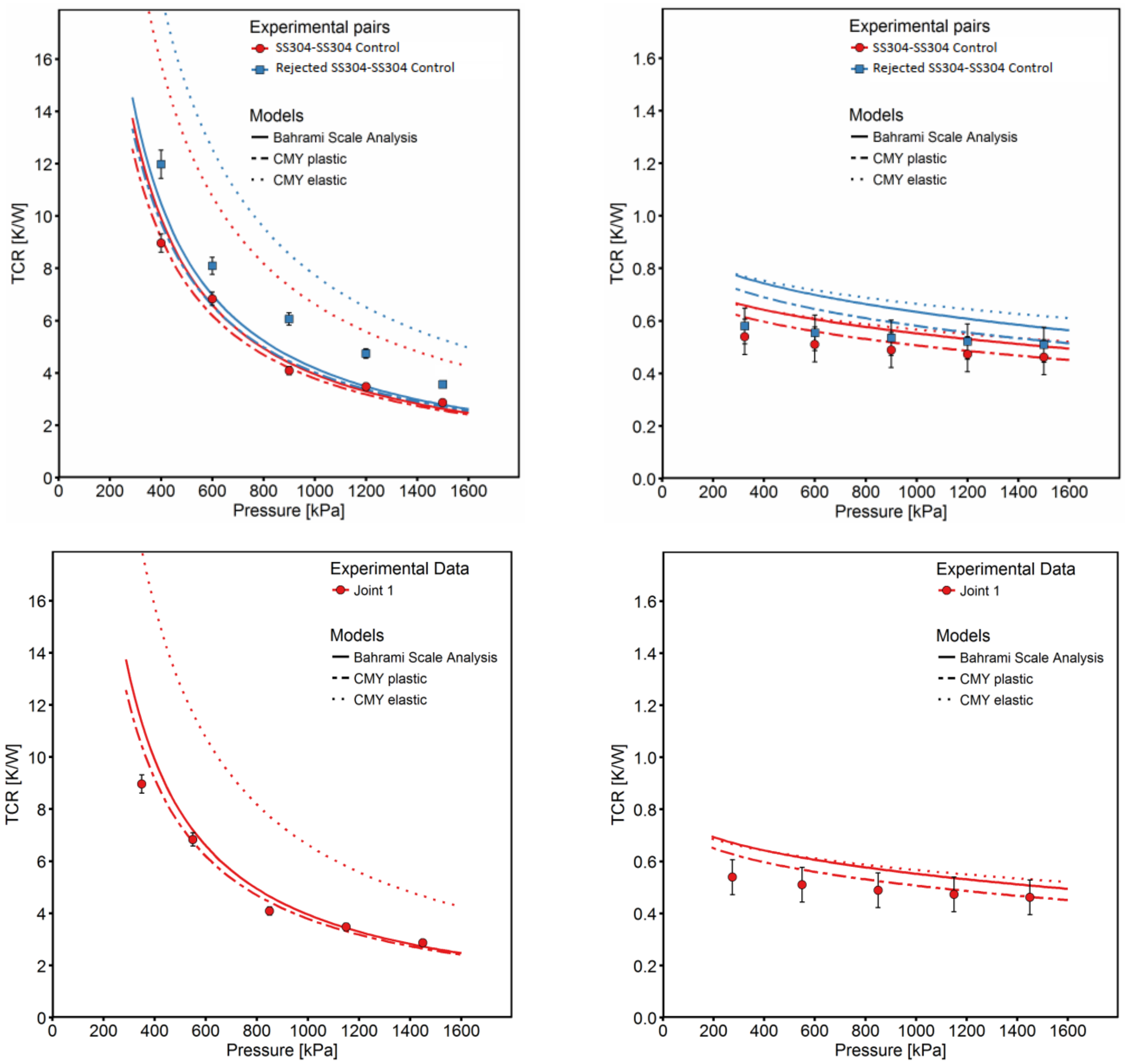

Fig. 34: a) TCR between lapped stainless steel and two different bead-blasted stainless steel samples under high vacuum; **b)** TCR between lapped stainless steel and two different bead-blasted stainless steel samples under atmospheric pressure; **c)** Control TCR between lapped stainless steel and bead-blasted stainless steel under high vacuum (14% RMS relative difference); **d)** Control TCR between lapped stainless steel and bead blasted stainless steel under atmospheric pressure (18% RMS relative difference) [40] [36] [16].

3.6. Rough metals and smooth ceramics

TCR results between polished ceramics and bead blasted stainless steel under high vacuum are presented in Fig. 35a. The same models using the material and surface properties of both the ceramic and the stainless steel are also shown. Again, the deformation of the asperities is assumed to be plastic. This is expected because the stainless steel is the rough surface and therefore it is the stainless steels' asperities that are deforming on the smoother ceramics. This is consistent with Mikic's plasticity index, shown in Eq. 74, which indicates plastic asperity deformation when less than or equal to 0.33 and elastic asperity deformation when greater than or equal to 3.0 [59]. Joint 1 (SS304 and SS304) has a Mikic plasticity index of 0.19, Joint 2 has a Mikic plasticity index of 0.21 and Joint 3's is 0.22.

$$\gamma_p = \frac{H'}{Em} \tag{74}$$

In Fig. 35b the TCR between these same samples is shown under atmospheric pressure. All the models fit the data within the uncertainty of the measurements. Under atmospheric pressure, the elastic models are not significantly different from the plastic models because the presence of the air in the joint reduces the sensitivity of the model to the deformation of asperities. In addition, the TCR is reduced by an order of magnitude with a gas in the joint, similar to metal-metal contact.

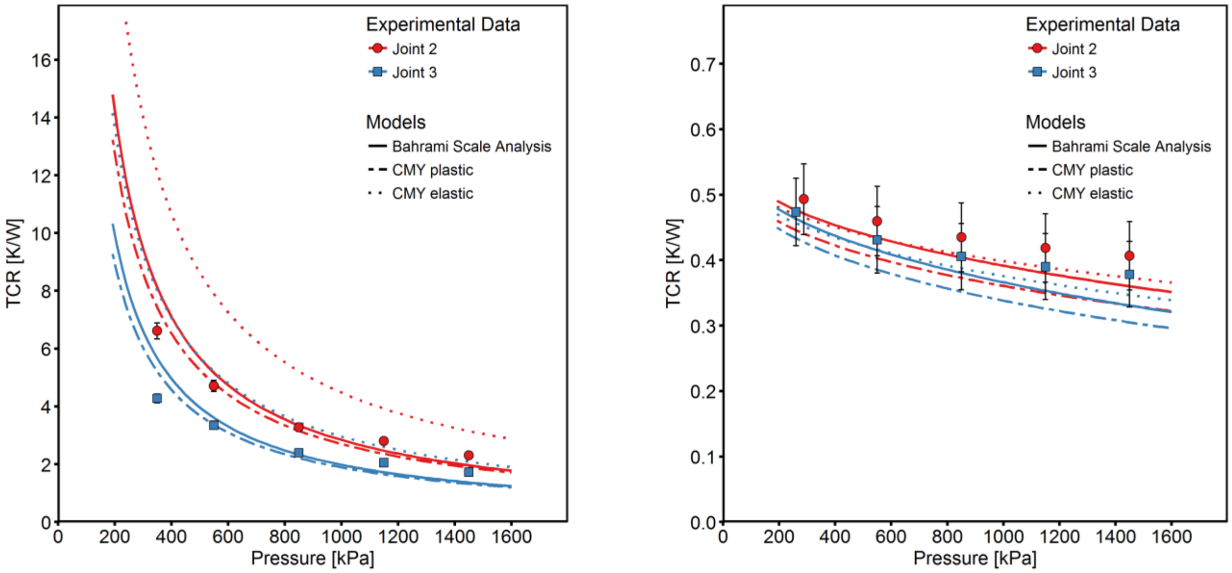

Fig. 35: a) TCR between bead blasted stainless steel and polished ceramic (Joint 2, 14% RMS relative difference; Joint 3, 13% RMS relative difference) under high vacuum **b)** TCR between bead blasted stainless steel and polished ceramics under atmospheric pressure (Joint 2, 7.9% RMS relative difference; Joint 3, 7.7% RMS relative difference) [40] [36] [16].

The correlation used for the average asperity slope of the ceramic is not influential on the result because the ceramic is much smoother than the stainless steel. It holds then that the stainless steel's asperity correlation is more influential on the models' results because its roughness determines the effective roughness and effective asperity slope in the model.

Due to the similarity between the metal-metal models and ceramic-metal data the plastic conforming rough contact metal-metal models are deemed appropriate for ceramic-metal joints when the metal is relatively rough, and the ceramic is relatively smooth. In addition, the elastic CMY model is also appropriate in atmospheric pressure only. Since the deformation of the asperities is plastic and both plastic models yield similar results for ceramic stainless-steel contacts, further figures only contain the scale analysis model for simplicity.

3.7. Rough ceramics and smooth metals

If the ceramic is rough and the metal is smooth, then it is expected that the metal sample will deform under the harder ceramic asperities. However, the metal-metal TCR models do not consider this as they assume that the effective rough sample is the softer material and the perfectly smooth sample is the material that experiences no deformation. To test if these models work despite this assumption, rough ceramics (polished and as-fired) were put into contact with smooth metals (lapped). Figures 36a and 36b show the results of this experiment in a high vacuum and atmospheric pressure. In both cases, the models are all in reasonable agreement with the experimental data which strongly suggest that the metal-metal models are appropriate for ceramic-metal joints despite the deformation assumption.

Antonetti's correlation, Eq. 75, for asperity slope as a function of roughness was selected for the ceramic surfaces because Fletcher and Lambert's correlation resulted in large difference from the model and experimental data.

$$m_{ceramic} = 0.124(\sigma)^{0.743} \tag{75}$$

It is reasonable that one correlation is appropriate for ceramics and less so for the bead blasted metals in this experiment because the surfaces are in truth formed by completely different processes. Again, for smooth metals with rough ceramics the correlation used on the stainless steel is not influential.

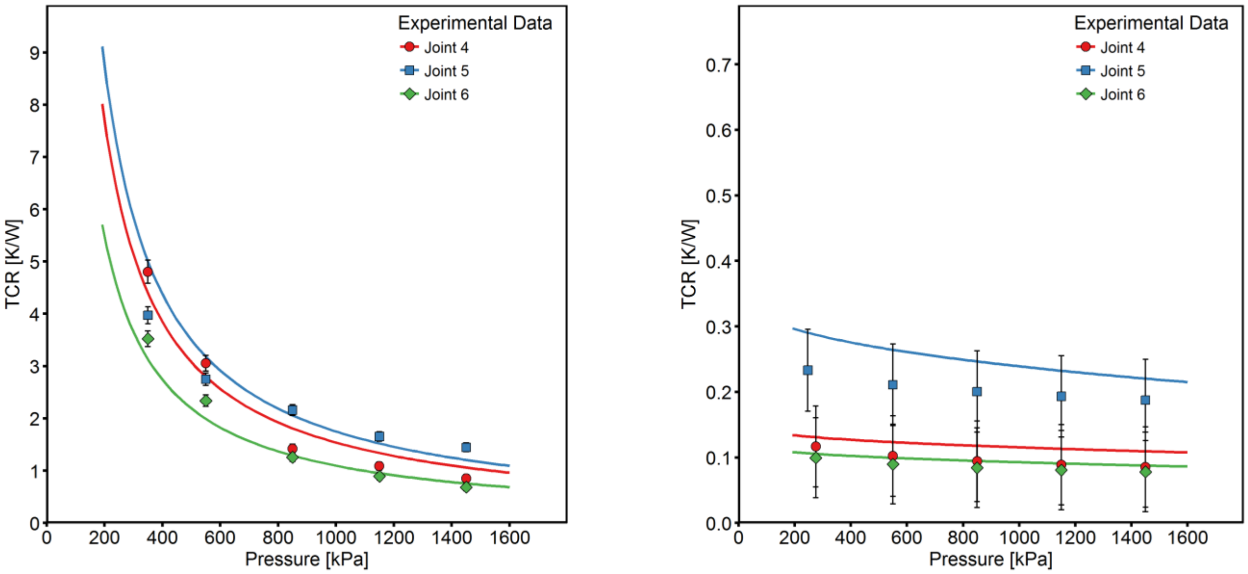

Fig. 36: a) TCR between ceramics and smooth stainless steel in high vacuum (Joint 4, 20% RMS relative difference; Joint 5, 9.9% RMS relative difference; Joint 6, 16% RMS relative difference) **b)** TCR between rough ceramics and stainless steel in atmospheric pressure (Joint 4, 24% RMS relative difference; Joint 5, 11% RMS relative difference; Joint 6, 22% RMS relative difference) [36] [16]

3.8. Rough ceramic and rough metal

Finally using Eq. 73 for the asperity slope of the bead blasted stainless steel and Eq. 75 for the asperity slope of the as-fired aluminum oxide the theoretical TCR for conforming rough stainless steel and conforming rough ceramic is compared with experimental data in Fig. 37a in vacuum and Fig. 37b in atmospheric pressure. In both cases the scale analysis model captures the trend of the data and is in reasonable agreement.

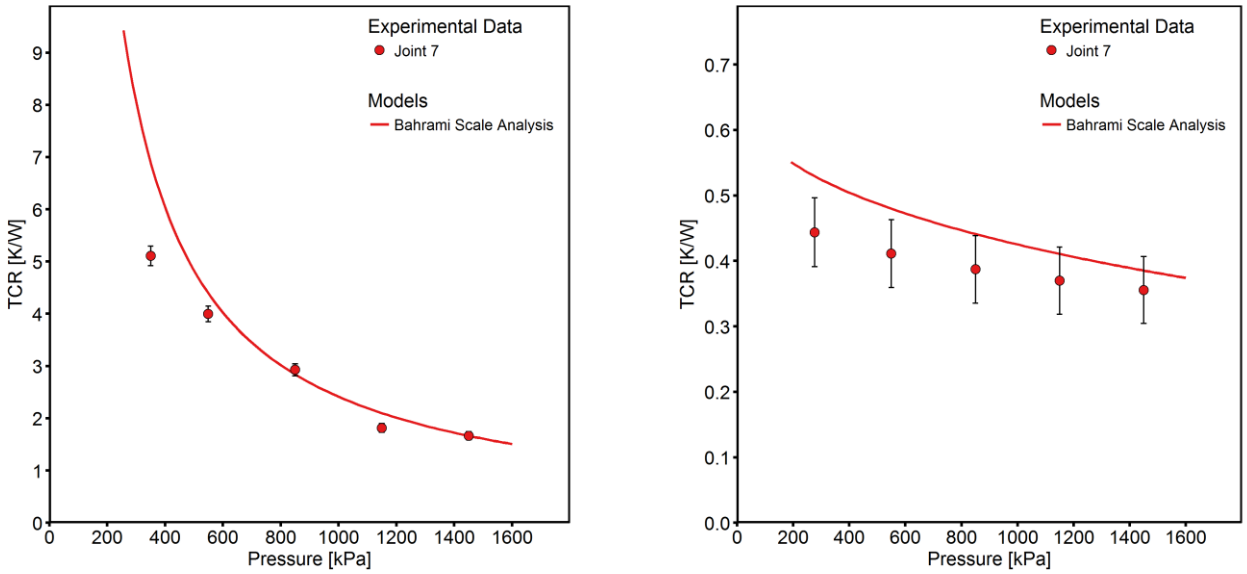

Fig. 37: a) Rough ceramic and rough stainless steel in vacuum (18% RMS relative difference) **b)** Rough ceramic and rough stainless steel in atmosphere (14% RMS relative difference) [36] [16]

3.9. Conclusion

Experimental TCR results between conforming rough stainless steel and aluminum oxide and aluminum nitride contacts were presented. The results adequately agreed with the available statistical metal-metal TCR models with use of certain asperity slope estimations. This strongly indicated that metal-metal TCR models were perfectly suitable for estimating ceramic-metal TCR despite the differences in material manufacture, surface features (porosity), microscale deformation characteristics and thermal conduction.

RMS relative difference between the plastic models and the data did not exceed 21% in vacuum or 24% in atmospheric pressure. The average RMS relative difference for the scale analysis model was 15% and 12% for the plastic CMY model. Most large deviations of the experimental data from the plastic models were observed at low contact pressures which was consistent with metal-metal contacts.

Chapter 4. Thermal contact resistance of alumina and aluminum

As seen in chapter 2, in power electronics aluminum oxide ceramics are used as insulators between high voltage devices and touch safe heat sinks because of their high dielectric strength and thermal conductivity. The thermal contact resistance developed at the interface of the insulator can be a significant impediment to heat transfer. In chapter 3 it was shown that the TCR between ceramics and metals can be modelled with existing TCR models. In this chapter, the thermal contact resistance between as-fired, lapped and polished aluminum oxide and cast, machined and anodized aluminum is measured using the guarded heat flow method. The influence of the thermal interface materials including graphite, phase change material and thermal grease is also measured. All results are compared with existing models.

4.1. Introduction

In chapter 2 it was seen that the TCR developed at the interface of alumina insulators and heat sinks was significant in bare contact. In chapter 3 the experimental TCR between ceramics and metals was compared with existing TCR models. However, in chapter 3, the only metal investigated was stainless steel because it does not corrode or oxidize. In power electronics, alumina insulators are frequently in contact with aluminum heat sinks. Aluminum heat sinks are typically either cast or extruded. Extruded aluminum has a higher thermal conductivity than cast aluminum but limits designers to extrudable geometries. Extruded aluminum may also be easily anodized. Casting allows for more complex cavities that can accommodate non-uniform shapes created by a fully assembled PCB. Cast aluminum is not typically anodized. In practice, TCR at alumina heat sink interfaces is reduced by application of a TIM. High performance thermal interface materials (TIMs), like thermal grease, reduce TCR by filling the micro gaps developed between rough surfaces that would otherwise be filled with lower thermal conductivity air [44]. TIMs have drawbacks which include increased cost, assembly complexity and reliability concerns due to thermal pump out. In addition to the use of TIMs, it is also common practice to machine cast surfaces and tape over extruded surfaces to be anodized to reduce cast surface imperfections and insulating coatings on mounting areas. Considering that anodized aluminum is aluminum oxide and that both cast aluminum and as-fired alumina insulators are rough and contain pores, are these mechanical operations necessary if a TIM is used? Alternatively, are TIMs required if surfaces are very smooth?

Very little data on alumina-metal TCR is available in the literature to answer these questions because most research studies have focused on metal-metal contacts [10]. Ceramics are different from the bead blasted metals used to validate bare TCR models (stainless steel, nickel, copper, etc.) in that their surfaces are not necessarily gaussian or close to gaussian, their surfaces are porous (to various degrees depending on grain size and sintering process), they are brittle and suffer from microscale fracture under indentation, and they transfer heat primarily via lattice vibrations (phonons) as opposed to electrons. Despite these differences, in Chapter 3, these models were validated for stainless steel (bead-blasted and lapped) and ceramic contacts. However, stainless steel is not a material that is used frequently in power electronics due to its poor thermal conductivity. Aluminum, on the other hand, is a very common material for heat sinks thanks to its low cost and high thermal conductivity. TCR with aluminums have not always agreed with TCR models because they develop thin aluminum oxide layers when exposed to air. Also, the surfaces of machined, cast and anodized aluminum extrusions are different from bead-blasted stainless steel. The roughness of milled and extruded surfaces are directionally dependent and not random.

The data for ceramic-metal joints with TIMs is also lacking in the literature; they are primarily limited to metal-TIM-metal joints. Exceptions include work by Chung et al. who studied the TCR between metallic coated alumina and aluminum. They showed that aluminum and copper coatings in contact with alumina had the lowest TCR [14]. Also, Lahmar et. al. measured the interfacial resistance between alumina and gold coatings and explored the influence of adhesion on the results [66]. Effective TIMs for metal-metal joints include thermal greases, gap fillers, graphite, phase change materials, metal foils and carbon nanotubes [48].

TCR models for TIMs are available in the literature such as the one by Bahrami et. al for polymer rough interfaces or Marotta et. al’s model for graphite contacts [42], [44]. Again, these models were not developed or validated for alumina-TIM-metal contacts and may not accurately predict TCR between engineered aluminums and alumina filled with TIMs.

This chapter aims to address the gap in the literature data on alumina-aluminum TCR by first reporting the experimental TCR between as-fired, lapped and polished alumina in bare contact with cast, anodized and machined aluminum measured with the guarded heat flow method as per ASTM E1530 [15] in order to provide an expected range of TCR between alumina and various aluminums.

The impact of TIMs on the TCR of alumina-aluminum joints is investigated using the same experimental setup. Commercially available TIMs tested include graphite thermal grease, gap filler material and phase change material.

4.2. Experimental setup and sample preparation

2 mm thick polished, lapped and as-fired 99.5 % aluminum oxide discs were ordered off the shelf from Ortech Advanced Ceramics. The thermal conductivity of the alumina samples were measured as described in Chapter 3 on the same experimental test bed.

Cast aluminum samples were machined out from aluminum heat sink castings. Half of the samples were then machined on CNC mill to produce cast aluminum samples with machined surfaces while the other half were untouched. The thermal conductivity of the cast aluminum was measured per the slab mode of the hot disk method or transient plane source method [67] (TPS2500S Thermal Constants Analyser, Hot Disk AB, Sweden and ThermTest Inc, Canada). Extruded aluminum 6063-T5 disk were machined and anodized with a type 2 cosmetic coating as is typical in the power electronics industry (Spectral Finishing, BC, Canada). Extruded aluminum thermal conductivity was not measured but taken from the literature because its expected thermal conductivity of 180 W/(m·K) is so high that even if it is 30% off, its impact on the resistance measurement is small (0.014 K/W). Metal samples are 3 mm thick.

To measure the TCR between alumina and aluminum surfaces the guarded heat flow meter setup was used with additional aluminum samples between the heat flux meters and the alumina sample. The heat flow through the joint was measured per ASTM E1530 using the cylindrical ARMCO iron heat flux meters as described in Chapter 3. To measure the temperature difference across the aluminum-alumina-aluminum joint, thermocouples (Omega, T Type, ±1 °C) were inserted into each aluminum sample. All sample roughness measurements were measured by profilometer (skidless diamond tip, Mitutoyo Surftest SJ-400) at our lab, the Laboratory for Alternative Energy Conversion. Results are tabulated in Table 11.

All measurements were conducted in atmospheric pressure at steady state conditions determined to be when the total thermal resistance between the heat flux meters changed less than 0.12% for at least 30 minutes and 0.06% for at least 10 minutes. On average, tests exceeded 3 hours. For tests conducted with grease and gap filler, 0.3 grams of thermal interface material was applied on each alumina-aluminum interface. This was measured with a high sensitivity scale. Approximate bond-line thickness prior to compression is listed in Table 12. Upon compression, significant thermal interface material escaped the joint.

Table 11: Properties of aluminum and alumina samples

Samples	Thermal conductivity, W/(m·K)	Roughness, μm
As-fired alumina	25.19	1.1
Lapped alumina	25.19	1
Polished alumina	25.19	0.3
Cast aluminum	120	1.2
Machined aluminum	120	1.55
Anodized aluminum	180	0.4

Table 12: Thermal interface material properties

TIMs	Thermal conductivity, W/(m·K)	Density, kg/m^3	Initial thickness, mm
Graphite	28 (through)	-	0.2
Grease	2.3	2530	0.23
Gap filler	3.6	3000	0.19
PCM	4	-	0.2

4.3. Experimental results: Bare Joints

Thermal contact resistance results of bare cast aluminums and alumina under atmospheric pressure are shown in Fig. 38. The results show that there is little difference between using polished, lapped or as-fired alumina when in bare contact with cast aluminum. Fig. 39 contain results for thermal contact resistance between the same aluminum oxide disks and machined aluminum anodized aluminum, respectfully. Since the machined aluminum is actually cast aluminum it too suffers from some porosity. In this case, the TCR of the machined aluminum is higher than the cast aluminum because the samples tested are actually rougher than the cast samples and have the same thermal conductivity. The anodized aluminum samples were originally extruded aluminum and have the lowest roughness of the three aluminum samples. However, the anodized layer (aluminum oxide) is harder than the cast surface and so likely contributes to higher TCR in bare contact. TCR between bulk alumina and anodized aluminum is shown in Fig. 40. Error bars account for the uncertainty of the measured data (see Appendix A for details).

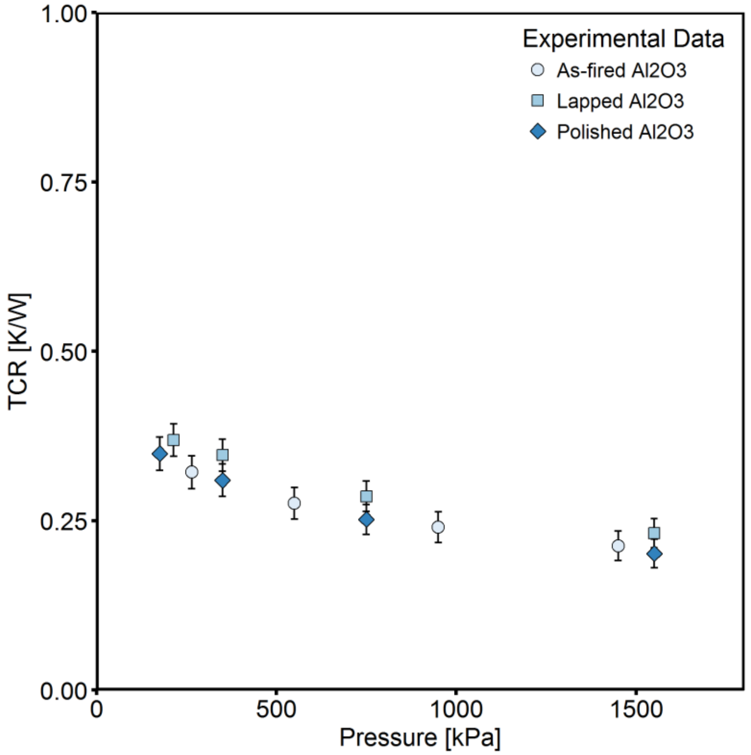

Fig. 38: TCR between cast aluminum and as-fired, lapped and polished alumina in atmospheric pressure

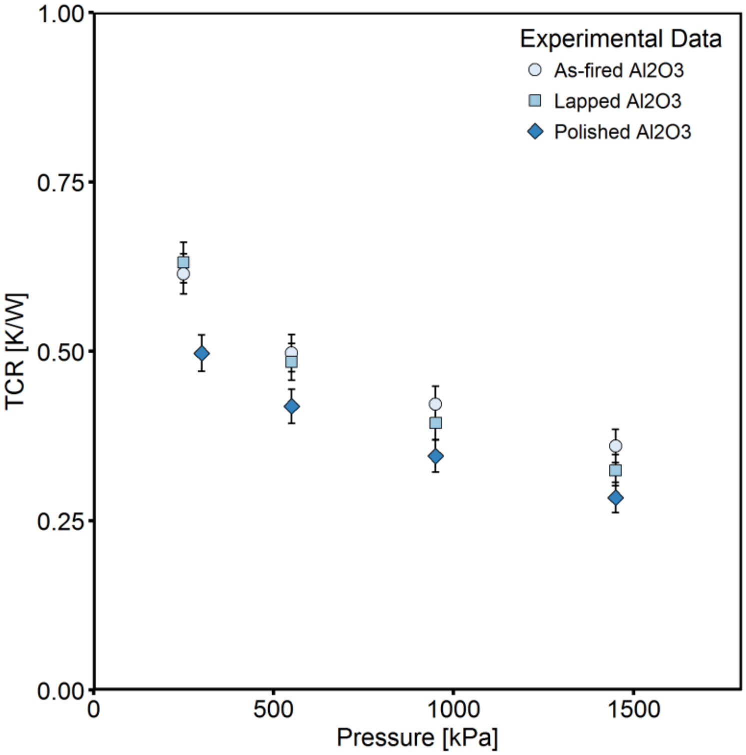

Fig. 39: TCR between machined (cast) aluminum and as-fired, lapped and polished alumina in atmospheric pressure

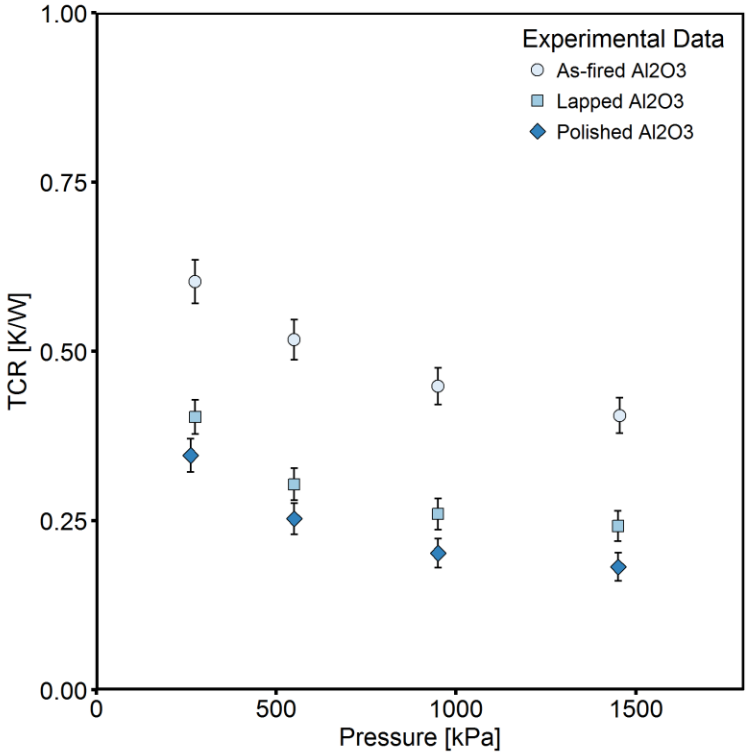

Fig. 40: TCR between anodized aluminum and as-fired, lapped and polished alumina in atmospheric pressure

4.4. Experimental results: TIM Filled Joints

Fig. 41 contains TCR results between cast aluminum and as-fired alumina with three different thermal interface materials. Use of graphite, grease, and gap filler all offer significant reductions in TCR when compared to the bare joints. Using the gap filler material results in the lowest TCR while the graphite has the highest TCR especially at low contact pressures.

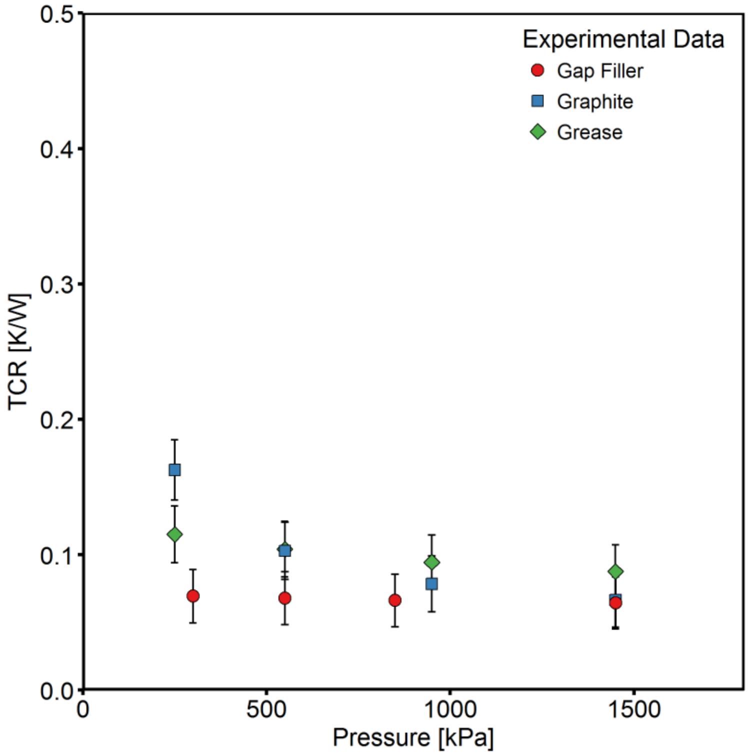

Fig. 41: TCR between cast aluminum and as-fired Al_2O_3 with TIMs.

Fig. 42 includes results for machined aluminum in contact with as-fired alumina with thermal grease, gap filler and graphite. Despite the big differences between the cast and machined aluminum in bare contact with alumina, when a TIM is used both joints have similar TCR. These results imply that with thermal interface materials between the joints, the TCR is a weaker function of the effective roughness parameters of the surfaces. Finally, Fig. 43 contains the results from anodized aluminum in contact with alumina with the previously mentioned TIMs. The reduction in TCR from the bare joints to the TIM joints is the lowest for the anodized surfaces. This is reasonable because the anodized layer introduces a significant resistance in the joint and this is not reduced with the use of TIMs.

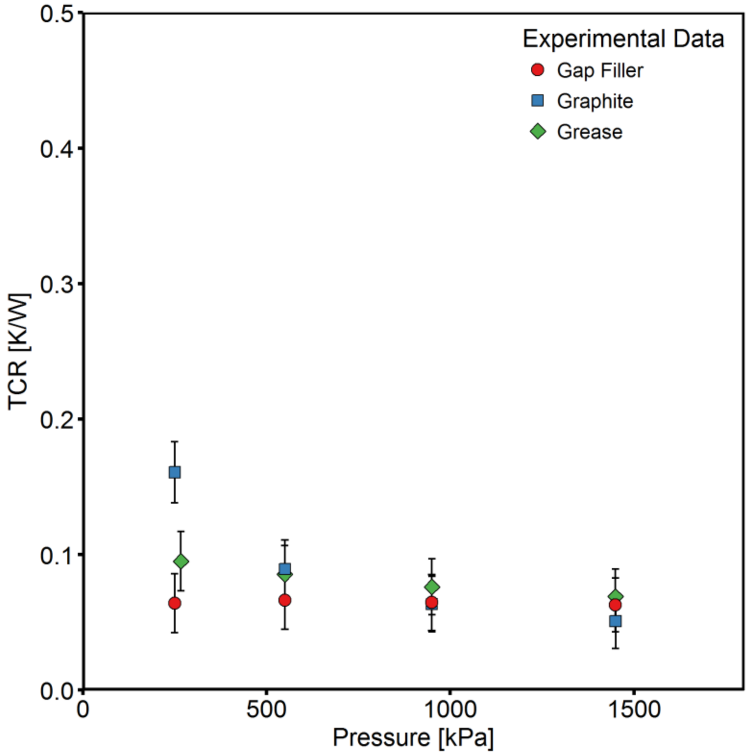

Fig. 42: TCR between machined (cast) aluminum and as-fired Al_2O_3 with TIMs.

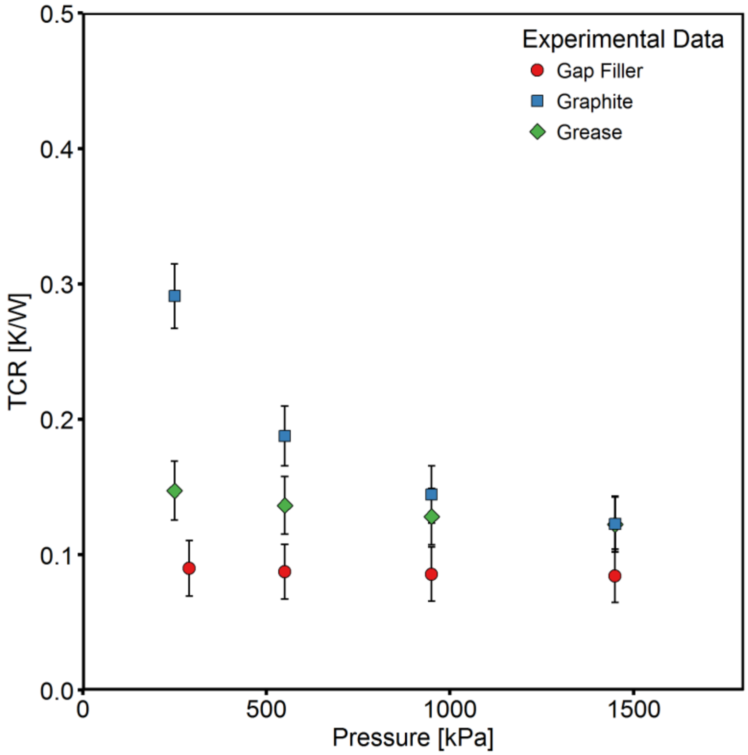

Fig. 43: TCR between anodized (extruded) aluminum and Al2O3 with TIMs.

4.5. Comparison with models: Bare joints

The same scale analysis model used in Chapter 3 is compared with the experimental data in Fig. 44, Fig. 45 and Fig. 46.

The model is in reasonable agreement with the experimental data of the TCR for cast aluminum in contact with alumina, shown in Fig. 44, however the difference between the model and the experiment is higher than the stainless steel and alumina TCR studied in chapter 3. This higher difference could be due to out-of-flatness of the cast aluminum surface or a thin aluminum oxide layer developed on the cast surface.

Rough milled surfaces are not uniformly random. Due to the cutting tool, they have a macro-scale lay which may be categorized as surface waviness. Consequently, the model is very poor for the machined aluminum (milled) surface in contact with alumina in

Fig. 45. In addition, out of flatness could contribute to the large difference between the model and the experiment. This highlights the limitations of the conforming rough TCR models.

For the anodized aluminum in contact with alumina, Fig. 46, the model does not change with pressure at the same rate as the experimental data which suggests that an error may be found in the contact mechanics modelling or the related material properties. For this case, the micro-surface hardness used is that of alumina (15 GPa) because anodized aluminum has approximately a 25 micron thick anodization layer of aluminum oxide on the surface. This is an approximate micro-hardness value for sintered aluminum oxide and likely differs significantly from the anodized aluminum coating. The model used here is not appropriate for contacts with coatings. This too highlights the limitations of conforming rough contact models for use with aluminum heat sinks surfaces found in industry.

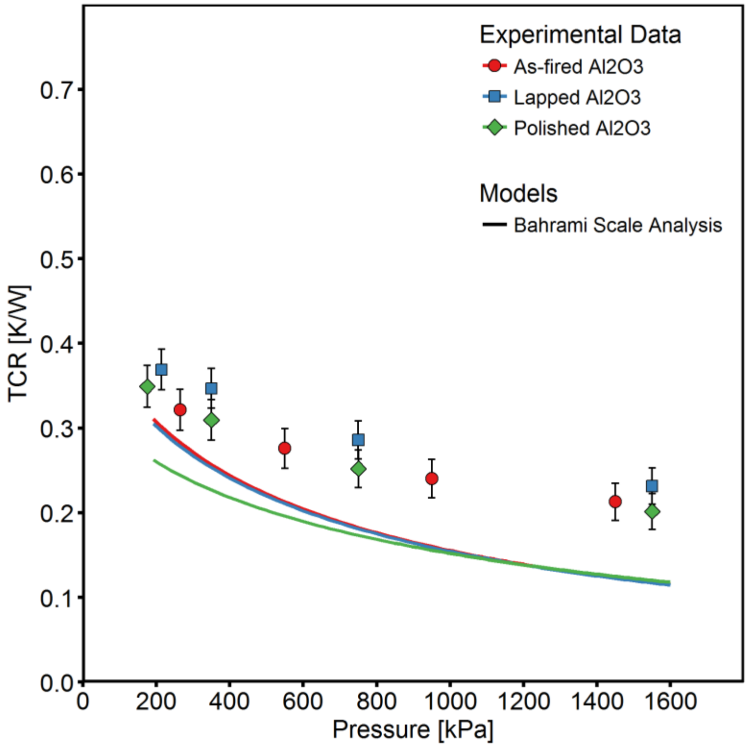

Fig. 44: Experimental TCR vs contact pressure between cast aluminum and alumina (polished, lapped and as-fired) and scale analysis model.

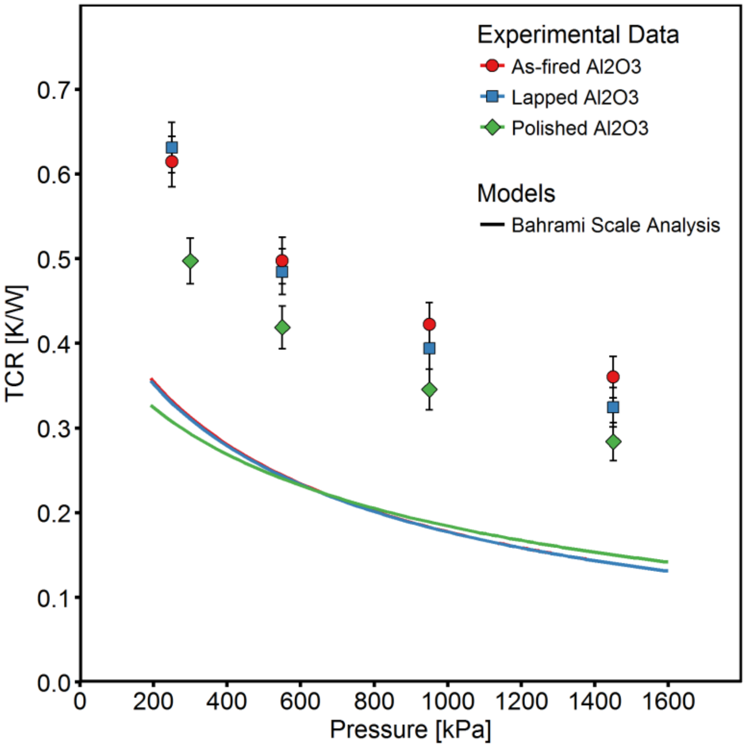

Fig. 45: TCR vs contact pressure between machined aluminum and alumina (polished, lapped and as-fired) and scale analysis model.

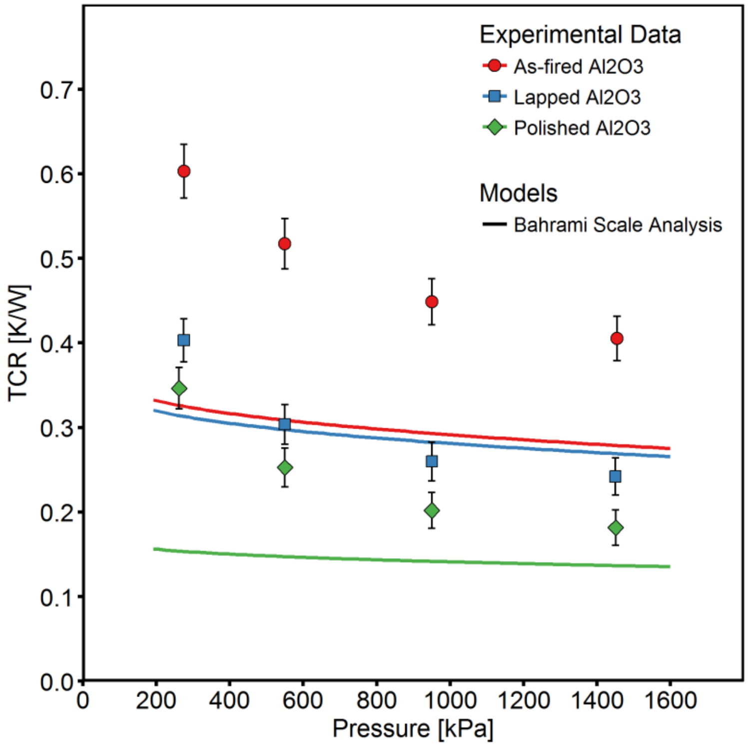

Fig. 46: Experimental TCR vs contact pressure between anodized aluminum and alumina (polished, lapped and as-fired) and scale analysis model.

4.6. Comparison with models: TIM filled joints

Figures 47, 48 and 49 show the comparison of the experimental data with models for the joints with interface materials. In all cases the TIM model is approximated with Eq. 76 where the only term in the equation represents thermal resistance due to the bond-line thickness of the TIM between the two solids. Given that the experimental data does not change with pressure the change in bond-line thickness with pressure is neglected. Contact resistance between the solids and the TIMs are also neglected in Eq. 76. Graphite is not modelled to due to lack of critical material properties.

$$TCR_{Al2O3} = \frac{t_{bond-line}}{k_{TIM} A} \tag{76}$$

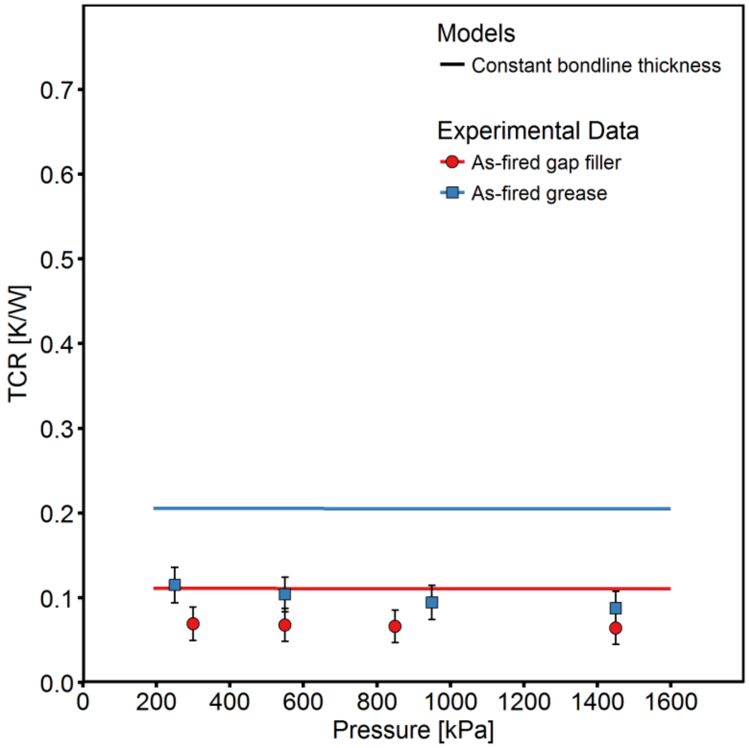

Fig. 47: Experimental TCR and conforming rough modelled TCR of cast aluminum and Al2O3 with thermal grease and gap filler vs contact pressure in atmospheric air.

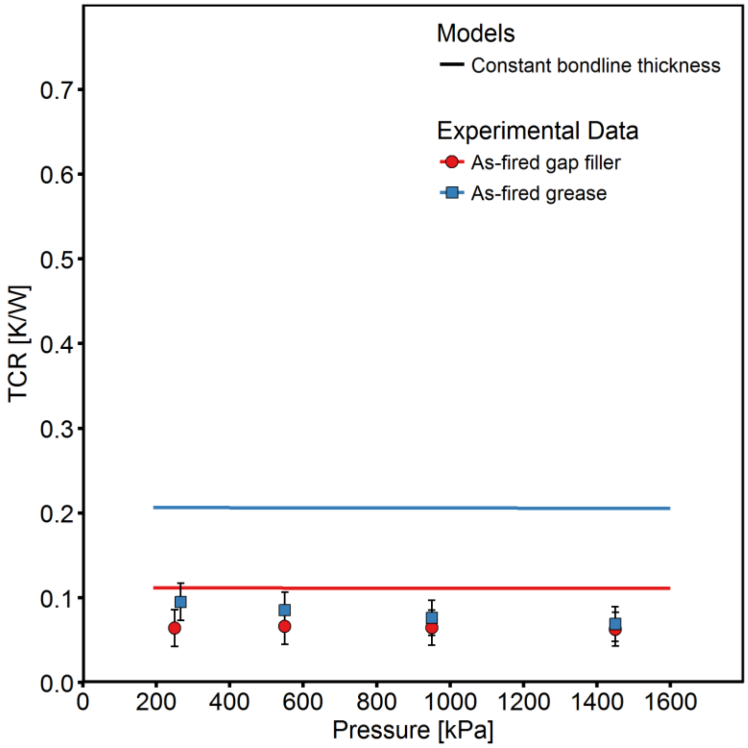

Fig. 48: Experimental TCR and conforming rough modelled TCR of machined (cast) aluminum and Al2O3 with thermal grease and gap filler vs contact pressure in atmospheric air.

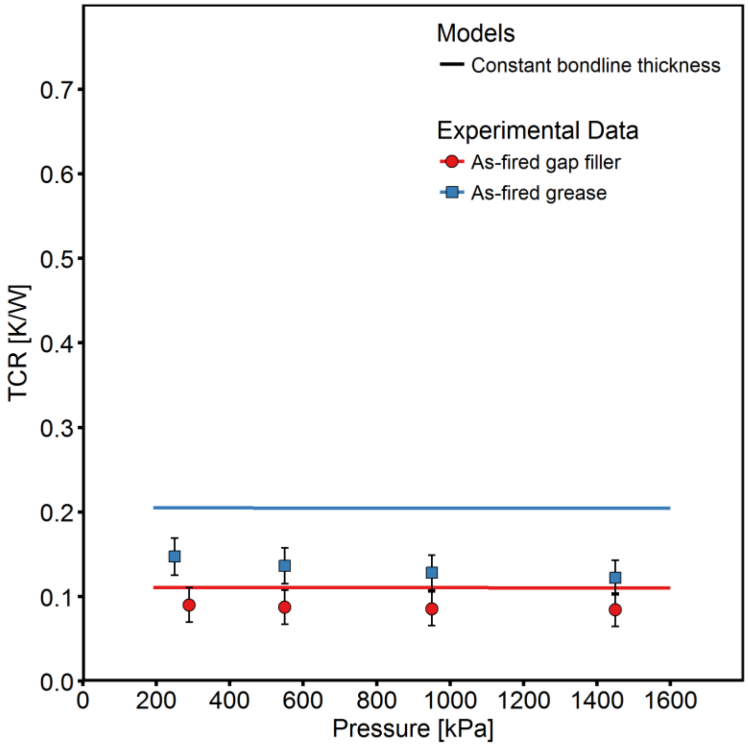

Fig. 49: Experimental TCR and conforming rough modelled TCR of anodized (extruded 6063) aluminum and Al2O3 with thermal grease and gap filler vs contact pressure in atmospheric air.

As seen in Fig. 47, 48 and 49 the effect of contact pressure is negligible on TCR in this experiment. The thickness of TIM in the joint is driving the TCR in all three cases. The large difference between the model and experimental data for the thermal grease is due to the inaccurate bond-line thickness approximation in the model. In reality, much of the grease is displaced out of the joint and the bond-line thickness should be properly measured in-situ. Also, the results with thermal grease show a small dependence on contact pressure. Though this is within the uncertainty of the data, it suggests either that the bond-line thickness is changing slightly with contact pressure or the resistance the TIM and the solid is changing with contact pressure. It is difficult to draw further conclusions from this experimental data because the bare-bare models did not match the experimental data.

For the gap filling material, which does not remain liquid but solidifies in the joint, the bond-line thickness approximation is much more appropriate though it still is not within the error bars for both the cast aluminum and machined aluminum cases. The model is within the correct order of magnitude of the experimental results and follows the same trend. For the anodized aluminum, it is within the error bars at low pressure.

4.7. Conclusion

TCR results between as-fired, lapped and polished alumina and cast, machined and anodized aluminum were presented with and without TIMs. The conforming rough contact model validated for use with ceramic-meatllic contact in chapter 3 did not capture the TCR of the anodized and machined aluminum in contact with alumina. The model was more appropriate for the cast aluminum and alumina joints. This was attributed to the waviness of the machined aluminum and the effect of the coating of the anodized aluminum on the contact mechanics.

With a TIM in the joint, the results correlated weakly with contact pressure and with surface roughness which suggests that controlled surface roughness may not be necessary for minimizing TCR cost-effectively when using a TIM. A simple TIM model captured the trends of the TIM filled joint data but was not accurate due to an approximate bond-line thickness measurement.

Chapter 5. Conclusion

5.1. Summary

In this thesis, the thermal resistance of alumina insulators for power electronics was explored in detail because they can provide excellent electrical insulation with minimal thermal resistance at a reasonable cost. It was revealed that the thermal contact resistance between the alumina insulator and metals was significant and non-negligible in Chapter 2. When using thermal interface materials, the thermal contact resistance was reduced up to 70%. The thermal contact resistance between aluminum oxide, aluminum nitride and stainless steels was then measured experimentally. These results were compared with existing statistical conforming rough contact models in order to validate their use for ceramic-metallic joints. The results were in reasonable agreement for conforming rough contact of ceramics with lapped and bead-blasted stainless steels.

However, it was then shown that the conforming rough models were not satisfactory for alumina in contact with typical heat sink aluminums (cast aluminum, machined cast aluminum and anodized extruded aluminum). Given that they were in agreement with stainless steel alumina contacts, it is believed that the cause of the non-agreement was due to the aluminum surfaces. Finally, the TCR of aluminum alumina joints with thermal interface materials was measured experimentally with the same method. In all cases except for graphite, thermal interface materials reduced the TCR's dependence on pressure. The results suggested that reducing roughness with further machining may not be necessary if an effective TIM is used and the original effective surface is in the conforming rough regime.

5.2. Suggested research topics

The experimental results in this thesis strongly suggest that conforming rough contact models are sufficient for ceramic-metallic joints if their surfaces are close to Gaussian and in the conforming rough regime. However, the models are not in agreement for aluminum alumina joints more typical of actual applications. Reasons for this are not obvious. It is possible that the aluminum surfaces in contact with alumina were not in the conforming rough regime. It is also possible that the oxide surfaces developed on aluminum (aluminum oxide) are to blame. The nature of the surface roughness of the cast, extruded and milled surfaces may also contribute to the failure of conforming rough models to capture the experimental TCR. The roughness of extruded and milled surfaces are clearly directionally dependent and not random (patterns are visible on the surfaces). This is less obvious for the cast surfaces.

Modelling non-Gaussian surfaces with another probability distribution that better fits each real surface (cast, milled and extruded, etc.) might solve this problem. This would likely require a numerical solver to calculate the separation between mean contact planes because non-Gaussian probability distributions are not convenient for mathematical analysis. A TCR model of this nature would be very useful for the TCR community because it would account for a large range of surfaces.

Section 3.4 includes SEM images used to approximate the porosity of the ceramic surfaces in this thesis. It is an approximate method and the porosity was not shown to be high (around 10%). This low porosity does not likely affect the TCR significantly. At higher porosity the surface roughness might not be close to Gaussian because there will be more valleys (pores) than hills. It is not clear if these conforming rough models are appropriate for very porous surfaces.

Ultimately, TIMs are used with alumina insulators in power electronics. Improving TIM models may therefore be an avenue worth pursuing. TIM models may be either too simple, like the one in chapter 4, or complex and involve too many unknown material dependent inputs. Many of these variables are not tabulated for ceramics.

The models investigated in chapter 3 and 4 all assume uniform contact pressures, however as seen in chapter 2 non-uniform contact pressures are common in the industry. Work may therefore be found on predicting the non-uniform contact pressures developed in power electronics and using this pressure distribution to calculate expected TCR with a given TIM.

References

[1] D. Tan, “Emerging System Applications and Technological Trends in Power Electronics: Power electronics is increasingly cutting across traditional boundaries,” *IEEE Power Electronics Magazine*, vol. 2, no. June, pp. 38–47, 2015.

[2] Grand View Research, “Power Electronics Market Size Worth $39.22 Billion By 2025,” 2017.

[3] International Energy Agency IEA, “Technology Roadmap: Electric and plug-in hybrid electric vehicles,” 2011.

[4] International Energy Agency IEA, “Technology Roadmap Wind energy,” 2013.

[5] International Energy Agency IEA, “Technology Roadmap Solar Photovoltaic Energy,” 2014.

[6] R. K. Dey and A. Sardar, “Trends in Power Electronics Packaging Technologies For XEVs,” *Auto Tech Review*, vol. 3, no. 8, pp. 18–23, Aug. 2014.

[7] BCCResearch, “The Market for Thermal Management Technologies,” Wellesley, MA, USA, 2016.

[8] Y. A. Cengel, *Heat Transfer A Practical Approach*, 2nd ed. New York: McGraw-Hill, 2004.

[9] X. C. Tong, *Advanced Materials for Thermal Management of Electronic Packaging*. Springer-Verlag New York, 2014.

[10] M. M. Yovanovich, “Four decades of research on thermal contact, gap, and joint resistance in microelectronics,” *IEEE Transactions on Components and Packaging Technologies*, vol. 28, no. 2. pp. 182–206, 2005.

[11] V. V. Rao, M. V. Krishna Murthy, and J. Nagaraju, “Thermal conductivity and

thermal contact conductance studies on Al2O3/Al-AlN metal matrix composite," *Composites Science and Technology*, vol. 64, no. 16, pp. 2459–2462, 2004.

[12] T. Aikawa and W. O. Winer, "Thermal contact conductance across Si3N4—Si3N4 contact," *Wear*, vol. 177, pp. 25–32, 1994.

[13] E. Marotta and L. S. Fletcher, "Thermal contact conductance of refractory ceramic coatings," *Journal of Thermophysics and Heat Transfer*, vol. 10, no. 1, pp. 10–18, 1996.

[14] K. C. Chung, H. K. Benson, and J. W. Sheffield, "Thermal contact conductance of ceramic substrate junctions," *Journal of Heat Transfer*, vol. 117, no. 2, pp. 508–510, 1995.

[15] ASTM International, "ASTM E1530-11(2016), Standard Test Method for Evaluating the Resistance to Thermal Transmission of Materials by the Guarded Heat Flow Meter Technique," West Conshohocken, PA, 2016.

[16] M. Bahrami, J. Culham, and M. Yovanovich, "Thermal resistances of gaseous gap for conforming rough contacts," *AIAA Paper(42nd AIAA Aerospaces Meeting and Exhibit)*, pp. 1–11, 2004.

[17] M. Bahrami, J. R. Culham, M. M. Yovanovich, and G. E. Schneider, "Thermal Contact Resistance of Nonconforming Rough Surfaces, Part 1: Contact Mechanics Model," *Journal of Thermophysics and Heat Transfer*, vol. 18, no. 2, pp. 209–217, 2004.

[18] M. Bahrami, J. R. Culham, M. M. Yovanovich, and G. E. Schneider, "Thermal Contact Resistance of Nonconforming Rough Surfaces, Part 2: Thermal Model," *Journal of Thermophysics and Heat Transfer*, vol. 18, no. 2, pp. 218–227, 2004.

[19] M. Garcia-Poulin, M. Ahmadi, M. Bahrami, E. Lau, and C. Botting, "Thermal Resistance of Electrical Insulation for Bolted and Clamped Discrete Power Devices," in *2018 34th Thermal Measurement, Modeling & Management Symposium (SEMI-THERM)*, 2018.

[20] M. R. (Ed.), *Power Electronics Handbook*, 3rd ed. Elsevier Science, 2010.

[21] B. Electronics, “Bitron Electronics Power converters and commands for automotive applications.” [Online]. Available: https://www.bitronelectronics.com/pages/PowerElectronics_automotive_en/185.

[22] Delta, “Delta Solar Inverters.”

[23] Elmo Motion Control, “Elmo Motion Control Wind Turbine Featured Product - Tiger & Eagle Powerful Digital Servo Drives.” [Online]. Available: http://www.elmomc.com/applications/wind-turbine-stations-application.htm.

[24] A. Technologies, “48Vdc Cordex HP 1.2kW.”

[25] PCPartPicker, “Corsair - 1200W 80+ Platinum Certified Fully-Modular ATX Power Supply.” [Online]. Available: https://ca.pcpartpicker.com/product/vkYXsY/corsair-power-supply-ax1200i.

[26] D.-Q. Technologies, “RC1200 Battery Charger.” [Online]. Available: https://delta-q.com/product/rc1200-battery-charger/.

[27] J. D. Cressler, *Silicon Earth : introduction to the microelectronics and nanotechnology / John D. Cressler.*, 2nd ed. Boca Raton, Florida , 2016.

[28] J. P. Joule, “XXXVIII. On the heat evolved by metallic conductors of electricity, and in the cells of a battery during electrolysis,” *The London, Edinburgh, and Dublin Philosophical Magazine and Journal of Science*, vol. 19, no. 124, pp. 260–277, Oct. 1841.

[29] Y. Shabany, *Heat transfer : thermal management of electronics / Younes Shabany.* Boca Raton : CRC Press, 2010.

[30] Y. A. Cengel, *Introduction to Thermodynamics and Heat Transfer*, Second. New York: McGraw-Hill, 2008.

[31] J. a. Greenwood and J. B. P. Williamson, “Contact of Nominally Flat Surfaces,”

Proceedings of the Royal Society A: Mathematical, Physical and Engineering Sciences, vol. 295, no. 1442, pp. 300–319, 1966.

[32] R. Jahn and H. Truckenbrodt, “A simple fractal analysis method of the surface roughness,” *Journal of Materials Processing Technology*, 2004.

[33] Z. J. Wang, W. Z. Wang, Y. Z. Hu, and H. Wang, “A numerical elastic-plastic contact model for rough surfaces,” *Tribology Transactions*, 2010.

[34] G. Liu, J. Zhu, L. Yu, and Q. J. Wang, “Elasto-plastic contact of rough surfaces,” *Tribology Transactions*, 2001.

[35] M. Bahrami, M. M. Yovanovich, and J. R. Culham, “Thermal Joint Resistances of Conforming Rough Surfaces with Gas-Filled Gaps,” *Journal of Thermophysics and Heat Transfer*, vol. 18, no. 3, pp. 326–332, 2004.

[36] M. Bahrami, J. R. Culham, and M. M. Yovanovich, “Modeling Thermal Contact Resistance: A Scale Analysis Approach,” *Journal of Heat Transfer*, vol. 126, no. 6, p. 896, 2004.

[37] M. R. Sridhar and M. M. Yovanovich, “Review of Elastic and Plastic Contact Conductance Models: Comparison with Experiment,” *Journal of Thermophysics and Heat Transfer*, 1994.

[38] A. A.-H. Hegazy, “Thermal Joint Conductance of Conforming Rough Surfaces: Effect of Surface Micro-Hardness Variation,” University of Waterloo, 1985.

[39] M. R. Sridhar and M. M. Yovanovich, “Empirical methods to predict Vickers microhardness,” *Wear*, 1996.

[40] M. M. Yovanovich, “Micro and Macro Hardness Measurements , Correlations , and Contact Models,” in *44th AIAA Aerospace Sciences Meeting and Exhibit*, 2006, pp. 1–28.

[41] S. Song, M. M. Yovanovich, and F. O. Goodman, “Thermal Gap Conductance of Conforming Surfaces in Contact,” *Journal of Heat Transfer*, 1993.

[42] E. E. Marotta, S. J. Mazzuca, and J. Norley, “Thermal joint conductance for flexible graphite materials: Analytical and experimental study,” *IEEE Transactions on Components and Packaging Technologies*, vol. 28, no. 1, pp. 102–110, 2005.

[43] C. Yuan, B. Duan, L. Li, B. Shang, and X. Luo, “An improved model for predicting thermal contact resistance at liquid-solid interface,” *International Journal of Heat and Mass Transfer*, 2015.

[44] M. Bahrami, M. M. Yovanovich, and E. E. Marotta, “Thermal joint resistance of polymer-metal rough interfaces,” *J. Electron. Packag.*, vol. 128, no. 1, pp. 23–29, 2006.

[45] Y. Xiong *et al.*, “Prognostic and Warning System for Power-Electronic Modules in Electric , Hybrid Electric , and Fuel-Cell Vehicles,” *IEEE Transacations of Industrial Electronics*, vol. 55, no. 6, pp. 2268–2276, 2008.

[46] T.-L. Li and S. L.-C. Hsu, “Enhanced thermal conductivity of polyimide films via a hybrid of micro-and nano-sized boron nitride,” *The Journal of Physical Chemistry B*, vol. 114, no. 20, pp. 6825–6829, 2010.

[47] R. C. Buchanan, “Ceramic Insulators,” in *Ceramic Materials for Electronics*, Third, Rev., R. C. Buchanan, Ed. New York: Marcel Dekker, 2004, pp. 1–85.

[48] J. Hansson, C. Zanden, L. Ye, and J. Liu, “Review of current progress of thermal interface materials for electronics thermal management applications,” *Nanotechnology (IEEE-NANO), 2016 IEEE 16th International Conference on*. pp. 371–374, 2016.

[49] K. C. Otiaba, N. N. Ekere, R. S. Bhatti, S. Mallik, M. O. Alam, and E. H. Amalu, “Thermal interface materials for automotive electronic control unit: Trends, technology and R&D challenges,” *Microelectronics Reliability*, vol. 51, no. 12. pp. 2031–2043, 2011.

[50] D. Gautam, D. Wager, and M. Edington, “Performance Comparison of Thermal Interface Materials for Power Electronics Applications,” pp. 3507–3511, 2014.

[51] A. Gholami and M. Bahrami, “Thermal Spreading Resistance Inside Anisotropic Plates with Arbitrarily Located Hotspots,” *Journal of Thermophysics and Heat Transfer*, vol. 28, no. 4, pp. 679–686, 2014.

[52] M. Razavi, Y. S. Muzychka, and S. Kocabiyik, “Review of Advances in Thermal Spreading Resistance Problems,” *Journal of Thermophysics and Heat Transfer*, vol. 30, no. 4, pp. 863–879, 2016.

[53] A. Bejan and A. D. Kraus, *Heat Transfer Handbook*. 2003.

[54] M. G. Cooper, B. B. Mikic, and M. M. Yovanovich, “Thermal contact conductance,” *International Journal of Heat and Mass Transfer*, 1969.

[55] C. V. Madhusudana, *Thermal Contact Conductance*, 2nd ed. Sydney: Springer, 2014.

[56] V. W. Antonetti and M. M. Yovanovich, “Enhancement of Thermal Contact Conductance By Metallic Coatings: Theory and Experiment.,” *Journal of Heat Transfer*. 1985.

[57] F. YIP, “The effect of oxide films on thermal contact resistance,” in *Thermophysics and Heat Transfer Conference*, American Institute of Aeronautics and Astronautics, 1974.

[58] S. R. Mirmira, L. S. Fletcher, and K. W. Baker, “Interfacial Contact Resistance of Single-Crystal Ceramics for Solar Concentrators,” *Journal of Thermophysics and Heat Transfer*, vol. 13, no. 1, pp. 110–116, 1999.

[59] B. B. Mikic, “Thermal contact conductance; theoretical considerations,” *International Journal of Heat and Mass Transfer*, 1974.

[60] M. R. Sridhar and M. M. Yovanovich, “Elastoplastic contact conductance model for isotropic conforming rough surfaces and comparison with experiments,” *J. Heat Transfer*, 1996.

[61] M. Li, Y. Wang, J. Zhou, J. Ren, and B. Li, “Thermal boundary conductance

across metal-nonmetal interfaces: effects of electron-phonon coupling both in metal and at interface," *European Physical Journal B*, vol. 88, no. 6, pp. 1–7, 2015.

[62] A. Majumdar and P. Reddy, "Role of electron-phonon coupling in thermal conductance of metal-nonmetal interfaces," *Applied Physics Letters*, 2004.

[63] E. T. Swartz and R. O. Pohl, "Thermal boundary resistance," *Reviews of Modern Physics*, 1989.

[64] B. R. Lawn, "Indentation of Ceramics with Spheres : A Century after Hertz," vol. 94, pp. 1977–1995, 1998.

[65] P. Auerkari, "Mechanical and physical properties of engineering alumina ceramics," Espoo, Finland, 1996.

[66] A. Lahmar, T. P. Nguyen, D. Sakami, S. Orain, Y. Scudeller, and F. Danes, "Experimental investigation on the thermal contact resistance between gold coating and ceramic substrates," *Thin Solid Films*, vol. 389, no. 1–2, pp. 167–172, 2001.

[67] M. Gustavsson, E. Karawacki, and S. E. Gustafsson, "Thermal conductivity, thermal diffusivity, and specific heat of thin samples from transient measurements with hot disk sensors," *Review of Scientific Instruments*, 1994.

Appendix A: Uncertainty calculations

The experimental data was analyzed in the R programming language. All linear curve fits were performed with R. The following equations were used in the uncertainty analysis.

$$uRel_{Q_{1\,or\,2}} = \sqrt{\frac{uAbs_{k_{HFM}}^{2}}{k_{HFM}^{2}} + \frac{uAbs_{A}^{2}}{A^{2}} + \frac{uAbs_{\frac{dT}{dx}}^{2}}{\frac{dT^{2}}{dx}}}$$

$$uRel_{Q_{avg}} = \sqrt{uAbs_{Q_{1}}^{2} + uAbs_{Q_{2}}^{2}}$$

$$uRel_{\frac{Qt}{kA}}^{2} = \sqrt{\frac{uAbs_{A}^{2}}{A^{2}} + \frac{uAbs_{t}^{2}}{t^{2}} + \frac{uAbs_{k}^{2}}{k^{2}} + uRel_{Q_{avg}}^{2}}$$

$$uAbs_{T_{int_{1\,or\,2}}} = \sqrt{uAbs_{\frac{Qt}{kA}}^{2} + uAbs_{TC}^{2}}$$

$$uAbs_{dT} = \sqrt{uAbs_{T_{int_{1}}}^{2} + uAbs_{T_{int_{1}}}^{2}}$$

$$uRel_{R_{j}} = \sqrt{uRel_{dT}^{2} + uRel_{Q_{avg}}^{2}}$$

$$uRel_{R_{met\,or\,cer}} = \sqrt{\frac{uAbs_{A}^{2}}{A^{2}} + \frac{uAbs_{t}^{2}}{t^{2}} + \frac{uAbs_{k}^{2}}{k^{2}}}$$

$$uAbs_{2TCR} = \sqrt{uAbs_{R_{j}}^{2} + uAbs_{R_{cer}}^{2} + uAbs_{R_{met}}}$$

$$uRel_{TCR} = \frac{uAbs_{TCR}}{2TCR}$$

Appendix B: Tabulated results from Chapter 3

Table 13: Joint 1 surface properties

Scale analysis micro-hardness [Pa]	CMY micro-hardness [Pa]	Effective elasticity [Pa]	Effective thermal conductivity [W/(m·K)]	Effective RMS roughness [m]	Effective average asperity slope [rad]
2.88E+09	2.91E+09	1.09E+11	16.76	2.84E-06	0.14

Table 14: Joint 1 vacuum results

Pressure [kPa]	Exp. TCR [K/W]	Abs. uncertainty [K/W]	TCR scale analysis [K/W]	TCR CMY plastic [K/W]	TCR CMY elastic [K/W]	Rel. dif. scale analysis	Rel. dif. CMY plastic	Rel. dif. CMY elastic
350.17	8.96	0.35	11.32	10.17	17.94	26.33%	13.56%	100.14%
550.05	6.84	0.25	7.20	6.63	11.68	5.32%	3.00%	70.84%
850.33	4.09	0.16	4.64	4.38	7.71	13.51%	7.07%	88.48%
1150.11	3.47	0.14	3.44	3.30	5.81	0.88%	4.90%	67.34%
1449.83	2.86	0.12	2.73	2.66	4.67	4.62%	7.29%	63.10%

Table 15: Joint 1 atmospheric results

Pressure [kPa]	Exp. TCR [K/W]	Abs. uncertainty [K/W]	TCR scale analysis [K/W]	TCR CMY plastic [K/W]	TCR CMY elastic [K/W]	Rel. dif. scale analysis	Rel. dif. CMY plastic	Rel. dif. CMY elastic
274.80	0.54	0.07	0.67	0.60	0.65	24.37%	15.79%	23.47%
550.04	0.51	0.07	0.61	0.56	0.61	20.29%	10.98%	21.01%
850.07	0.49	0.07	0.57	0.52	0.58	16.73%	7.11%	19.00%
1149.74	0.47	0.07	0.54	0.49	0.55	13.40%	3.77%	17.11%
1450.06	0.46	0.07	0.51	0.46	0.53	9.97%	0.51%	14.99%

Table 16: Joint 2 surface properties

Scale analysis micro-hardness [Pa]	CMY micro-hardness [Pa]	Effective elasticity [Pa]	Effective thermal conductivity [W/(m·K)]	Effective RMS roughness [m]	Effective average asperity slope [rad]
3.09E+09	3.10E+09	1.29E+11	20.14	1.95E-06	0.12

Table 17: Joint 2 vacuum results

Pressure [kPa]	Exp. TCR [K/W]	Abs. uncertainty [K/W]	TCR scale analysis [K/W]	TCR CMY plastic [K/W]	TCR CMY elastic [K/W]	Rel. dif. scale analysis	Rel. dif. CMY plastic	Rel. dif. CMY elastic
349.88	6.61	0.28	8.12	7.24	12.11	22.84%	9.48%	83.09%
549.91	4.71	0.19	5.17	4.72	7.89	9.69%	0.16%	67.40%
850.00	3.28	0.13	3.34	3.13	5.22	2.12%	4.50%	59.54%
1149.93	2.80	0.12	2.47	2.35	3.93	11.85%	16.16%	40.00%
1450.07	2.31	0.10	1.96	1.89	3.15	15.12%	18.21%	36.55%

Table 18: Joint 2 atmospheric results

Pressure [kPa]	Exp. TCR [K/W]	Abs. uncertainty [K/W]	TCR scale analysis [K/W]	TCR CMY plastic [K/W]	TCR CMY elastic [K/W]	Rel. dif. scale analysis	Rel. dif. CMY plastic	Rel. dif. CMY elastic
288.31	0.49	0.05	0.47	0.43	0.46	4.62%	11.11%	5.83%
550.04	0.46	0.05	0.43	0.39	0.43	5.57%	12.62%	5.68%
849.97	0.43	0.05	0.40	0.37	0.41	7.05%	14.36%	5.98%
1149.94	0.42	0.05	0.38	0.35	0.39	9.05%	16.38%	6.88%
1449.95	0.41	0.05	0.36	0.33	0.37	11.30%	18.51%	8.10%

Table 19: Joint 3 surface properties

Scale analysis micro-hardness [Pa]	CMY micro-hardness [Pa]	Effective elasticity [Pa]	Effective thermal conductivity [W/(m·K)]	Effective RMS roughness [m]	Effective average asperity slope [rad]
3.01E+09	3.04E+09	1.3E+11	30.48	1.93E-06	0.11

Table 20: Joint 3 vacuum results

Pressure [kPa]	Exp. TCR [K/W]	Abs. uncertainty [K/W]	TCR scale analysis [K/W]	TCR CMY plastic [K/W]	TCR CMY elastic [K/W]	Rel. dif. scale analysis	Rel. dif. CMY plastic	Rel. dif. CMY elastic
349.95	4.28	0.15	5.66	5.07	8.00	32.25%	18.56%	86.81%
550.01	3.35	0.12	3.60	3.31	5.21	7.48%	1.29%	55.47%
550.04	3.35	0.12	3.60	3.31	5.21	7.53%	1.24%	55.54%
1149.89	2.05	0.08	1.73	1.66	2.61	15.52%	19.17%	27.20%
1450.07	1.73	0.08	1.37	1.33	2.09	20.62%	23.06%	21.07%

Table 21: Joint 3 atmospheric results

Pressure [kPa]	Exp. TCR [K/W]	Abs. uncertainty [K/W]	TCR scale analysis [K/W]	TCR CMY plastic [K/W]	TCR CMY elastic [K/W]	Rel. dif. scale analysis	Rel. dif. CMY plastic	Rel. dif. CMY elastic
260.50	0.47	0.05	0.46	0.42	0.45	2.54%	9.15%	3.91%
550.00	0.43	0.05	0.41	0.38	0.41	3.74%	10.92%	3.52%
849.92	0.41	0.05	0.38	0.35	0.38	6.09%	13.35%	4.37%
1149.94	0.39	0.05	0.35	0.32	0.36	9.26%	16.33%	6.19%
1449.88	0.38	0.05	0.33	0.31	0.35	12.39%	19.17%	8.12%

Table 22: Joint 4 surface properties

Scale analysis micro-hardness [Pa]	CMY micro-hardness [Pa]	Effective elasticity [Pa]	Effective thermal conductivity [W/(m·K)]	Effective RMS roughness [m]	Effective average asperity slope [rad]
4.10E+09	3.99E+09	1.29E+11	20.12	4.37E-07	0.06

Table 23: Joint 4 vacuum results

Pressure [kPa]	Exp. TCR [K/W]	Abs. uncertainty [K/W]	TCR scale analysis [K/W]	TCR CMY plastic [K/W]	TCR CMY elastic [K/W]	Rel. dif. scale analysis	Rel. dif. CMY plastic	Rel. dif. CMY elastic
349.98	4.80	0.22	4.40	3.74	2.80	8.47%	22.21%	41.75%
549.96	3.05	0.15	2.80	2.44	1.83	8.37%	20.25%	40.25%
849.89	1.42	0.09	1.81	1.61	1.21	27.81%	13.90%	14.61%
1149.77	1.09	0.08	1.34	1.21	0.91	23.23%	11.67%	16.26%
1450.00	0.85	0.07	1.06	0.97	0.73	24.27%	14.09%	14.44%

Table 24: Joint 4 atmospheric results

Pressure [kPa]	Exp. TCR [K/W]	Abs. uncertainty [K/W]	TCR scale analysis [K/W]	TCR CMY plastic [K/W]	TCR CMY elastic [K/W]	Rel. dif. scale analysis	Rel. dif. CMY plastic	Rel. dif. CMY elastic
275.08	0.12	0.06	0.13	0.12	0.12	12.26%	5.15%	2.59%
550.09	0.10	0.06	0.12	0.12	0.11	20.88%	13.09%	9.46%
849.99	0.09	0.06	0.12	0.11	0.11	25.11%	17.00%	12.42%
1150.09	0.09	0.06	0.11	0.11	0.10	27.75%	19.49%	14.08%
1449.93	0.09	0.06	0.11	0.10	0.10	28.06%	19.83%	13.74%

Table 25: Joint 5 surface properties

Scale analysis micro-hardness [Pa]	CMY micro-hardness [Pa]	Effective elasticity [Pa]	Effective thermal conductivity [W/(m·K)]	Effective RMS roughness [m]	Effective average asperity slope [rad]
3.95E+09	3.85E+09	1.30E+11	30.68	3.36E-07	0.04

Table 26: Joint 5 vacuum results

Pressure [kPa]	Exp. TCR [K/W]	Abs. uncertainty [K/W]	TCR scale analysis [K/W]	TCR CMY plastic [K/W]	TCR CMY elastic [K/W]	Rel. dif. scale analysis	Rel. dif. CMY plastic	Rel. dif. CMY elastic
349.91	3.52	0.15	3.14	2.68	1.45	10.97%	23.97%	58.80%
550.08	2.34	0.11	2.00	1.75	0.95	14.45%	25.16%	59.41%
849.63	1.26	0.08	1.28	1.15	0.62	2.03%	8.63%	50.39%
1149.98	0.89	0.07	0.95	0.87	0.47	6.49%	3.02%	47.32%
1449.99	0.68	0.07	0.76	0.70	0.38	10.77%	2.19%	44.47%

Table 27: Joint 5 atmospheric results

Pressure [kPa]	Exp. TCR [K/W]	Abs. uncertainty [K/W]	TCR scale analysis [K/W]	TCR CMY plastic [K/W]	TCR CMY elastic [K/W]	Rel. dif. scale analysis	Rel. dif. CMY plastic	Rel. dif. CMY elastic
275.03	0.10	0.06	0.11	0.10	0.09	6.00%	0.35%	5.16%
550.09	0.09	0.06	0.10	0.09	0.09	10.72%	4.71%	3.08%
849.88	0.08	0.06	0.09	0.09	0.08	12.35%	6.23%	3.53%
1150.05	0.08	0.06	0.09	0.09	0.08	12.65%	6.55%	4.85%
1449.92	0.08	0.06	0.09	0.08	0.07	12.43%	6.42%	6.39%

Table 28: Joint 6 surface properties

Scale analysis micro-hardness [Pa]	CMY micro-hardness [Pa]	Effective elasticity [Pa]	Effective thermal conductivity [W/(m·K)]	Effective RMS roughness [m]	Effective average asperity slope [rad]
3.87E+09	3.80E+09	1.29E+11	20.13	1.12E-06	0.14

Table 29: Joint 6 vacuum results

Pressure [kPa]	Exp. TCR [K/W]	Abs. uncertainty [K/W]	TCR scale analysis [K/W]	TCR CMY plastic [K/W]	TCR CMY elastic [K/W]	Rel. dif. scale analysis	Rel. dif. CMY plastic	Rel. dif. CMY elastic
350.08	3.97	0.16	5.00	4.30	6.90	25.85%	8.33%	73.79%
550.15	2.75	0.12	3.18	2.80	4.50	15.73%	2.03%	63.62%
850.04	2.16	0.10	2.06	1.86	2.98	4.61%	13.89%	38.01%
1150.04	1.65	0.09	1.52	1.40	2.24	7.94%	15.49%	35.40%
1450.05	1.45	0.08	1.21	1.12	1.80	16.53%	22.37%	24.34%

Table 30: Joint 6 atmospheric results

Pressure [kPa]	Exp. TCR [K/W]	Abs. uncertainty [K/W]	TCR scale analysis [K/W]	TCR CMY plastic [K/W]	TCR CMY elastic [K/W]	Rel. dif. scale analysis	Rel. dif. CMY plastic	Rel. dif. CMY elastic
247.00	0.23	0.06	0.29	0.27	0.28	24.48%	16.16%	21.75%
549.90	0.21	0.06	0.26	0.24	0.26	25.39%	16.24%	24.32%
849.94	0.20	0.06	0.25	0.23	0.25	22.98%	13.62%	23.44%
1150.08	0.19	0.06	0.23	0.21	0.24	20.37%	11.02%	22.24%
1450.11	0.19	0.06	0.22	0.20	0.23	17.63%	8.44%	20.81%

Table 31: Joint 7 surface properties

Scale analysis micro-hardness [Pa]	CMY micro-hardness [Pa]	Effective elasticity [Pa]	Effective thermal conductivity [W/(m·K)]	Effective RMS roughness [m]	Effective average asperity slope [rad]
3.33E+09	3.30E+09	1.29E+11	20.14	2.21E-06	0.17

Table 32: Joint 7 vacuum results

Pressure [kPa]	Exp. TCR [K/W]	Abs. uncertainty [K/W]	TCR scale analysis [K/W]	TCR CMY plastic [K/W]	TCR CMY elastic [K/W]	Rel. dif. scale analysis	Rel. dif. CMY plastic	Rel. dif. CMY elastic
350.15	5.11	0.19	6.89	6.04	13.44	34.95%	18.35%	163.09%
549.48	3.99	0.15	4.39	3.94	8.76	9.97%	1.20%	119.39%
850.11	2.93	0.12	2.84	2.61	5.80	3.02%	10.76%	97.97%
1149.19	1.81	0.08	2.10	1.97	4.36	15.79%	8.34%	140.23%
1450.12	1.67	0.08	1.67	1.58	3.50	0.00%	5.21%	110.11%

Table 33: Joint 7 atmospheric results

Pressure [kPa]	Exp. TCR [K/W]	Abs. uncertainty [K/W]	TCR scale analysis [K/W]	TCR CMY plastic [K/W]	TCR CMY elastic [K/W]	Rel. dif. scale analysis	Rel. dif. CMY plastic	Rel. dif. CMY elastic
276.71	0.44	0.05	0.53	0.48	0.53	19.04%	10.83%	22.20%
549.86	0.41	0.05	0.48	0.44	0.50	16.63%	7.77%	23.32%
849.94	0.39	0.05	0.44	0.40	0.48	14.01%	4.93%	23.92%
1149.75	0.37	0.05	0.41	0.38	0.46	11.20%	2.19%	23.92%
1449.80	0.36	0.05	0.39	0.35	0.44	8.59%	0.21%	23.83%

Appendix C: Tabulated results from Chapter 4

Table 34: Surface properties

Metal Sample	Ceramic Sample	Scale analysis micro-hardness [Pa]	Eff. elasticity [Pa]	Eff. thermal conductivity [W/(m·K)]	Eff. RMS roughness [m]	Effective average asperity slope [rad]
Cast Aluminum	As-fired Al_2O_3	1.02E+09	6.62E+10	41.54	1.60E-06	0.15
Cast Aluminum	Lapped Al_2O_3	1.02E+09	6.62E+10	41.23	1.57E-06	0.15
Cast Aluminum	Polished Al_2O_3	1.02E+09	6.62E+10	41.71	1.22E-06	0.10
Machined Aluminum	As-fired Al_2O_3	1.01E+09	6.62E+10	41.19	1.88E-06	0.16
Machined Aluminum	Lapped Al_2O_3	1.02E+09	6.62E+10	41.78	1.86E-06	0.16
Machined Aluminum	Polished Al_2O_3	1.02E+09	6.62E+10	41.83	1.58E-06	0.11
Anodized Aluminum	As-fired Al_2O_3	1.50E+10	1.95E+11	25.16	1.14E-06	0.14
Anodized Aluminum	Lapped Al_2O_3	1.50E+10	1.95E+11	25.24	1.09E-06	0.13
Anodized Aluminum	Polished Al_2O_3	1.50E+10	1.95E+11	25.17	4.80E-07	0.07

Table 35: Cast aluminum and as-fired Al_2O_3 results

Pressure [kPa]	Exp. TCR [K/W]	Abs. uncertainty [K/W]	TCR scale analysis [K/W]	Rel. dif. scale analysis
264.7797	0.3214	0.0244	0.2825	12.12%
549.9522	0.2759	0.0235	0.2129	22.81%
949.9754	0.2403	0.0227	0.1601	33.39%
1449.8655	0.2129	0.0219	0.1229	42.30%

Table 36: Cast aluminum and lapped Al_2O_3 results

Pressure [kPa]	Exp. TCR [K/W]	Abs. uncertainty [K/W]	TCR scale analysis [K/W]	Rel. dif. scale analysis
214.3098	0.3690	0.0240	0.2958	19.84%
350.0389	0.3469	0.0236	0.2531	27.02%
750.0003	0.2859	0.0225	0.1810	36.70%
1550.0186	0.2314	0.0215	0.1170	49.45%

Table 37: Cast aluminum and polished Al_2O_3 results

Pressure [kPa]	Exp. TCR [K/W]	Abs. uncertainty [K/W]	TCR scale analysis [K/W]	Rel. dif. scale analysis
175.4414	0.3491	0.0246	0.2670	23.52%
349.9981	0.3095	0.0239	0.2270	26.68%
750.0671	0.2520	0.0221	0.1732	31.27%
1550.1455	0.2016	0.0212	0.1201	40.41%

Table 38: Machined aluminum and as-fired Al_2O_3 results

Pressure [kPa]	Exp. TCR [K/W]	Abs. uncertainty [K/W]	TCR scale analysis [K/W]	Rel. dif. scale analysis
250.1142	0.6144	0.0297	0.3309	46.14%
549.8578	0.4976	0.0274	0.2440	50.96%
949.9289	0.4222	0.0260	0.1826	56.75%
1449.7805	0.3602	0.0246	0.1397	61.21%

Table 39: Machined aluminum and lapped Al_2O_3 results

Pressure [kPa]	Exp. TCR [K/W]	Abs. uncertainty [K/W]	TCR scale analysis [K/W]	Rel. dif. scale analysis
249.8779	0.6312	0.0300	0.3291	47.86%
549.8745	0.4845	0.0270	0.2432	49.81%
950.0573	0.3941	0.0248	0.1825	53.68%
1449.8011	0.3244	0.0232	0.1401	56.83%

Table 40: Machined aluminum and polished Al_2O_3 results

Pressure [kPa]	Exp. TCR [K/W]	Abs. uncertainty [K/W]	TCR scale analysis [K/W]	Rel. dif. scale analysis
300.0356	0.4973	0.0269	0.2926	41.17%
550.1000	0.4190	0.0253	0.2401	42.68%
950.0462	0.3456	0.0240	0.1889	45.35%
1450.0315	0.2841	0.0225	0.1502	47.14%

Table 41: Anodized aluminum and as-fired Al_2O_3 results

Pressure [kPa]	Exp. TCR [K/W]	Abs. uncertainty [K/W]	TCR scale analysis [K/W]	Rel. dif. scale analysis
275.0380	0.6030	0.0319	0.3246	46.17%
550.0151	0.5172	0.0296	0.3091	40.24%
949.9346	0.4484	0.0273	0.2929	34.67%
1454.5155	0.4051	0.0262	0.2791	31.11%

Table 42: Anodized aluminum and lapped Al_2O_3 results

Pressure [kPa]	Exp. TCR [K/W]	Abs. uncertainty [K/W]	TCR scale analysis [K/W]	Rel. dif. scale analysis
274.9271	0.4030	0.0254	0.3125	22.47%
549.9575	0.3036	0.0236	0.2978	1.91%
950.0046	0.2598	0.0229	0.2829	8.90%
1449.9929	0.2420	0.0221	0.2692	11.22%

Table 43: Anodized aluminum and polished Al_2O_3 results

Pressure [kPa]	Exp. TCR [K/W]	Abs. uncertainty [K/W]	TCR scale analysis [K/W]	Rel. dif. scale analysis
262.0542	0.3464	0.0245	0.1539	55.56%
549.8754	0.2528	0.0230	0.1477	41.58%
949.9990	0.2019	0.0212	0.1415	29.94%
1450.5399	0.1816	0.0209	0.1365	24.82%

Table 44: Cast aluminum and as-fired Al_2O_3 with thermal grease results

Pressure [kPa]	Exp. TCR [K/W]	Abs. uncertainty [K/W]	TCR scale analysis [K/W]	Rel. dif. scale analysis
249.9780	0.1151	0.0209	0.2056	78.63%
549.8624	0.1040	0.0204	0.2053	97.32%
949.7257	0.0945	0.0200	0.2051	116.97%
1449.9499	0.0877	0.0197	0.2049	133.70%

Table 45: Cast aluminum and as-fired Al_2O_3 with gap filler results

Pressure [kPa]	Exp. TCR [K/W]	Abs. uncertainty [K/W]	TCR scale analysis [K/W]	Rel. dif. scale analysis
299.8187	0.0693	0.0197	0.1110	60.17%
550.0182	0.0678	0.0195	0.1109	63.44%
849.8453	0.0662	0.0194	0.1108	67.20%
1450.2564	0.0643	0.0192	0.1106	72.08%

Table 46: Machined aluminum and as-fired Al_2O_3 with thermal grease results

Pressure [kPa]	Exp. TCR [K/W]	Abs. uncertainty [K/W]	TCR scale analysis [K/W]	Rel. dif. scale analysis
266.6458	0.0951	0.0220	0.2064	116.99%
549.8662	0.0854	0.0213	0.2061	141.20%
950.0432	0.0761	0.0207	0.2058	170.32%
1449.5706	0.0690	0.0202	0.2056	197.96%

Table 47: Machined aluminum and as-fired Al_2O_3 with gap filler results

Pressure [kPa]	Exp. TCR [K/W]	Abs. uncertainty [K/W]	TCR scale analysis [K/W]	Rel. dif. scale analysis
249.9488	0.0641	0.0218	0.1116	74.06%
549.8906	0.0661	0.0213	0.1114	68.38%
949.8297	0.0647	0.0206	0.1112	72.00%
1450.0034	0.0629	0.0199	0.1111	76.52%

Table 48: Anodized aluminum and as-fired Al_2O_3 with thermal grease results

Pressure [kPa]	Exp. TCR [K/W]	Abs. uncertainty [K/W]	TCR scale analysis [K/W]	Rel. dif. scale analysis
249.9233	0.1473	0.0218	0.2048	39.08%
550.0881	0.1364	0.0213	0.2047	50.01%
950.0388	0.1282	0.0208	0.2045	59.55%
1449.8957	0.1223	0.0204	0.2044	67.13%

Table 49: Anodized aluminum and as-fired Al_2O_3 with gap filler results

Pressure [kPa]	Exp. TCR [K/W]	Abs. uncertainty [K/W]	TCR scale analysis [K/W]	Rel. dif. scale analysis
290.0215	0.0900	0.0204	0.1106	22.84%
549.9353	0.0875	0.0202	0.1105	26.20%
950.1355	0.0856	0.0200	0.1104	28.92%
1449.9032	0.0844	0.0196	0.1103	30.70%